Repository Istituzionale dei Prodotti della Ricerca del Politecnico di Bari

High Q-factor photonic cavities as new transducers for photothermal spectroscopy

This is a PhD Thesis

Original Citation:
High Q-factor photonic cavities as new transducers for photothermal spectroscopy / Mendoza Castro, Jesus Hernan. - ELETTRONICO. - (2023). [10.60576/poliba/iris/mendoza-castro-jesus-hernan_phd2023]

Availability:
This version is available at http://hdl.handle.net/11589/264723 since: 2024-01-15

Published version
DOI:10.60576/poliba/iris/mendoza-castro-jesus-hernan_phd2023
Politecnico di Bari

Terms of use:
Altro tipo di accesso

(Article begins on next page)

02 May 2024

EUROPEAN JOINT DOCTORATE PROGRAMME
"OPTICAL SENSING USING ADVANCED PHOTO-INDUCED EFFECTS – OPTAPHI"
MARIE SKŁODOWSKA-CURIE GRANT AGREEMENT NO. 860808

Politecnico di Bari

Department of Electrical and Information Engineering

ELECTRICAL AND INFORMATION ENGINEERING
SSD: ING-INF/02–ELECTROMAGNETIC FIELDS

TU WIEN TECHNISCHE UNIVERSITÄT WIEN

Faculty of Technical Chemistry
Institute of Chemical Technologies and Analytics

DOCTOR OF TECHNICAL SCIENCE (DR. TECHN.)

Ph.D. Program

Final Dissertation

High Q-factor Photonic Cavities as new transducers for Photothermal Spectroscopy

defended by
Jesús Hernán Mendoza Castro

Supervisors:

Prof. Marco Grande

Univ. Prof. Dr. Bernhard Lendl

Coordinator of Ph.D. Program:
Prof. Carpentieri Mario

Course n°36, 01/11/2020-31/10/2023

Politecnico di Bari

LIBERATORIA PER L'ARCHIVIAZIONE DELLA TESI DI DOTTORATO

Al Magnifico Rettore
del Politecnico di Bari

Il sottoscritto *Jesus Hernan Mendoza Castro* nato a *Lebrija-Santander, Colombia il 17/11/1991* residente a *Gasgasse | OeAD student housing, Gasgasse 2, 5050/4, Vienna, Austria*, e-mail: *nachomendozac@gmail.com* iscritto al 3° anno di Corso di Dottorato di Ricerca in Ingegneria Elettrica e dell'Informazione ciclo *XXXVI* ed essendo stato ammesso a sostenere l'esame finale con la prevista discussione della tesi dal titolo: "*High Q-factor Photonic Cavities as new transducers for Photothermal Spectroscopy"*

DICHIARA

1) di essere consapevole che, ai sensi del D.P.R. n. 445 del 28.12.2000, le dichiarazioni mendaci, la falsità negli atti e l'uso di atti falsi sono puniti ai sensi del codice penale e delle Leggi speciali in materia, e che nel caso ricorressero dette ipotesi, decade fin dall'inizio e senza necessità di nessuna formalità dai benefici conseguenti al provvedimento emanato sulla base di tali dichiarazioni;
2) di essere iscritto al Corso di Dottorato di ricerca Ingegneria Elettrica e dell'Informazione ciclo XXXVI, corso attivato ai sensi del "*Regolamento dei Corsi di Dottorato di ricerca del Politecnico di Bari"*, emanato con D.R. n.286 del 01.07.2013;
3) di essere pienamente a conoscenza delle disposizioni contenute nel predetto Regolamento in merito alla procedura di deposito, pubblicazione e autoarchiviazione della tesi di dottorato nell'Archivio Istituzionale ad accesso aperto alla letteratura scientifica;
4) di essere consapevole che attraverso l'autoarchiviazione delle tesi nell'Archivio Istituzionale ad accesso aperto alla letteratura scientifica del Politecnico di Bari (IRIS-POLIBA), l'Ateneo archivierà e renderà consultabile in rete (nel rispetto della Policy di Ateneo di cui al D.R. 642 del 13.11.2015) il testo completo della tesi di dottorato, fatta salva la possibilità di sottoscrizione di apposite licenze per le relative condizioni di utilizzo (di cui al sito http://www.creativecommons.it/Licenze), e fatte salve, altresì, le eventuali esigenze di "embargo", legate a strette considerazioni sulla tutelabilità e sfruttamento industriale/commerciale dei contenuti della tesi, da rappresentarsi mediante compilazione e sottoscrizione del modulo in calce (Richiesta di embargo);
5) che la tesi da depositare in IRIS-POLIBA, in formato digitale (PDF/A) sarà del tutto identica a quelle **consegnate**/inviate/da inviarsi ai componenti della commissione per l'esame finale e a qualsiasi altra copia depositata presso gli Uffici del Politecnico di Bari in forma cartacea o digitale, ovvero a quella da discutere in sede di esame finale, a quella da depositare, a cura dell'Ateneo, presso le Biblioteche Nazionali Centrali di Roma e Firenze e presso tutti gli Uffici competenti per legge al momento del deposito stesso, e che di conseguenza va esclusa qualsiasi responsabilità del Politecnico di Bari per quanto riguarda eventuali errori, imprecisioni o omissioni nei contenuti della tesi;
6) che il contenuto e l'organizzazione della tesi è opera originale realizzata dal sottoscritto e non compromette in alcun modo i diritti di terzi, ivi compresi quelli relativi alla sicurezza dei dati personali; che pertanto il Politecnico di Bari ed i suoi funzionari sono in ogni caso esenti da responsabilità di qualsivoglia natura: civile, amministrativa e penale e saranno dal sottoscritto tenuti indenni da qualsiasi richiesta o rivendicazione da parte di terzi;
7) che il contenuto della tesi non infrange in alcun modo il diritto d'Autore né gli obblighi connessi alla salvaguardia di diritti morali od economici di altri autori o di altri aventi diritto, sia per testi, immagini, foto, tabelle, o altre parti di cui la tesi è composta.

Luogo e data ***Vienna, Austria, 15/12/2023*** Firma Jesús Hernán Mendoza Castro

Il/La sottoscritto, con l'autoarchiviazione della propria tesi di dottorato nell'Archivio Istituzionale ad accesso aperto del Politecnico di Bari (POLIBA-IRIS), pur mantenendo su di essa tutti i diritti d'autore, morali ed economici, ai sensi della normativa vigente (Legge 633/1941 e ss.mm.ii.),

CONCEDE

- al Politecnico di Bari il permesso di trasferire l'opera su qualsiasi supporto e di convertirla in qualsiasi formato al fine di una corretta conservazione nel tempo. Il Politecnico di Bari garantisce che non verrà effettuata alcuna modifica al contenuto e alla struttura dell'opera.
- al Politecnico di Bari la possibilità di riprodurre l'opera in più di una copia per fini di sicurezza, back-up e conservazione.

Luogo e data ***Vienna, Austria, 15/12/2023*** Firma Jesús Hernán Mendoza Castro

"Wanderer, your footsteps
are the road and nothing more;
wanderer, there is no road,
the road is made by walking.
By walking one makes the road,
and upon glancing behind
one sees the path.
that never will be trod again."
– Antonio Machado

ACKNOWLEDGMENTS

I am deeply thankful to everyone who shared this path with me. Every unique experience we had undoubtedly contributed to this step.

I would like to express my gratitude to my supervisors, Dr. Marco Grande, and Dr. Bernhard Lendl, for providing me with the opportunity to be part of this remarkable journey in OPTAHI. Experiencing diverse research environments and methodologies at Politecnico di Bari in Italy and TU Wien in Vienna has greatly contributed to my personal and professional growth.

Bernhard, I want to extend my sincere thanks for allowing me to be part of your team. Your support and critical thinking consistently guided us in the right direction, ensuring the significance of each step we took. Analytical chemistry is an endless realm of possibilities, and this interdisciplinary project has confirmed it. I am truly grateful for the time you spent asking the right questions, not only in research.

Marco, I appreciate the challenges you presented to me, for delving into some computational aspects of photonics and how they translate into real devices. My deepest feelings of gratitude are directed towards you. Everything you did to pave the way for me, and your PhD students is something we can never truly repay. Your exemplary leadership, patience, commitment, and optimism served as invaluable lessons. “Do not lose momentum” will forever be etched in my mind, motivating me not to give up.

Prof. ssa Antonella D’orazio I appreciate all your support and brave attitude in the last hard weeks. Thanks, Dr. William Whelan-Curtin for supporting us during this process.

Thanks to Silvia from the Cell chip group at TU Wien. Your support makes possible the next steps in this project.

I acknowledge the European Joint Doctorate Programme "Optical Sensing Using Advanced Photo-Induced Effects – OPTAPHI" and the Marie Skłodowska-Curie Grant, which make it possible to obtain the results presented in this study.

All the people I had the opportunity to meet during these 2 and a half years in Europe, a big thank you. I want to express my gratitude to the people at TU Wien, Politecnico di Bari, OPTAPHI, and everyone who made this journey unforgettable. Artem, Simone, Michelle, Ajmal, Giulia, Savda, Davide, Gabrielle, Ilaria... an endless list of people who offered me a beer to relax, a laugh to keep going, their time to solve problems, a listening ear, skills, expertise, and precious moments of mutual support. This genuinely makes me happy because we were wanderers but never alone. Thank you to everybody.

A mis padres, gracias por ser la razón más importante para seguirlo intentando todos los días, así como ustedes tantas veces lo han hecho. Su ejemplo de dignidad y trabajo duro marcó en mi la motivación para apostarle a este reto. Cada pequeño paso que he podido dar hasta ahora, no ha sido más que el resultado de su confianza. Esto también es de ustedes. Amándolos siempre.

A la reina de mi vida, que siempre ha sabido ser un apoyo a pesar de las circunstancias. Me siento muy afortunado de que hayamos podido crecer juntos y a la par de nuestros sueños seguir abriendo caminos.

A todos los míos en Colombia y Ecuador, aunque no los nombre uno por uno quiero que sepan que, a su modo pusieron granos de arena que contribuyeron a que me encuentre hoy aquí. Los abrazo siempre desde el corazón.

Me siento orgulloso de mis raíces, de ese pedacito de tierra intrincado en las montañas que me vio crecer. Nunca imaginé que me movería tan lejos, pero más aún que la vida nunca dejaría de ser generosa.

08/11/2023
Jesús Hernán Mendoza Castro

LIST OF PUBLICATIONS

Journal papers

- Iadanza, S., **Mendoza-Castro, J. H.**, Oliveira, T., Butler, S., Tedesco, A., Giannino, G., Lendl, B., Grande, M. & O'Faolain, L, "High-Q asymmetrically cladded silicon nitride 1D photonic crystals cavities and hybrid external cavity lasers for sensing in air and liquids," Nanophotonics, vol. 11, no. 18, pp. 4183–4196, Aug. 2022, doi: https://doi.org/10.1515/nanoph-2022-0245 [1]

- **Mendoza-Castro, J.H.*,** Vorobev A.S.*, Iadanza S., Lendl B., O'Faolain L., Grande M., "Enhanced Fano resonances in a Silicon Nitride Photonic Crystal Nanobeam-assisted Micro Ring Resonator for dual telecom band operation", ID: 504912. Opt. Express. (2023), doi DOI: https://doi.org/10.1364/OE.504912.***(*Joint authorship)***

- **Mendoza-Castro, J.H.*,** Vorobev A.S.*, Iadanza S., Lendl B., O'Faolain L., Grande M., "Fano resonances in a Silicon Nitride Photonic Crystal Nanobeam evanescently coupled to a high-Q Micro Ring Resonator". *MANUSCRIPT IN PREPARATION* ID: xxxxxx. Opt. Express. (2023). ***(*Joint authorship)***

Conference Proceedings

- T. Oliveira, S. Iadanza, **J. H. Mendoza-Castro**, M. Grande and L. O'Faolain, "Silicon Nitride 1D Photonic Crystal Cavity Hybrid Laser for Refractive Index Sensing in Liquid and Gaseous Media," 2023 Conference on Lasers and Electro-Optics Europe & European Quantum Electronics Conference (CLEO/Europe-EQEC), Munich, Germany, 2023, pp. 1-1, doi: https://doi.org/10.1109/CLEO/Europe-EQEC57999.2023.10231533 [2]

- **J.H. Mendoza-Castro**, A.S. Vorobev, S. Iadanza, B. Lendl, M. Grande, L. O'Faolain, Fano Resonances in a Photonic Crystal Side-Coupled Micro Ring Resonator for Refractive Index Sensing, in 2023 Conference on Lasers and Electro-Optics Europe & European Quantum Electronics Conference (CLEO/Europe-EQEC), IEEE, Munich, Germany, 2023: pp. 1–1. https://doi.org/10.1109/CLEO/Europe-EQEC57999.2023.10231647 [3]

- **J.H. Mendoza-Castro**, A.S. Vorobev, S. Iadanza, B. Lendl, M. Grande, L. O'Faolain, Q-Factor Optimization in Photonic Crystal Nanobeam Cavities Based on Elliptical Nanopillars for Refractive Index Sensing, in 2023 Conference on Lasers and Electro-Optics Europe & European Quantum Electronics Conference (CLEO/Europe-EQEC), IEEE, Munich, Germany, 2023: pp. 1–1. https://doi.org/10.1109/CLEO/Europe-EQEC57999.2023.10232053 [4]

- A.S. Vorobev, **J.H. Mendoza-Castro**, S. Iadanza, B. Lendl, M. Grande, L. O'Faolain, Enable Fano resonances lineshapes in a Silicon Nitride Photonic Crystal-MicroRing structure, in 2023

IEEE Silicon Photonics Conference (SiPhotonics), IEEE, Washington, DC, USA, 2023: pp. 1–2. https://doi.org/10.1109/SiPhotonics55903.2023.10141919 [5]

- **J.H. Mendoza-Castro**, A.S. Vorobev, S. Iadanza, T. Oliveira, B. Lendl, L. O'Faolain, M. Grande, Compact side-coupled Silicon Nitride Photonic Crystal Nanobeam Cavity for refractive index sensing, in 2023 IEEE Silicon Photonics Conference (SiPhotonics), IEEE, Washington, DC, USA, 2023: pp. 1–2. https://doi.org/10.1109/SiPhotonics55903.2023.10141917 [6]

- **J. H. Mendoza-Castro**, L. O'Faolain, and M. Grande, "Q-factor enhancement in photonic crystal cavities based on trapezoidal slotted nano-sticks for refractive index sensing," 2021 Conference on Lasers and Electro-Optics Europe & European Quantum Electronics Conference (CLEO/Europe-EQEC), 2021, pp. 1-1, doi: https://doi.org/10.1109/CLEO/Europe-EQEC52157.2021.9542649 [7]

Conferences – Oral Presentations

- **J.H. Mendoza-Castro**, A.S. Vorobev, S. Iadanza, B. Lendl, L. O'Faolain and M. Grande. "Control of Fano Spectral Profile based on a Silicon Nitride Photonic Crystal-Micro Ring Resonator structure"; C-PASS 2023, Castellaneta Marina, Italy; September 2023.

- A.S. Vorobev, **J. H. Mendoza-Castro** et all. "Graphene Electrodes on Silicon Nitride Devices for Near-Infrared Wavelength Tuning"; C-PASS 2023, Castellaneta Marina, Italy; September 2023.

- G. Ricchiuti, **J. H. Mendoza-Castro**, Walsh A., Vorobev A.S. et all. "Photothermal Spectroscopy (PTS) of PMMA thin layer using micro-ring resonators (MRRs)"; C-PASS 2023, Castellaneta Marina, Italy; September 2023.

- T. Oliveira, S. Iadanza, **J. H. Mendoza-Castro**, M. Grande and L. O'Faolain, "Silicon Nitride 1D Photonic Crystal Cavity Hybrid Laser for Refractive Index Sensing in Liquid and Gaseous Media"; 2023 Conference on Lasers and Electro-Optics Europe & European Quantum Electronics Conference (CLEO/Europe-EQEC), Munich, Germany; June 2023.

- A. S. Vorobev, **J. H. Mendoza-Castro**, S. Iadanza, B. Lendl, M. Grande and L. O'Faolain, "Enable Fano resonances lineshapes in a Silicon Nitride Photonic Crystal-MicroRing structure"; 2023 IEEE Silicon Photonics Conference (SiPhotonics), Washington, DC, USA; April 2023.

- **J.H. Mendoza-Castro**, A.S. Vorobev, S. Iadanza, M. Grande, L. O'Faolain and B. Lendl "Engineering resonances in Photonic integrated circuits for Lab-On-a-Chip spectroscopy"; The 3rd Student meeting of the Coblentz Society and NE & NY Society for Applied Spectroscopy (SAS) Section. Three minutes presentations by Ph.D. students from across the world working in all fields of vibrational spectroscopy; March 2023.

- **J.H. Mendoza-Castro**, "Project 2.3: High Q-factor photonic cavities for PTS"; 3rd OPTAPHI Workshop: Applications of Advanced Spectroscopy and Integrated Photonics – Cork, Ireland; December 2022.

- **J. H. Mendoza-Castro**, S. Iadanza, T. Oliveira, S. M. Butler, A. Tedesco, G. Giannino, B. Lendl, M. Grande, and L. O'Faolain, " Refractive index sensor based on Silicon Nitride photonic crystal operating on Hybrid External Cavity Laser configuration"; META 2022, Torre Molinos, Spain; July 2022. https://metaconferences.org/META/files/meta22_proceedings.pdf

- **J.H. Mendoza-Castro**, “Project 2.3: High Q-factor photonic cavities for PTS”; 2nd OPTAPHI Workshop: Advanced spectroscopy & Cooperation – Vienna, Austria; April 2022.

Conferences – Poster Presentations

- **J.H. Mendoza-Castro**, A.S. Vorobev, S. Iadanza, B. Lendl, L. O’Faolain and M. Grande. “Integrated waveguide coupled Si_3N_4 Photonic Crystal Nanobeam Cavity for refractive index sensing”; C-PASS 2023, Castellaneta Marina, Italy; September 2023;

- **J.H. Mendoza-Castro**, A.S. Vorobev, S. Iadanza, B. Lendl, L. O’Faolain and M. Grande. “Silicon Nitride photonic cavities for refractive index sensing: from Photonic crystals to Fano resonances”; D-PHOTON 2023, Bari, Italy. July 2023;

- A.S. Vorobev, J. H. **Mendoza-Castro**, S. Iadanza, G.V. Bianco, G. Bruno, A. D’Orazio, L. O’Faolain and M. Grande. “Graphene Electrodes on Silicon Nitride Devices for Near-Infrared Wavelength Tuning”; D-PHOTON 2023, Bari, Italy. July 2023;

- **J. H. Mendoza-Castro**, A. S. Vorobev, S. Iadanza, B. Lendl, M. Grande and L. O'Faolain, "Q-Factor Optimization in Photonic Crystal Nanobeam Cavities Based on Elliptical Nanopillars for Refractive Index Sensing"; 2023 Conference on Lasers and Electro-Optics Europe & European Quantum Electronics Conference (CLEO/Europe-EQEC), Munich, Germany; June 2023.

- **J. H. Mendoza-Castro**, A. S. Vorobev, S. Iadanza, B. Lendl, M. Grande and L. O'Faolain, "Fano Resonances in a Photonic Crystal Side-Coupled Micro Ring Resonator for Refractive Index Sensing"; 2023 Conference on Lasers and Electro-Optics Europe & European Quantum Electronics Conference (CLEO/Europe-EQEC), Munich, Germany; June 2023.

- **J.H. Mendoza-Castro**, A.S. Vorobev, S. Iadanza, B. Lendl, L. O’Faolain and M. Grande. “High-Q factor Si_3N_4 Fano cavity for On-Chip refractive index sensing”; ANAKON 2023, Vienna, Austria; July 2023.

- **J. H. Mendoza-Castro**, A.S. Vorobev, S. Iadanza, T. Oliveira, B. Lendl, L. O’Faolain, M. Grande., "Compact side-coupled Silicon Nitride Photonic Crystal Nanobeam Cavity for refractive index sensing"; 2023 IEEE Silicon Photonics Conference (SiPhotonics), Washington, DC, USA; April 2023.

- **J. H. Mendoza-Castro**, L. O’Faolain, and M. Grande, "Q-factor enhancement in photonic crystal cavities based on trapezoidal slotted nano-sticks for refractive index sensing"; 2021 Conference on Lasers and Electro-Optics Europe & European Quantum Electronics Conference (CLEO/Europe-EQEC), Virtual meeting; June 2021.

CONTENTS

Acknowledgments **6**
List of Publications **8**
Journal papers 8
Conference Proceedings 8
Conferences – Oral Presentations 9
Conferences – Poster Presentations 10
Contents **11**
Abstract **14**
Introduction **16**
Chapter 1 - High Q-factor photonic cavities for Photothermal spectroscopy **21**
1.1. High Q-factor photonic cavities 22
1.2. Aim of the Thesis 24
1.3. Thesis Content 25
Chapter 2 - Fundamentals **26**
2.1. Photonic Crystals Nanobeam Cavities 26
2.1.1. Photonic Crystals 26
2.1.2. Refractive index sensing characteristics 29
2.2. Micro Ring Resonators 30
2.2.1. Micro ring resonator 30
2.2.2. Refractive index sensing characteristics 31
2.3. Summary & Perspective 34
Chapter 3 - Photonic Crystal Nanobeam Cavities **36**
3.1. Engineered angled sidewalls 36
3.1.1. Design and Simulation 37
3.1.2. Fabrication and Experimental Results 42
3.1.2.2. Passive measurements 43
3.1.2.3. Active measurements 45

3.2. Elliptical Nano pillars 45
3.3. Slotted Nanobeam 48
3.4. Summary & Perspective 50
Chapter 4 - Photonic Fano Cavities based Micro Ring Resonators 52
4.1. Fano resonance generation in a Photonic Crystal Nanobeam-assisted MRR 52
4.1.1. Principle 52
4.1.2. Design and Simulations 56
4.1.2.1. Silicon Nitride Micro Ring Resonator 56
4.1.2.2. Air-based circular holes Photonic Crystal Nanobeam-assisted Micro Ring Resonator 57
4.1.2.3. Air-based rectangular slots Photonic Crystal Nanobeam-assisted Micro Ring Resonator 60
4.1.3. Fabrications and experimental results 62
4.1.3.2. TE-like mode at C-band 63
4.1.3.3. TM-like mode at O-band 66
4.1.3.4. Water cladding 67
4.2. Summary & Perspective 69
Chapter 5 - Microfluidics Integration 70
5.1. Material platforms 70
5.2. Bonding Strategies 72
5.3. Integration with Si_3N_4 Photonic Cavities 73
5.4. Refractive index Sensing 74
5.5. Summary & Perspective 76
Chapter 6 - Conclusions & Outlook 77
6.1. Outlook 77
6.1.1. MIR Metasurfaces (collaboration with Artem Vorobev and Giulia Malvicini) 77
6.1.1.2. Guided Mode Resonances 78
6.1.1.3. Fabrication 80
6.1.2. Integration in a photothermal system (Collaboration with Giovanna Richiutti) 80
6.1.3. Flow injection analysis and Fiber coupling 81
6.2. Conclusions 81
Appendix A– Computational photonics 84
Appendix B – 1D Photonic Band Gap in 1D Photonic Crystal 88
References 91

ABSTRACT

Spectroscopic sensors represent a significant type of device designed to study the distinct fingerprint absorption spectrum of molecules. Photothermal spectroscopy (PTS) stands out as a highly sensitive and selective method, enabling the indirect measurement of the optical absorption of specific materials. In PTS, accurate measurement of refractive index changes is crucial. Therefore, suitable transducers for measuring such changes in gaseous and liquid samples are required. While excellent results have been achieved, the system remains bulky. The refractive index sensitivity and real-time measurement capabilities of integrated photonics make them ideal for interfacing with PTS systems.

Integrated photonics enable the implementation of compact devices that facilitate efficient light-matter interaction. Among these devices, high-quality factor resonators can significantly enhance their performance by allowing light to circulate within the device for extended periods. Furthermore, they can be engineered to cover a wide range of refractive indices, making them versatile for various gaseous and liquid samples. Additionally, combining photonics with on-chip components such as microfluidics opens the possibilities for fully integrated lab-on-a-chip systems, providing comprehensive solutions for sample handling and analysis.

In this thesis, various types of integrated photonic resonators have been designed and numerically studied for using as new refractive index transducers in PTS. The computational work conducted for this research required access to high-performance computing infrastructure provided by CINECA in Italy and Politecnico di Bari, Italy. Commercial solver RSOFT, and flexible open-source tools like MEEP and MPB, were employed. A combination of 2D and 3D-Finite Difference Time Domain simulations, as well as Rigorous Coupled Wave Analysis (RCWA) and other solvers, were used to simulate the proposed resonant structures.

The combination of a reduced thermo-optic coefficient and low two-photon absorption has established Silicon Nitride as the primary platform for the devices proposed in this thesis. Photonic cavities with high Q-factors and small modal volumes offer increased sensitivity and lower detection limits. Consequently, this study prioritized the design of photonic crystal nanobeam cavities (PhCNC) and Micro Ring Resonators (MRR). MRRs are characterized by their Free Spectral Range (FSR), while PhCNCs can be optimized to support single-mode operation, which is particularly relevant for demonstrating a Hybrid External Cavity Laser (HECL).

Fano resonances are a specific interference phenomenon observed in the scattering of waves. They are characterized by a spectral shape with an asymmetric line profile. The steep profile of Fano resonances can lead to more significant signal changes when a transducer interacts with samples. To achieve Fano resonance lineshapes, a photonic crystal nanobeam was side-coupled to a MRR.

Three variations of PhCNCs were investigated. The design with angled sidewalls demonstrated high tunability of the Q-factor, favoring more asymmetric cladding configurations. In the case of elliptical nanopillar design, there was a reduction in the impact of fabrication errors on the Q-factor. The Silicon-based slotted configuration exhibited a significant enhancement in the Q-factor through sidewall engineering. Furthermore, by side-coupling a S-bent waveguide to the PhCNCs, nearly single-mode operation was achieved. Conversely, the designs of circular-hole and rectangular-slot Fano resonators exhibited Fano lineshapes consistently. Furthermore, the ability to tune these asymmetric shapes was successfully demonstrated. Additionally, metasurfaces for Silicon on Si_3N_4 membranes operating in Mid-IR wavelength range are explored. Near-field enhancement and Fano-like features were examined.

Based on the simulations conducted, the optimal and most rugged geometries that can be fabricated in a single etching process were found. The fabrication was carried out by our consortium partners at Tyndall National Institute and the Centre of Advanced Photonics & Process Analytics (CAPPA), Ireland. The fabrication was led by Simone Iadanza and Artem Vorobev. Initial characterization of the fabricated devices and some of the experiments were conducted in collaboration with the CAPPA lab, including the demonstration of the HECL-based PhCNC sensor. The fabrication of metasurfaces is an ongoing process.

At TU Wien, Vienna an experimental setup for the characterization of the fabricated Photonic integrated circuits was built from scratch. The experimental measurements exhibited agreement with the trends observed in simulations. Nevertheless, certain discrepancies are noted and discussed. To enhance stability and enable the measurement of small refractive index changes, thermal stabilization control into the setup was incorporated.

Furthermore, advancements in the integration of liquid handling through microfluidics are demonstrated. The collaboration with the Dipl.-Ing. Silvia Schobesberger, a member of the Cell Chip group at TU Wien, allows the realization of a reliable microfluidic cell. The implemented microfluidic cell on the refractive index transducer Si_3N_4 surface was tested with aqueous glucose solutions showing an almost linear response. Thus, this transducer can now be used as a refractive index detector in liquid chromatography and in flow injection analysis.

On the other hand, ongoing efforts on Photo Thermal Spectroscopy concerns about the refractive index transducers presented here. Therefore, further improvements toward an integrated PTS sensor could build upon the results discussed in this thesis.

INTRODUCTION

Spectroscopy is a powerful tool that deals with the study of interactions between matter and electromagnetic radiation, including visible light, infrared, and ultraviolet radiation. It enables the exploration of the composition, structure, and properties of various substances by analyzing the way they interact with light. Spectroscopy plays a crucial role in fields such as chemistry, physics, astronomy, and environmental science, offering insights into the fundamental nature of matter and the universe itself. The interactions in spectroscopy methods between radiation and matter may include various processes, such as absorption, emission, or scattering. Spectroscopy finds widespread application in the analysis of diverse materials across solid, liquid, gas, and plasma states. Its utility in gas-sensing is extensive, serving critical roles in the chemical industry, material sciences, pharmaceuticals, and oil refineries. Spectroscopy plays a vital role in assessing air quality, encompassing indoor air quality control, outdoor pollution monitoring, and the investigation of greenhouse gas emissions and their distribution[8].

In a wide range of applications, the precise and quantitative measurement of trace gases stands as a crucial requirement. This need extends across medical diagnostics, process control, environmental monitoring, and scientific research. While powerful gas laser sensors have been developed, there remains a persistent demand for more sensitive and reliable miniature sensors. Achieving miniaturization in sensors plays a crucial role in scenarios where a compact absorption volume is essential. However, this remains a challenge. Reducing the probe volume offers significant advantages, particularly in the monitoring of rapidly changing gas concentrations within gas streams, allowing for swift gas exchange and ensuring a prompt sensor response. Such miniature sensors are invaluable when working with limited quantities of the target gas [9].

In the realm of sensor miniaturization, promising solutions emerge through the utilization of indirect absorption spectroscopy techniques, specifically photothermal spectroscopy (PTS) and photoacoustic spectroscopy (PAS). These innovative approaches eliminate the need for extensive path lengths, opting for alternative methodologies. Both methods involve the indirect generation of signals through the application of excitation lasers. As electromagnetic waves are absorbed by molecules, their internal energy levels increase, resulting in sample heating via energy transfer through collisional relaxation. Consequently, fluctuations in sample temperature induce changes in density and pressure, giving rise to PTS and PAS signals [10].

PTS is a technique that quantifies a signal directly proportional to the induced temperature change, primarily caused by the presence of a sample being measured. What sets this method apart is its "baseline-free" characteristic, as a signal is only generated in the presence of the sample. When the sample absorbs energy from incident light, the amount of absorbed energy correlates with the light's intensity. When the light intensity is modulated, it results in localized transient heating within the sample. This heating initiates the creation of two distinct

waves. The first is a weakly damped propagating acoustic (pressure) wave with wavelengths in the centimeter range. The second is a heavily damped thermal wave observable only near the incident light beam. These waves possess different damping coefficients and wavelengths, causing them to separate spatially and enabling independent study [11].

The fundamental principle of PTS is depicted in Figure 1. Here, a laser source (pump beam) is employed to excite the sample under examination, with specific intensity modulation at a defined frequency. This modulation leads to periodic heating and cooling of the sample, subsequently inducing changes in its refractive index. A second laser source, known as the "probe beam," is utilized to detect and measure the thermally photo-induced relative refractive index gradient, denoted as Δn.

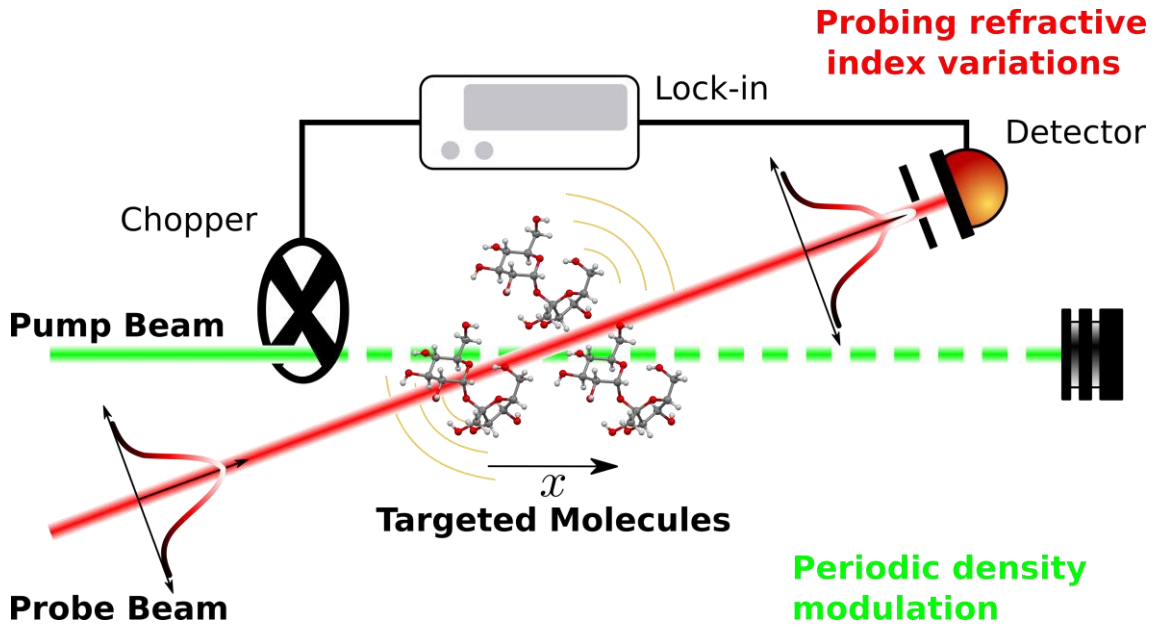

Figure 1 – Schematic structure of Photothermal common-path interferometry system.

PTS offers versatility in its implementation through various experimental setups, allowing for customization to suit different research requirements. These setups encompass distinct beam geometries (single-beam or collinear/transversal dual-beam), diverse excitation laser modes (continuous wave or pulsed), and a range of transduction methods (e.g., photothermal deflection, photothermal lens, or photo-thermal interferometry).

Among the available configurations, the dual-beam arrangement, although more demanding in terms of alignment, stands out for its superior sensitivity when compared to the single-beam setup. In the dual-beam setup, the photothermal effect generation and detection are executed using two laser sources operating in different spectral regions. Typically, the probe laser is chosen for its cost-effectiveness and non-invasive nature, facilitating the monitoring of the sample's thermal response.

Alignment of the two laser beams can be achieved either collinearly, where they overlap, or perpendicularly. Collinear alignment offers improved absolute sensitivity due to the extended interaction length between the beams. In contrast, the transversal mode does not rely on the sample's length but still offers the potential for achieving excellent detection limits. The choice of the detection scheme is primarily based on the specific application of interest.

The bulky setups required for PTS need to integrate components that can further reduce its dimension. Photonic cavities as refractive index transducers can do one of the first steps to

further miniaturize a spectroscopy system. In the domain of photonics, optical signals propagate through waveguides employing a Total Internal Reflection (TIR) regime. This mode of operation results in the generation of an evanescent electromagnetic field characterized by penetration depths ranging from 100 to 900 nanometers The enhanced light-matter interaction produced in the reduced volume surrounding the photonic sensors, makes them a good choice for refractive index sensing. Evanescent wave optical sensors are an integral component of advanced photonics research due to the versatile use they have in a label-free configuration. This means that they eliminate the need for fluorescent, colorimetric, or enzymatic tags, reducing the complexity of assays and streamlining the detection process. Their remarkable sensitivity obviates the necessity for additional amplification steps, thereby expediting and simplifying the analytical procedures [12].

Photonic sensors find extensive application in industries such as chemistry, biomedicine, and food processing, where they serve as valuable tools for measuring refractive indices. These sensors are particularly favored for their capability to deliver remarkable sensitivity to changes in ambient refractive indices, owing to the distinctive field distribution of their resonances [13–15]. The sensitivity of an optical sensor is intricately linked to the sensor's material and structural properties. Therefore, strategies to manipulate the field distribution rely on a rigorous structural design that allows highly localized electromagnetic fields. Therefore, the diversity of photonics can provide the tools to realize an integrated PTS sensor.

European Double Doctorate Training Network on Optical Sensing Using Advanced Photo-Induced Effects (OPTAPHI) focuses on the development of compact and robust Photo-acoustic and Photothermal sensors. The consortium aims to pioneer novel laser technologies, including hybrid photonic crystal lasers and Quantum Cascade Lasers with extended wavelengths to bridge gaps in this scientific research discipline. Additionally, OPTAPHI explores innovative spectroscopic configurations enabled by these in-house state-of-the-art laser systems.

The OPTAPHI project required close collaboration between academic institutions and partner organizations, with each contributing expertise in spectroscopy and photonic integration. Previous experience of the members and recent breakthroughs enable participant researchers to focus on specific identified challenges and subsequently align their findings to create a comprehensive solution.

One of OPTAPHI's primary objectives is to create portable solutions for real-time gas detection, making significant contributions to environmental monitoring, industrial process control, hydrocarbon gas sensing, and the monitoring of toxic gases and food quality. The target sensor should be able to produce measurements comparable to those obtained through traditional laboratory-based techniques like mass spectroscopy or chromatography, despite being significantly smaller in size. Its cost-effective and autonomous design will allow it ideally for embedded and extensive pollution monitoring in urban environments. Leveraging the availability of affordable electronic systems, this device will be well-equipped for its purpose. Furthermore, thanks to its wavelength-independent characteristic, it can incorporate lasers spanning the entire electromagnetic spectrum, from UV to THz.

Another challenge OPTAPHI aims to address is the advancement of innovative sensing methods and laser sources for highly sensitive gas and liquid detection in industrial processes. For instance, the program seeks to enhance the capabilities of techniques like PTS for the detection of water in organic solvents. Therefore, innovative, and optimized laser sources through the development of novel hybrid lasers and single-mode interband cascade lasers,

are expected. The gases that can be detected using PTS depend on the laser's wavelength, which needs to be customized to match the absorption lines of the target gas. To create compact, portable, and cost-effective sensors, these lasers must have a small size (e.g., DFB laser), and be integrated with the PTS cell.

With this in mind, several interrelations arise among the projects within the OPTAPHI consortium. At first, project 1.3 “Photonic crystal hybrid lasers for intra-cavity QEPAS and PTS” led by Gautham Paikkath will provide and hybrid probe laser [16]. For reference, the sketched probe beam in Figure 1 will be replaced with an integrated hybrid source. The project involves the development and production of hybrid lasers employing innovative resonant cavities. This design leads to densely spaced longitudinal modes within the laser cavity. To maintain single-mode operation, a high Q-factor photonic crystal cavity resonant mirror will be engineered, allowing only a single mode to fall within the reflection band. Stabilization of the longitudinal modes of the laser will be achieved by cladding a part of the silicon nitride waveguide with a material having a negative thermo-optic coefficient. The size of this cladding section will be selected to balance the positive thermo-optic coefficient of the gain chip.

Second, Project 2.2 “2D materials for hybrid laser wavelength tuning” led by Artem Vorobev [17], will provide the tunability to the hybrid-probe beam employing Graphene Electrodes (GE) in the fabricated optical devices. The project's core focus is the design, fabrication, and characterization of novel tunable lasers. These lasers will be based on silicon-nitride resonant cavities, like the ones designed for the 1.3 project, operating at wavelengths of 1.35 and 1.6 µm, and will incorporate monolayer and/or bilayer graphene sheets without compromising the cavity's Q-factor. The laser's design will prioritize tunability with minimal intensity modulation, thereby enhancing its utility as a spectroscopy probe source. When the resonant reflector is tuned, it alters the phase spectrum, affecting the roundtrip phase conditions and causing a shift in the lasing mode's wavelength.

On the other hand, project 3.3 “Trace water detection in organic solvents using PTS” carried out by Giovanna Ricchiuti [18] will explore the use of photothermal spectroscopy for liquids. The primary focus will be on maximizing the photothermal contrast between the solvent and analyte. To achieve this, the study will involve measuring traces of water (a potent IR absorber) in organic solvents (weaker IR absorbers). This may include photonic crystals and hybrid lasers, adapted for both excitation (pump beam) and readout purposes (probe beam). The choice of the operating wavelength will be optimized to minimize absorption by the liquid, and the devices will be redesigned accordingly. The liquid PTS system will be fine-tuned to accommodate the use of these components, contributing to the advancement of liquid-compatible photothermal spectroscopy.

Thus, project 3.3 will use the tunable hybrid source lead by projects 1.3 and 2.2 as a probe laser in a PTS system. Then the results discussed in this document will add the extra building blocks toward the demonstration of PTS on-a-chip for liquid samples: refractive index transducers, near-field enhancement for the pump beam, and liquid handling.

The research presented in this thesis aims to provide resonant structures that can be used as a refractive index transducer for the probe beam and as a source of near-field enhancement for the pump beam (See Figure 1). In concrete, it provides high Q-factor photonic cavities that can be integrated into a photothermal spectroscopy system [17]. The ability of high Q-factors to trap and confine light with minimal loss offers an ideal platform for exploring the potential to significantly enhance sensitivity, enabling the detection and characterization of samples

with increased precision. Besides, build on the proposed devices to add a liquid handling mechanism employing microfluidics for low quantities of sample.

Chapter 1 - HIGH Q-FACTOR PHOTONIC CAVITIES FOR PHOTOTHERMAL SPECTROSCOPY

Indirect absorption spectroscopy methods, such as photothermal spectroscopy (PTS) and photoacoustic spectroscopy (PAS), have the potential for sensor miniaturization. These indirect techniques detect changes in the thermodynamic properties of samples by examining alterations in the samples' refractive index (PTS) and detection of acoustic wave properties (PAS), respectively. In these methods, excitation lasers (pump beams) induce spectroscopic signals indirectly. The absorption of electromagnetic waves by molecules excites their internal energy levels, leading to sample heating through energy transfer by collisional relaxation. The resultant changes in sample temperature give rise to variations in density and pressure, ultimately generating PTS and PAS signals.

On the probe beam side, this research aims to provide refractive index transducers based on nanophotonic devices characterized by a high Q-factor, and low modal volumes. The first facilitates high-end transduction features for tracking the PTS signals, while the latter improves the overlap between the light and the sample within the interaction volume. In PTS, the alteration in temperature doesn't solely depend on optical power or energy; it also inversely relates to the volume in which the light is absorbed. This is because heat capacity scales with the quantity of substance involved [11]. Therefore, several designs that fulfill these requirements are computationally explored. Experiments conducted with fabricated devices demonstrate the feasibility of these new structures and pave the way for the miniaturization of PTS systems.

This work also explores all-dielectric resonant structures designed for mid-infrared (MIR) wavelengths, proposing an alternative approach to further enhancing the interaction between the analyte and the excitation source (pump beam). This approach inherently broadens the possibilities for miniaturization, applicable to both PTS and other direct spectroscopy methods.

The design and numerical validation of the proposed devices was carried out at Politecnico di Bari, utilizing available computational resources. Additional support was provided through ISCRA projects granted by the High-Performance Computing infrastructure of CINECA, Italy. Device fabrication took place at the facilities of the Tyndall National Institute, Ireland, while initial characterizations were conducted at Politecnico di Bari (Italy) and Munster Technological University (Ireland). Subsequently, the setup built at Technischen Universität Wien facilitated all subsequent experiments. In summary, this thesis aims to develop novel and advanced transduction interfaces to enable the miniaturization of PTS systems, contributing to the advancement of photonic sensing technology.

1.1. High Q-factor photonic cavities

Photonic sensors have a unique ability to resist specific physical parameters (e.g., immunity to EM fields) while retaining sensitivity to others, such as temperature, strain, and refractive index (RI) [13]. Consequently, their significance in contemporary science and technology is further increased by their application in different fields such as environmental monitoring and personal healthcare. Photonic sensors offer distinct advantages due to their compatibility with chip integration and use of CMOS technology, enabling the creation of compact and cost-effective devices [19–21]. Silicon Nitride (Si_3N_4) exhibits an extensive transparency range, spanning from visible to mid-infrared wavelengths, making it a versatile choice for a wide range of emerging applications. These applications include 3D photonic integrated circuits (PICs), nonlinear photonics, and biophotonics. The Si_3N_4-on-silica platform offers a substantial refractive index contrast, enabling efficient optical confinement within compact device footprints [22].

State-of-the-art nanophotonic biosensors could reach limits of detection down to 10^{-5}-$7{\cdot}10^{-7}$ RIU (Refractive index units) for Micro Ring Resonators (MRR) and 10^{-5} RIU for photonic crystals (PhC), respectively [12]. MRRs are made of a ring-shaped waveguide (WG) crafted from a high-refractive-index material like Si/Si_3N_4 and are coupled with a bus waveguide (WG). A photonic crystal corresponds with a synthetic modulation of the refractive index that is characterized by the axis of periodicities as 1D, 2D, or 3D. Both structures have shown excellent results in refractive index sensing [14,23].

MRRs with ultra-high intrinsic Q-factor have been released in Si_3N_4 MRRs with values of $4.22{\cdot}10^8$ [24] and lithium niobate (LN) MRRs with an intrinsic Q of $6{\cdot}10^6$ [25]. These metrics could provide, what is needed for precision spectroscopy on a chip. However, MRRs come with certain limitations that can impact their performance. One of the primary challenges is the bend loss of the ring. As light circulates through the device, these losses lead to increased attenuation, particularly when the light completes multiple round trips. These losses can significantly restrict the device's overall efficiency. The Free Spectral Range (FSR) of a MRR, which is determined by the ring's size and the refractive index of the material, sets the frequency range in which resonant modes can be supported. This can impose design limitations, affecting the device's versatility. Fabrication tolerances also play a crucial role. Even slight variations in parameters like the ring's diameter can cause shifts in resonance frequency and bandwidth. These shifts, in turn, lead to reduced device performance.

Temperature sensitivity is another challenge, as the resonance frequency of MRRs can shift with temperature changes. This sensitivity can be attributed to alterations in the material's refractive index, thermal expansion affecting the ring's dimensions, or thermal effects on the waveguide's effective refractive index. However, this can be beneficial in a PTS system, where the MRR can be used as a refractive index transducer to detect the absorption induced. In the mid-infrared wavelength range (3.25–3.6 µm), the optical absorption of an analyte is transduced by the intensity change of a MRR's optical transmission. This change is achieved through the thermo-optic effect of the employed material [26].

As an alternative, photonic crystal cavities can exhibit resonances with high Q-factor and high sensitivity in a more compact footprint [13]. Especially, in those systems where Silicon is involved. However, losses due to roughness are proportional to the refractive index contrast of the waveguide system used. Photonic crystal cavities attract great attention for their ultra-sensitive optical sensing and lab-on-a-chip applications, owing to their ultra-compact size,

ultra-small mode volume, and high integrability with bus-waveguides. Constant effort is made to optimize structures that can obtain high Q-factor and sensitivity for refractive index sensing. Therefore, to enhance the figure of merit (FOM) and to achieve a lower detection limit, various strategies have been proposed. These include exploring functionalized materials to reduce absorption loss, simplifying the functionalization process, and optimizing the structure towards nanobeam cavities. The interplay between the mechanism of coupling light into the structure and the geometry itself can ideally handle a single resonance. Alternatively, topologically protected optical modes can be useful for achieving single-mode operation photonic crystals. The topological state which forms at the interface between two lattices with different topological invariants, enables the generation of a single mode centered in the photonic bandgap and deals with the limitations imposed by FSR devices like MRRs [27]. This approach has been also explored with Fano resonances [28] and with III-V materials [29] for the realization of topological photonic crystal-based lasers.

Beyond the transduction device, measurement of small sample amounts is required. Today, lab-on-a-chip technology holds great promise for creating efficient sensing devices for analyzing gases and liquids for a wide range of applications. This approach requires conducting numerous measurements. To address this challenge, photonic integrated circuits (PICs) can be integrated with microfluidic channels (MFCs) for studying both liquids and gases. Recently, different concentrations of isopropanol in de-ionized water as the analyte have been used to evaluate the sensitivity (S) and detection limit (DL) of a system that includes Si_3N_4 MRRs [30]. The achieved experimental sensitivity was ~10^{-6} RIU. This advancement in MRR technology shows promise as a versatile platform for environmental monitoring and implementing point-of-care strategies in biomedical applications.

The role of a pump beam in PTS is crucial since the measured signal is proportional to the energy it delivers. Lasers can deliver substantial power levels or pulse energies within extremely limited optical bandwidths. This unique characteristic of lasers serves to increase the photothermal signals, contributing to their sensitivity. However, within the far field, constraints imposed by the conventional diffraction limit of light are encountered. In the near field, engineering significant gradients in the optical field at sub-wavelength scales can effectively overcome this limitation. Therefore, resonant nanostructures operating at the wavelengths of the pump beam can do the job. For instance, a sample's absorption band with a narrower full width at half maximum (FWHM) compared to that of the metasurface resonance, will result in resonant absorption enhancement.[31]

All-dielectric metasurfaces with resonant response offer the potential for flexible control of electromagnetic fields, facilitating the creation of advanced biosensors that enhance both device sensitivity and multiplexing capabilities [32]. Similarly, to confine electromagnetic energy within open subwavelength resonators, the concept of Bound States in the Continuum (BICs) is employed by achieving destructive interference between two leaky modes [33]. In parallel, metasurfaces based on BICs have found applications in lasing and high-harmonic generation [34]. Furthermore, applications in enhancing light-matter interactions for sensing purposes have been demonstrated [35]. For instance, mid-infrared molecular fingerprints for chemical identification and molecular analysis, have been experimentally demonstrated [21].

1.2. Aim of the Thesis

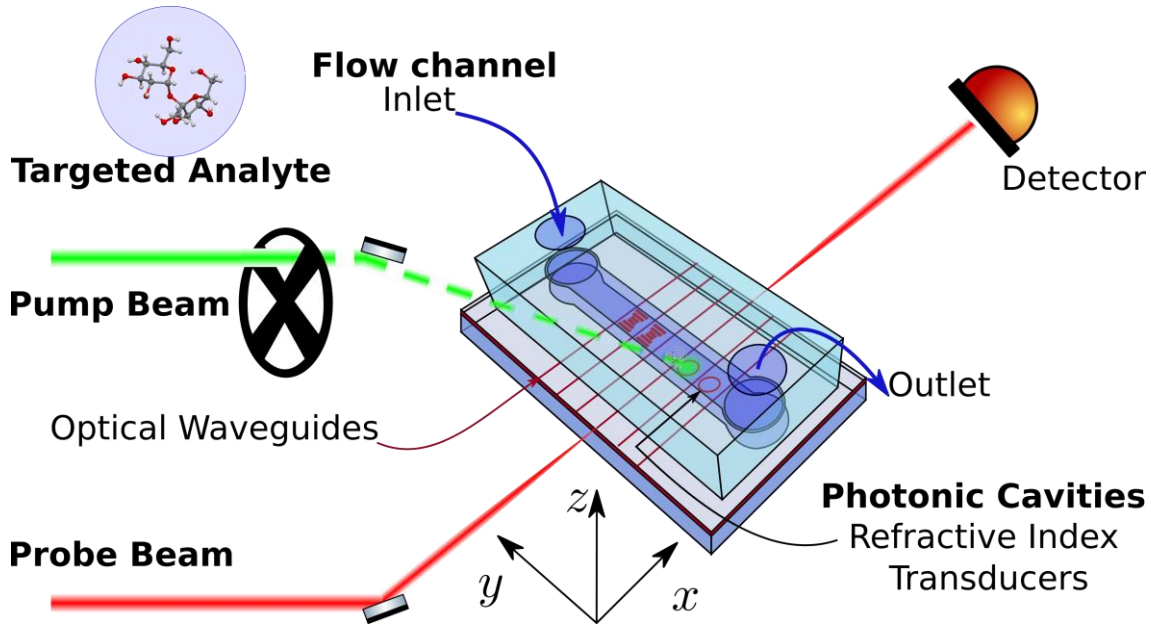

Figure 1.1 - Representation of the conducted research, highlighting the addressed aspects.

This research aims to investigate nanophotonic resonant structures for integration into a photothermal spectroscopy system. These nanostructures can serve as refractive index transducers, operating in telecom wavelengths (NIR), or as a mechanism for near-field enhancement at MIR wavelengths, among other potential applications. A visual representation of the intended research goal is presented in Figure 1.1.

Figure 1.1 can be divided into three different zones: (i) The one that refers to the probe beam, guiding light towards the photonic cavities. (ii) The flow channel where the target analyte circulates over the photonic cavities. (iii) The pump beam is directed towards the flow channel. These three aspects describe the organization of the activities outlined in this document and the efforts undertaken to advance toward a more compact photothermal spectroscopy system.

The first part of this work focuses on the design of refractive index transducers that can leverage the potential high-Q photonic cavities in the telecom wavelength range. Photonic Crystal Nanobeam Cavities (PhCNC) are explored in three prototypes that can enhance various features. In the first approach, a novel PhCNC is designed with an engineered cross-section that achieves state-of-the-art metrics in terms of Q-factor and sensitivity. This is demonstrated by its operation as a standalone and hybrid refractive index sensor. The second part addresses shape optimization of the unit cell of the cavity to tackle inaccuracies inherent in the fabrication process. In the third part, a slotted design is explored to compensate for the drops in the resonance linewidth in a resonator that is inherently highly sensitive.

Generation of Fano resonances based on Micro Rings is demonstrated. The shape of the resonance can be further exploited as an additional degree of freedom for sensing. Two variations of the design are explored and tested in different operational scenarios to underscore the achieved properties of these Fano resonators.

Subsequently, the integration of a microfluidic system is demonstrated through bonding onto a Silicon Nitride chip surface after a single etching process. The operation of the microfluidic cell for refractive index sensing is presented. Finally, the dissertation includes a discussion of

some of the numerical simulations conducted for the conception of metasurfaces designed for near-field enhancement in the context of MIR wavelengths.

1.3. Thesis Content

This thesis is organized as follows: Chapter 2 introduces fundamental concepts relevant to the discussion in this document, including Photonics Crystals Cavities and Micro Ring resonators. In Chapter 3, the approach for realizing Photonic Crystal Nanobeam Cavities as refractive index transducers is described. Chapter 4 delves into the details of achieving Fano resonances with Micro Ring Resonators. Chapter 5 presents the integration approach used to incorporate microfluidics for liquid handling on a Silicon Nitride chip. Analysis of preliminary results related to the application of the proposed transducers as refractive index sensors, is provided. Finally, Chapter 6 offers insights into the numerical results concerning the design of mid-infrared (MIR) metasurfaces. Besides, covers conclusions and outlines directions for future work.

Chapter 2 - FUNDAMENTALS

This chapter serves two primary objectives. First, it provides an introduction to the fundamental aspects of Photonic Crystal Nanobeam Cavities and Micro Ring Resonators. These topics are discussed in Chapters 3 and 4, respectively. Second, it offers a concise review of the applied electromagnetic models used to evaluate the implementation of the proposed photonic structures in this thesis.

2.1. Photonic Crystals Nanobeam Cavities

Photonic Crystal Nanobeam Cavities (PhCNC) employ a periodic dielectric structure, commonly referred to as a photonic crystal, to act as a mirror in one dimension [8]. This mirror function relies on destructive interference, preventing the propagation of light within specific frequency ranges (Photonic bandgap [37,38]), much akin to the operation of a distributed Bragg reflector (DBR). The Photonic Band Gap (PBG) allows the control of the flow of light in a photonic structure. The confinement of light in the other dimensions is achieved through total internal reflection (TIR). The establishment of a cavity within this system involves the introduction of a defect in the periodic structure. Such a defect can take the form of filling a hole or change of the dielectric [39]. This manipulation leads to the entrapment of photons with optical frequencies falling within the bandgap, effectively creating a cavity [36]. A description of the formation of PBG in 1D periodic crystal is presented in Appendix B.

2.1.1. Photonic Crystals

While the concept of one-dimensional (1D) photonic crystals, specifically nanobeam structures, was introduced over 25 years ago [40], they have only recently garnered substantial interest within the field of photonics [15,23,41]. These 1D photonic crystals exhibit periodicity exclusively along the axis of light propagation and primarily rely on the principle of total internal reflection to confine light in both the vertical and transverse dimensions. Figure 2.1(a-b) presents a Photonic Crystal Nanobeam Cavity on the substrate and a 2D Photonic crystal slab resonator undercut, respectively. Silicon-based device parameters of the PhCNC are reported in [42] while the 2D slab resonator is described in [43].

Regarding the 1D PhCNC shown in Figure 2.1 (a), the confinement mechanism can be understood as a distributed reflectance along x direction and index guiding along y, z. On the other hand, the 2D slab resonator in Figure 2.1 (b) possesses distributed reflectance in x, y, and index guiding along z. Figure 2.1 (c) shows the spatial distribution of the resonance mode electric-field energy (electric field in plane). The field distribution is taken through a slice at the center of the nanobeam cavity. Analysis of the Fourier components of the resonant mode (See Figure 2.1(d)) reveals that they are highly localized at the band edge of the Brillouin zone along the k_x-axis (where $k_x = \pi/a$). Figure 2.1(d), refers to the filled and dashed rings, which represent the light cone in the air and the substrate, respectively, at the band edge of the

Brillouin zone's band. The light cone corresponds to modes that do not meet the criterion of TIR [44]. This localization effectively minimizes the amount of mode energy within the light cone, which plays a crucial role in reducing scattering losses. Similarly, Figure 2.1(e) presents the spatial distribution of electric-field energy and is based on a slice taken through the center of the slab cavity in Figure 2.1(b). The Fourier components of the dominant magnetic component (electric field in plane) shown in Figure 2.1(f) are mostly distributed outside the light cone.

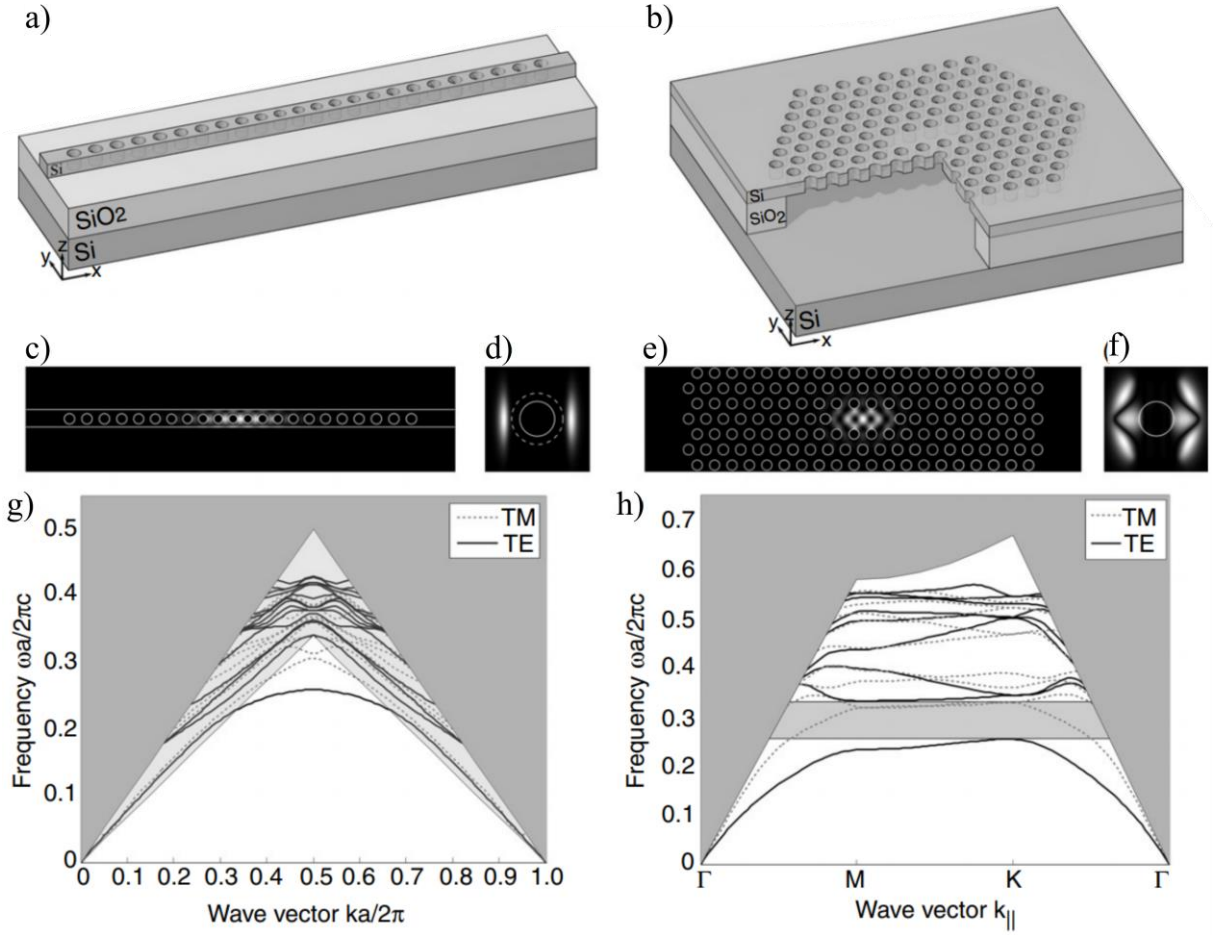

Figure 2.1 - Silicon-on-insulator **(a)** Photonic Crystal Nanobeam Cavity on a substrate [42] and **(b)** 2D Photonic crystal slab resonator undercut [43]. **(c)** The mode's electric-field energy distribution within the 1D PhCNC is shown in *(a)*. The structural details are overlaid on the illustration. **(d)** The 2D Fourier transform of the dominant magnetic component (H_z) of the mode presented in *(c)*. The solid ring indicates the light cone within the surrounding air medium, while the dashed ring represents the light cone within the SIO_2 substrate. **(e)** The mode's electric-field energy distribution of a 2D slab cavity, as depicted in *(b)*. The structural features are overlaid on the image. **(f)** The 2D Fourier transform of the principal magnetic component (H_z) associated with the mode displayed in *(e).* The solid ring depicted in the result corresponds to the light cone within the air medium. **(g)** The photonic band structure for the 1D PhCNC seen in *(a)* focusing on the region outside of the taper section (cavity). The vertical axis represents the angular frequency (ω), which is normalized to $2\pi c/a$, where c is the speed of light in a vacuum, and a is the lattice constant. The horizontal axis represents the wavevector along the propagation direction (k_x), which is normalized to $2\pi/a$. The dark region corresponds to the light cone observed in the air medium, while the lightly shaded area signifies the light cone in the substrate. **(h)** The photonic band structure for the 2D photonic crystal slab is seen in (b) focusing on the region outside of the cavity. The dark region corresponds to the light cone observed in the air. Modified from [45]

The physical origin of the photonic band structure relies on the coherent scattering of electromagnetic fields at the interfaces between distinct dielectric regions [36]. Figure 2.1 (g) presents the projected band structure of the PhCNC for the TE and TM modes (see Figure 2.1

(a)). The presence of transverse electric (TE) bandgap, which is situated between the peak of the lowest band and the edge of the substrate's light cone, is revealed. It is worthwhile noting the region within the TE bandgap that falls below the fundamental transverse magnetic (TM) mode and the presence of an overlapping TE/TM bandgap below the light cone. Therefore, dual-polarized PhCNC can be realized [46]. In a similar way to the previous case, the dispersion relation of the 2D slab photonic crystal is presented in Figure 2.1(h). The dark region denotes the light cone observed in the air medium, while the lightly shaded area indicates the TE bandgap, which exists between the first and second bands. It is important to highlight that in this context, there is an absence of overlapping TE/TM bandgaps.

The structural arrangement of 1D photonic crystal typically encompasses periodically repeating outer segments that function as Bragg mirrors, transitional segments, and a central defect that forms the cavity [15]. When working with a specific material system, the initial step involves selecting an appropriate periodic geometry for the mirrors. These regions are expected to display a photonic bandgap at the desired frequency and polarization, which signifies that the cavity mode will not propagate but instead decay exponentially within them. In a broader context, it is observed that taller structures composed of disjoint high-index regions tend to yield larger transverse magnetic (TM) bandgaps, while connected high-index regions usually result in more substantial transverse electric (TE) bandgaps. This distinction arises from variations in electromagnetic boundary conditions [36]. A comparison between structures with 1D PhCNC with and without substrate is discussed in [47].

In the design of photonic Crystal Nanobeam Cavities, a deterministic approach makes use of the band structure calculation [48,49], while the mode-matching [50,51] approach tries to optimize the whole parameter space. Both are thought to have a high Q-factor. The quality factor (Q-factor) serves as a metric for assessing the temporal confinement of light within a cavity. Mathematically, the Q-factor is defined as $Q = \omega_0 U/P$,[36] where ω_0 represents the angular frequency of the mode resonance, U quantifies the electromagnetic energy contained within the cavity, and P represents the rate of energy loss per unit time [44]. On designs where additional cavity length is not required, the cavity loss and the mode volume can be minimized simultaneously. The total cavity loss is a combination of two distinct components: radiation loss into free space (Q_{rad}) and coupling loss to the feeding waveguide (Q_{wg}). Increasing Q_{wg} involves adding more grating elements along the waveguide. Similarly, Q_{rad}, can be optimized by minimizing the cavity mode' spatial Fourier harmonics present within the light cone [48]. This is accomplished through the creation of a Gaussian-like attenuation profile. Most of the optical energy is densely concentrated within the dielectric region located at the center of the cavity, as visually depicted in Figure 2.1(c). To achieve the desired Gaussian-like attenuation profile, a proposed method is the implementation of a waveguide with a linearly increasing mirror strength, which is achieved by gradually tapering the hole radii [48].

Photonic crystal cavities can also be designed to achieve extreme light concentration, all while preserving the quality factor [52]. Through the strategic design of the photonic crystal unit cell and the introduction of minuscule dielectric inclusions well below the wavelength scale, it becomes possible to create a singular structure with a mode volume comparable to that of plasmonic elements. Plasmonic structures are recognized for their capacity to enhance the spatial confinement of light, as reflected by their small mode volume [53].

2.1.2. Refractive index sensing characteristics

The susceptibility of a cavity resonance mode to external perturbation (e.g. physical, biological, and chemical) directly impacts its inherent resonant characteristics, such as linewidth ($\delta\lambda$) and resonant wavelength (λ_0). The quality factor (Q) can be defined as the ratio of the central resonance wavelength of the cavity to its linewidth, expressed as $Q = \lambda_0/\delta\lambda = \omega\tau$. In this equation, ω represents the angular frequency, and τ is the photon lifetime of the cavity. A more extended photon lifetime implies a stronger interaction between light and matter. A higher Q results in a narrower resonance linewidth ($\delta\lambda$), which, in turn, dictates the system's ability to detect the smallest resonance shift ($\Delta\lambda$). On the other hand, the parameter V characterizes the cavity's capability to confine light. A smaller V indicates highly localized mode field distribution, significantly enhancing light–matter interactions. PhCNC can support both attributes with high Q/V which make them an exceptional platform for lab-on-a-chip optical sensing.

The sensing mechanism employed with PhCNC relies on the monitoring of resonance wavelength shifts triggered by refractive index (RI) changes induced by nearby analytes. These changes may be attributed to local disturbances resulting from analyte adsorption onto the cavity surface (e.g., protein adsorption) or global perturbations arising from variations in the bulk analyte concentration (e.g., different sodium chloride solution concentrations) or absorption-induced temperature changes [15,23]. According to the perturbation theory [36], the wavelength shift ($\Delta\lambda$) originated by an index perturbation (Δn) induced by surrounding analytes can be approximated as follows:

$$\frac{\Delta\lambda}{\lambda_0} \approx \frac{\Delta n}{n_0} \frac{\int_{V_{\text{analyte}}} \varepsilon(\mathbf{r})\,|\mathrm{E}(\mathbf{r})|^2 d^3\mathbf{r}}{\int_{V_{\text{total}}} \varepsilon(\mathbf{r})\,|\mathrm{E}(\mathbf{r})|^2 d^3\mathbf{r}} = \frac{\Delta n}{n_0}\Gamma_{\text{analyte}}, \tag{2.1}$$

where Γ_{analyte}represents the filling factor characterizing the distribution of the electric field energy within the surrounding analyte volume. Uniform RI change and constant unperturbed region is assumed. Moreover, in the context of nanoparticles or molecular detection [54–56] the wavelength shift can be formulated as follows:

$$\frac{\Delta\lambda}{\lambda_0} = \frac{3(\varepsilon_p - \varepsilon_s)}{\varepsilon_p + 2\varepsilon_s} \frac{|\mathrm{E}_{\text{mol}}|^2}{2\int \varepsilon|\mathrm{E}|^2 dr}\, V_{\text{mol}}, \tag{2.2}$$

where $\int \varepsilon|\mathrm{E}|^2 dr$ quantifies the total optical mode energy confined within the cavity, V_{mol} the volume of the nanoparticle, ε_p and ε_s represent the permittivity of the nanoparticle and the surrounding material, respectively. The relations presented in equation (2.1) and (2.2) indicate that an enhancement in the confinement factor (Γ_{analyte}) and a reduction in cavity volume (V) will result in a significant wavelength shift ($\Delta\lambda$). Therefore, an improvement in sensitivity is expected. The sensitivity is defined as follows:

$$\mathrm{S} = \frac{\Delta\lambda}{\Delta n} \approx \frac{\lambda_0}{n_0}\,\Gamma_{\text{analyte}} \tag{2.3}$$

where the overlapping between the analyte and the resonance mode (Γ_{analyte}) will be determinant to achieve high S. Therefore, the Figure of Merit, FOM is defined as:

$$\mathrm{FOM} = \frac{\mathrm{S}Q}{\lambda_0} \tag{2.4}$$

The Figure of Merit (FOM) experiences an impact due to the delicate balance between S and Q. Higher S requires the light mode to have a robust interaction with analytes, typically beyond the confines of the waveguide medium. Conversely, a higher Q demands that the light

mode remains more localized within the waveguide medium. Consequently, ongoing efforts are dedicated for realizing optimal geometries that effectively maximize both Q and S. This pursuit offers a promising foundation for achieving exceptionally low detection limits for sensing applications. Several configurations able to achieve both high-Q (>10^4) and high S (>300[nm/RIU]) are reported in [57]. Si_3N_4 has attracted attention as a viable substitute for Silicon-on-Insulator (SOI) platforms, due to its cost-effectiveness, compatibility with CMOS technology, and its relatively modest refractive index (n ~ 2). Besides, this material presents a reduced thermo-optic coefficient and a low two-photon absorption. The last is probably the most important due to it avoids self-tuning effects which would be detrimental to performance as a transducer. Several implementations of Silicon Nitride 1D photonic crystal nanobeam structures have been proposed [1,58–60].

In scenarios where PhCNCs are surrounded by absorbing materials, absorption events lead to the broadening of the cavity mode linewidth $\Delta[\delta\lambda]$ that can increase the detection limit to a single nanoparticle level. In such cases, the stringent requirements for ultra-high-Q are not necessary, and the sensing method becomes less sensitive to external disturbances like environmental temperature fluctuations. When compared to mode shift-based sensing, the mode broadening mechanism relies on the dissipative properties of analytes[61].

2.2. Micro Ring Resonators

An optical microring resonator (MRR) represents a compact and integrated optical device formed by curving an optical waveguide into a closed-loop configuration, frequently adopting a circular or racetrack shape. The fundamental operation of the MRR involves the interaction of light as it circulates within the waveguide, leading to interference patterns upon completing each circuit around the ring. Precisely when the roundtrip length corresponds to an integer multiple of the guided wavelength, it triggers constructive interference among the propagating light waves. This constructive interference results in the formation of distinct, sharply defined resonances and a significant amplification of light intensity within the microring [62–64].

2.2.1. Micro ring resonator

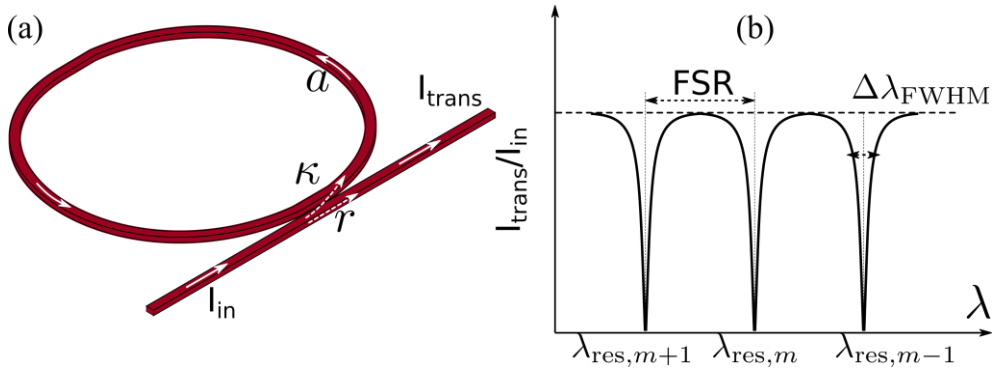

Figure 2.2 - (a) schematics of an all-pass micro ring resonator. (b) The corresponding Transmission function with some representation of the MRR performance criteria, including Free Spectral Range (FSR), Resonance linewidth ($\Delta\lambda_{\mathrm{FWHM}}$) at the $m-1$ resonance wavelength ($\lambda_{\mathrm{res},m+1}$).

The fundamental spectral characteristics of an all-pass ring resonator can be derived by considering continuous wave (CW) operation and ensuring field coherence. While this analysis assumes that reflections back into the bus waveguide are minimal (although this may not hold

in certain cases like a silicon wire [64]), the relationship between the transmitted and incident fields in the bus waveguide can be expressed as follows:

$$T(\lambda) = \frac{a^2 + r^2 - 2ar\cos\left(\frac{2\pi L n_{\text{eff}}}{\lambda}\right)}{1 - a^2 r^2 - 2ar\cos\left(\frac{2\pi L n_{\text{eff}}}{\lambda}\right)} \tag{2.5}$$

where n_{eff} corresponds to the effective refractive index of the waveguide, while L denotes the roundtrip length. The parameters r and a represent the self-coupling coefficient (transmission at the waveguide resonator coupling) and the single-pass amplitude transmission (inner circulation), respectively. The parameter a accounts for the combined effects of propagation loss within the ring and the losses occurring in the couplers. It links to the power attenuation coefficient (α[1/cm]) in the form $a = \exp(-\alpha L/2)$. Likewise, one can introduce the parameter κ to represent the cross-coupling coefficients. As such, r^2 and κ^2 stand for the power division ratios of the coupler. These ratios are assumed to adhere to the condition $r^2 + \kappa^2 = 1$, signifying the absence of losses within the coupling segment [64].

The resonant behavior of the ring can be determined by the phase ($\frac{2\pi L n_{\text{eff}}}{\lambda}$) relationship. Specifically, the resonance condition occurs when if the phase change over on roundtrip is a multiple of 2π or when the wavelength (λ) of the incident light completes an integer number of cycles within the optical path length, the ring reaches resonance:

$$\lambda_{res} = \frac{L n_{\text{eff}}}{m} \tag{2.6}$$

where m is an integer. In the absence of attenuation ($a \approx 1$), the transmission is perfect (unity) regardless of the detuning phase. In the case of critical coupling ($1 - a^2 = \kappa^2$ or $r = a$), the transmission at resonance diminishes to zero. The phase of the field transmission experiences periodic variations as a function of frequency. All-pass resonators effectively delay incoming signals through the temporary storage of optical energy within the resonator.

2.2.2. Refractive index sensing characteristics

The sensitivity of ring resonator sensors is highly influenced by their Q-factor. In particular is possible to link with the transmittance model of MRR, to have more insights into the device characteristics. This influence stems from the fact that a high Q-factor significantly reduces the impact of noise during the determination of the resonance wavelength, as supported by previous works [65]. Moreover, an enhanced Q-factor minimizes the smallest detectable wavelength shift contributing to a superior detection limit [65–69]. The Q-factor is determined by assessing the energy loss incurred in each resonant cycle relative to the energy stored within the ring. It is closely associated with the sharpness of the resonance peak. The energy loss primarily includes scattering loss, particularly at the sidewalls of the waveguide, and absorption loss stemming from the waveguide material. Consequently, enhancing the Q-factor of the ring resonator requires minimizing the energy loss. The Q-factor is predominantly influenced by both the coupling efficiency and the intrinsic optical losses [70,71]. The loaded Quality factor, Q_l, is defined as follows [70]:

$$Q_l = \frac{\lambda_0}{\Delta\lambda} = \frac{\pi\sqrt{ra}\, L n_g}{(1 - ra)\lambda_0} \tag{2.7}$$

where $\lambda_0(\lambda_{\text{res}})$ and $\Delta\lambda$ ($\Delta\lambda_{\text{FWHM}}$) represent the resonant wavelength and the linewidth of the resonance, respectively (see Figure 2.2). n_g denotes the group index by:

$$n_g = n_{\text{eff}} - \lambda \frac{dn_{\text{eff}}}{d\lambda} \tag{2.8}$$

The group index can be determined by calculating the difference between the wavelengths of two consecutive resonances, specifically using the free spectral range (FSR), as follows:

$$n_g \approx \frac{\lambda^2}{FSR \cdot L} \tag{2.9}$$

Alternatively, Q_l can also be written as:

$$\frac{1}{Q_l} = \frac{1}{Q_e} + \frac{1}{Q_i} \tag{2.10}$$

The coupling of optical power from the bus waveguide to the ring is quantified by Q_e, while Q_i represents the unloaded (intrinsic) quality factor. These values are expressed as follows:

$$Q_e = \frac{2Q_l}{1 - \sqrt{T_{\text{min}}}} \tag{2.11}$$

where T_{min} corresponds to the minimum amplitude in the normalized transmission spectrum. Then, if $r = 1$ then $Q_i = Q_l$. In other words:

$$Q_i = \frac{\pi\sqrt{a}Ln_g}{(1-a)\lambda_0} \tag{2.12}$$

Hence, by directly (e.g. experiment) measuring the Free Spectral Range (FSR) and utilizing Equation (2.9), one can determine the group index (n_g). On the other hand, when measuring the loaded quality factor (Q_l), the minimum point of the normalized transmission spectrum (T_{min}) and having the value of n_g, it becomes feasible to extract the parameters a and r from equations (2.7), (2.10-2.12). Additionally, when the critical coupling conditions are satisfied ($r = a$) the Field enhancement factor is given by $\text{FE}=(1-a^2)^{-1/2}$ [72]. Here, the maximum FE matches low propagation losses per roundtrip in the cavity. According to equations (2.5) and (2.7) decreasing radiation loss can enhance the Q-factor. Complementary, the utilization of a racetrack-shaped structure offers the advantage of maintaining a relatively stable coupling coefficient that can further improve the characteristics of the MRR.

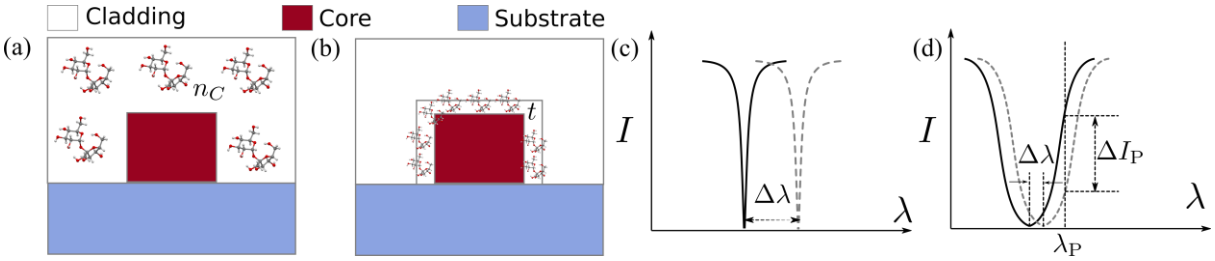

Figure 2.3 - Representation of (a) homogenous sensing where the analyte corresponds with the top cladding. (b) Surface sensing is where the analyte adsorbs on the waveguide surface as a thin layer. (c) Resonant wavelengths shift sensing scheme. (d) Intensity-based sensing scheme, where λ_P and I_P are the probe wavelength and Intensity, respectively. Adapted from [62]

Two fundamental sensing mechanisms find common usage in waveguides-based optical sensors: homogeneous sensing and surface sensing (see Figure 2.3(a-b)). In homogeneous sensing, the sensor is conventionally immersed in a sample solution, effectively constituting the top cladding (total surrounding volume) of the waveguide on a substrate. The uniformly dispersed analyte within this solution causes modifications to the bulk refractive index. This results in an alteration of the effective index of the guided mode. Under this mechanism, the effective index shift arises from all materials within the sample, lacking specificity. To address the lack of specificity, surface sensing comes into play. In surface sensing, the optical device

is preconfigured to possess receptors or binding sites on its sensor surfaces. These specialized sites can selectively interact with specific analytes in the sample, granting specificity. Furthermore, this approach offers higher sensitivity due to the presence of a more substantial evanescent field at the waveguide boundary, facilitating the probing of analytes by the evanescent field. When the sensing scheme, is based on detecting the refractive index variations several definitions for the sensitivity are possible depending on whether a decrease in intensity or a shift in resonant wavelength is measured. Table 2.1 presents a comparison between them and a detailed analysis is presented in [62].

Table 2.1. Sensitivity is defined in terms of the sensing mechanism and sensing scheme involved [62]. n_C is the refractive index of the cladding, t the analyte's cladding thickness and I the transmitted intensity.

		Sensing scheme	
		Resonant wavelength shift	***Intensity variation***
Sensing Mechanism	**Homogeneous**	$\mathrm{S} = \frac{\partial \lambda_{\mathrm{res}}}{\partial n_C} = \frac{\partial \lambda_{\mathrm{res}}}{\partial n_{\mathrm{eff}}} \cdot \frac{\partial n_{\mathrm{eff}}}{\partial n_C}$	$\mathrm{S} = \frac{\partial I}{\partial n_C} = \frac{\partial I}{\partial n_{\mathrm{eff}}} \cdot \frac{\partial n_{\mathrm{eff}}}{\partial n_C}$
	Surface	$\mathrm{S} = \frac{\partial \lambda_C}{\partial t} = \frac{\partial \lambda_{\mathrm{res}}}{\partial n_{\mathrm{eff}}} \cdot \frac{\partial n_{\mathrm{eff}}}{\partial t}$	$\mathrm{S} = \frac{\partial I}{\partial t} = \frac{\partial I}{\partial n_{\mathrm{eff}}} \cdot \frac{\partial n_{\mathrm{eff}}}{\partial t}$

In Table 2.1 the sensitivity, S, is defined in terms of the ratio between the change of the evaluated parameter (λ_{res}, I) and the change in the waveguide parameter affected by analyte (t, n_C). There, two distinct sensing schemes are possible as depicted in Figure 2.3(c-d). The most used approach involves the monitoring of resonant wavelength shifts induced by the analytes. This method offers a broader detection range, but it requires a more intricate experimental setup due to the need for wavelength-resolved measurements (tunable laser or Optical Spectrum Analyzer). In contrast, the latter approach retrieves variations in the output intensity at the wavelength exhibiting the steepest slope (e.g., Inflection point) within the transmission spectrum. This steep slope is capable of amplifying minuscule shifts in resonant wavelengths, resulting in a substantially detectable intensity variation. Consequently, this scheme has the potential to provide increased sensitivity and a simplified experimental setup that eliminates the need for wavelength-resolved measurements. However, it is exclusively effective when the monitoring wavelength closely aligns with the selected resonance, which, in fact, also presents a practical challenge.

Alternatively, a modified definition of sensitivity (bulk sensitivity $\partial \lambda_{\mathrm{res}} / \partial n_C$) is presented in [73]. The purpose is to provide a definition that allows comparison of resonators operating in different wavelength ranges by the ratio between the sensitivity of the resonator and its operational wavelength as follows:

$$\mathrm{S}' = \frac{\mathrm{S}}{\lambda_{\mathrm{res}}} = \frac{1}{n_g} \frac{\partial n_{\mathrm{eff}}}{\partial n_{\mathrm{c}}} \tag{2.13}$$

Another useful definition is the intrinsic limit of detection, which depends only on the intrinsic characteristics of the resonator:

$$\mathrm{iLOD} = \frac{\lambda_{res}}{Q\mathrm{S}} \tag{2.14}$$

Equation 2.14 is proposed in [74] giving a way of comparing the performance of RI sensors. In practical terms, there is a system limit of detection (sLoD) [68] linked to the specific readout instrumentation and experimental arrangement. The sLOD is proportional to iLOD, and it accounts for the minimum refractive index change necessary to cause a discernible modification in the output signal, surpassing three standard deviations (3σ) of the noise floor. Various factors play a role, including noise sources like the spectral and amplitude fluctuations of the light source, electrical noise originating from readout circuitry, and the level of thermal stability within the system. The application of scan averaging techniques can effectively mitigate noise effects. Due to the multifaceted nature of these system-related factors, conducting a genuinely objective comparison of sensors becomes a complex task, especially when they are characterized using diverse protocols and experimental systems. This statement is not limited to MRRs, the detection limit defined in equation 2.14 can also be applied to PhCNC [1,75].

In summary, optimizing sensor performance entails addressing several key considerations. In the case of homogeneous sensing by resonant wavelength shift, enhancing the light-analyte interaction by increasing the waveguide sensitivity ($\partial n_{\text{eff}}/\partial n_C$) will play a pivotal role in the overall sensitivity of the sensor. The presence of a high Q-factor is crucial for enhancing the sensitivity of ring resonator-based sensors. This high Q-factor serves to minimize the influence of noise on resonance wavelength determination, resulting in the reduction of the smallest detectable wavelength shift and, consequently, an enhancement of the sensor's detection limit. The miniaturization of the sensor, reducing its physical footprint, leads to shorter analysis times and brings about reductions in sample consumption and overall device costs. Moreover, compatibility with a semiconductor production platform enables the integration of sensor technology into industrial production workflows, offering the potential for scalable production and cost-effective refractive index sensors.

2.3. Summary & Perspective

Fundamental concepts related to the realization of Photonic Crystal Nanobeam Cavities and Micro Ring Resonators, including determinant characteristics for evaluating these integrated devices as refractive index sensors, have been examined. These photonic devices have emerged as powerful tools in the field of optics, offering unique and complementary capabilities for high-precision and ultrasensitive optical sensing applications.

Photonic crystal nanobeam cavities can confine light at sub-wavelength scales with small modal volumes and have demonstrated exceptional sensitivity to changes in refractive index, rendering them valuable components across various fields with applications, in refractive index sensing. A concise overview of photonic bandgap, two-dimensional photonic crystals, and photonic crystal cavities is presented. These elements possess numerous advantageous qualities, including precise wavelength control, high Q/V ratios (field enhancement), and a compact footprint.

The specific sensing scheme in use will also dictate the specific aspects that need to be emphasized for enhancing the sensing characteristics of Micro Ring Resonators, and photonic crystal cavities designs. This aspect is particularly important in the context of Photothermal Spectroscopy (PTS), where intensity variation schemes are typically employed. The intensity change scales proportional to the resonant wavelength shift. Therefore, high-sensitivity

refractive index sensors will be realized through improved spatial overlap of the resonant modes with the target molecule, and a steeper slope of the corresponding spectral feature.

Chapter 3 - Photonic Crystal Nanobeam Cavities

Optical cavities based on nanobeams exhibit exceptional characteristics, such as high-quality factors, low footprint, and mode volumes (V) at the wavelength scale [76]. These attributes establish them as the preferred choice for resonators in integrated photonics, enabling efficient light–matter interaction. This quality is particularly crucial for the realization of refractive index transducers, which could be included in a photothermal spectroscopy system [77]. The utilization of high-quality factor optical resonators holds significant importance across numerous photonic applications.

The majority of Si_3N_4 resonator designs documented in existing literature focus on free-standing PhCNC [58–60], where the substrate beneath the nanobeam is removed. Free-standing nanobeam cavities leverage the substantial refractive index contrast between the waveguide and a uniform environment (typically air) to achieve high Q-factors. Nevertheless, such devices exhibit limited compatibility with established semiconductor fabrication processes.

Implementing these resonators on a Si_3N_4 platform presents significant challenges due to the limited refractive index contrast achievable with this material system. Therefore, there is an ongoing effort to explore alternative geometries that do not require the use of free-standing configurations, while still maintaining their distinctive attributes [41,78]. In this chapter, various configurations of asymmetrically cladded silicon and silicon nitride 1D photonic crystal cavities are introduced and subsequently discussed for their potential as refractive index transducers. Additionally, their operation in a Hybrid External Cavity Laser (HECL) configuration is also demonstrated.

3.1. Engineered angled sidewalls

PhCNC structures encounter two inherent challenges when employed for refractive index sensing. Firstly, the limited overlap of the light field with analytes, as most of the light field remains confined within the high-index regions. Secondly, the obstruction of the sample fluids flows due to the specific geometry configuration, such as the 1D lattice holes [41,78]. As an alternative, several designs of Silicon PhCNC with remarkably high Q/V ratios have been documented, including the mode-gap cavity type [79,80]. Furthermore, hybrid integration with III-V materials through template-assisted selective epitaxy has been successfully demonstrated [81].

3.1.1. Design and Simulation

The Si_3N_4 PCNC design proposed here follows the stack mode-gap configuration, which involves the arrangement of a periodic array of Si_3N_4 rectangular structures separated by air (or another suitable upper cladding material). These gaps serve as wavelength-selective mirrors, like high-contrast Bragg gratings, situated on a SiO_2 substrate. The nanobeam cavity holds a parabolic-width stack, resulting in the creation of a defect within the photonic bandgap (PBG). This defect induces a Gaussian-shaped electric field distribution along the cavity, effectively minimizing optical losses [49]. This smooth perturbation enhances the mirror's reflective capabilities resulting in a very strong light confinement [51]. A schematic of the proposed structure is presented in Figure 3.1.

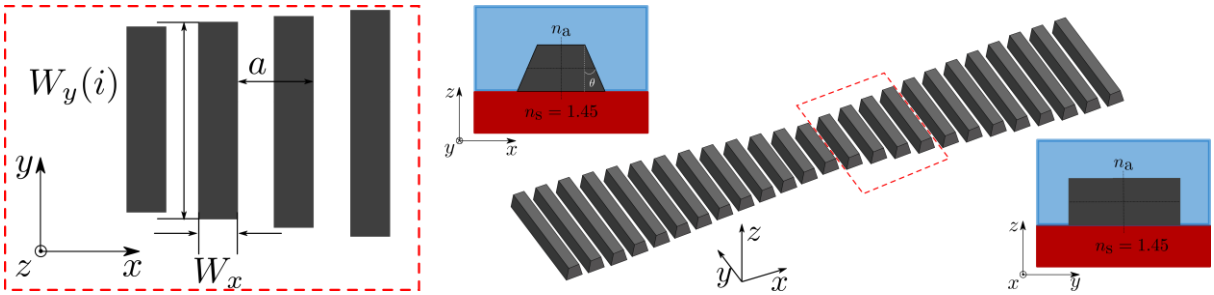

Figure 3.1 - Silicon Nitride Photonic Crystal Nanobeam Cavity with parabolic-width stack and engineered side walls. The vertical width of the stacks ($W_y(i)$) is modulated based on equation 3.1. The horizontal width W_x remains constant. The upper cladding, with refractive index n_a, is uniformly distributed in the surrounding volume. The structure is placed on a SiO_2 substrate with refractive index n_s. Note that (n_{upp}=n_a).

The local modulation of the stack width is defined by the following equation:

$$W_y(i) = W_y(0) + \frac{i^2}{i_{\max}}[W_y(i_{\max}) - W_y(0)], \tag{3.1}$$

where $W_y(i)$ is the width of the i^{th} dielectric block, referred to as nano-stick, extending from the central stick position (i=0) to both sides positions of the cavity ($i = i_{\max}$). Therefore, $W_y(0)$ and $W(i_{\max})$ correspond with the vertical width (y-axis) of the central and last stick at both ends of the PhCNC, respectively. The central stick width is determined by $W_y(0) = 3a$, while the side stick width is defined by $W_y(i_{\max}) = 2W_y(0) = 6a$. The lattice constant is represented by a, while the stick length W_x remains constant. Modulating the widths of the sticks along the y-axis offers a significantly wider range for refractive index modulation in contrast to the x-axis. This limitation in the x-axis results from fabrication constraints arising from the sub-micrometer features of the PhCNC's sticks, while the y-direction allows for more substantial width variations. The optimization of the quadratic tapering was carried out by calculating the Q-factor under various upper cladding refractive indexes ($n_{upp} = n_a$) scenarios [82].

Figure 3.2(a) and (b) illustrate the trends in cavity Q-factors and resonant wavelength shifts as the upper-cladding refractive index increases. In this context, the upper cladding refers to the environment above (analyte) the PhCNC, as indicated in the inset of Figure 3.1 and labeled with $n_a(n_{upp})$. The curves in Figure 3.2(a) depict Q-factors ranging from 10^5 to 10^7 for various upper-cladding configurations, with the red curve demonstrating the highest Q-factor values at refractive indices of 1.00 and 1.45, corresponding to the air-clad and SiO_2-clad architectures. Achieving a high Q-factor in a broad range of refractive indexes that mimics gases and liquids indicates the suitability of the proposed device for multi-environment operation.

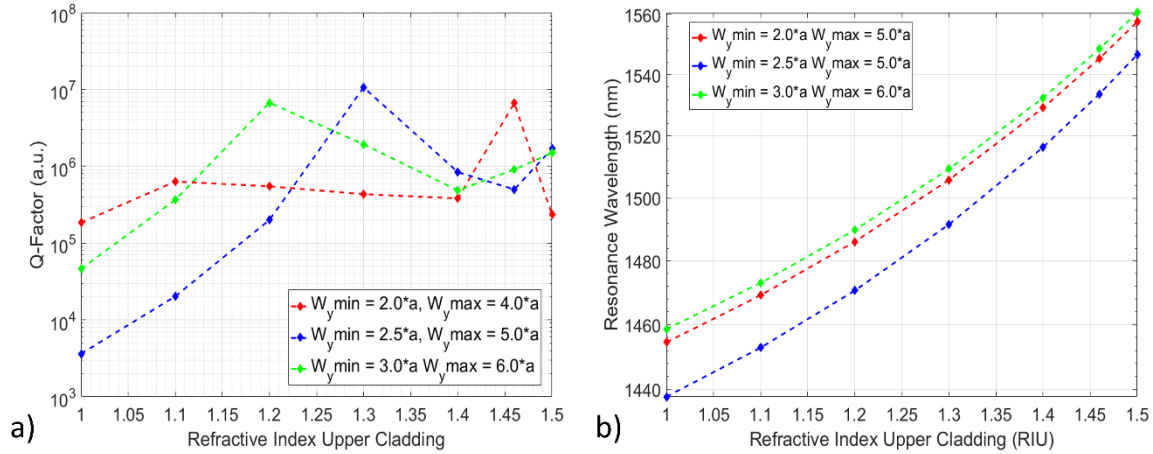

Figure 3.2 - (a) Calculated Q-factors for several upper-cladding refractive indices ($n_{\mathrm{upp}} = n_a$). Each Q-factor curve corresponds to a distinct quadratic tapering law defined by the initial and final Si_3N_4 stick widths, denoted as $W_y\mathrm{min}$ and $W_y\mathrm{max}$, respectively. (b) The calculated resonant wavelengths were determined while varying the refractive index of the upper cladding (n_a) in the various tapering configurations in (a) [1].

In addition to the modulation of stick widths ($W_y(i)$), the intrinsic Q-factor is linked to the number of periods within the cavity (also referred to as Gaussian mirror segments)[80]. This relationship involves the interplay between the periodicity of the PhCNC (a) and the length of the sticks (W_x) along the propagation direction (*x*-axis). In particular, the highest Q-factor values are achieved when there are about 90 or more mirrors segments (sticks) on each side of the central stick [1].

The changes in the quadratic tapering profile are observed to produce a linear augmentation in mirror strengths, a necessity for the attenuation of Gaussian fields. Besides the periodicity (a) among all the devices is constant due to it minimizes the cavity loss and the mode volume simultaneously. The influence of the refractive index in cladding seems to modulate the optimal condition to achieve the Gaussian-like attenuation of the electromagnetic field along the cavity resulting in variable performances. Therefore, the zero-cavity length, fixed periodicity, and a quadratic tapering of the filling fraction results in a Gaussian field profile, which leads to a high-Q cavity. Besides, consider that the dielectric band-edge frequency of the central mirror segment is used to determine the position of the resonant mode. Large width ($W_y(i)$) increases the effective index of the cavity mode, and pulls the mode away from the substrate light line, thus reducing the in-plane radiation loss. On the other hand, a large beam width will allow for higher-order modes with the same symmetry as the fundamental mode of interest.

The PhCNCs considered in this section have been specifically designed for a 300 nm thick Si_3N_4 platform with a refractive index ($n_{Si_3N_4}$) of 2.00, operating within the telecom band, and placed on a 2 µm thick layer of borosilicate glass (BOx) with n_s = 1.45. The thickness was chosen to match the laser mode area. Under the latter conditions, the influence of the nano-stick length along the x-axis (W_x) and the periodicity (a) on the Q-factor was studied using finite difference time domain (FDTD) calculations [82]. Throughout this optimization process, the ratio W_x/a remains ≤ 0.5 have been ensured. Description of used computational methods and software are presented in Appendix A.

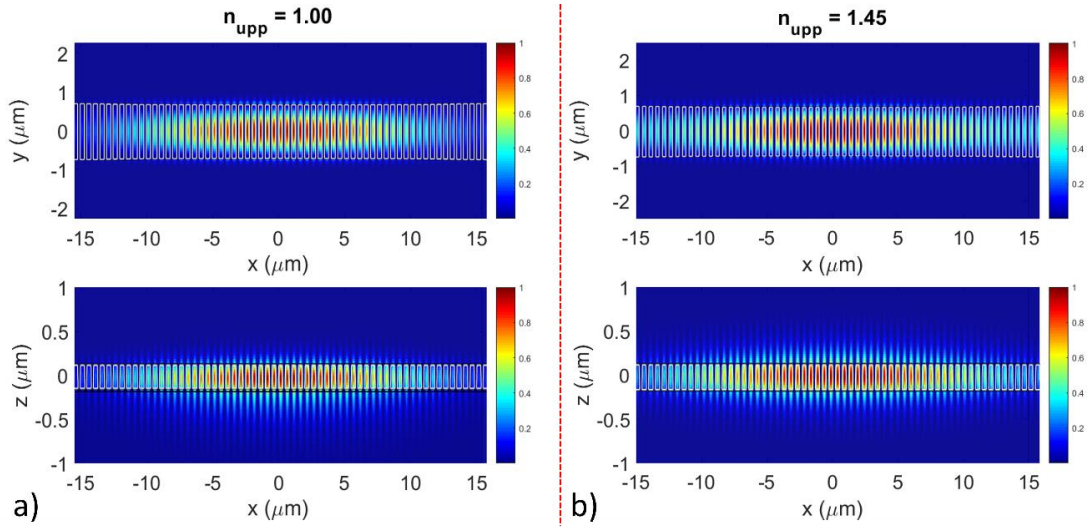

Figure 3.3 - Calculated electric field distribution of the optical mode in one of the proposed PhCNC for the *xy* and *xz* planes, considering two scenarios: (a) air upper-cladding and (b) SiO_2 upper-cladding.[1]

Figure 3.3 shows the optical mode confinement within the cavity in both air-clad and silica-clad configurations. The electric field distribution presented in this figure highlights the effective confinement of optical modes within the cavity in both the *xy* and *xz* planes. The portion of the optical energy distributed in the upper cladding further increases the interaction volume between the resonant modes and the samples, expanding in an area of 40µm^2 (*xy*-plane) for prospective refractive index sensing operation. For instance, the calculated field distribution in Figure 3.3(b) corresponds to a calculated Q-factor of ~70·10^6 in the silica-cladded architecture.

Analysis of the distribution of the electric field of the optical mode to assess the proportion of the field situated above the buried oxide substrate, which serves as the sensing volume, was conducted. This analysis involved dividing the 3D simulation space into 2D slices within the *xz* plane and calculating the optical mode fraction using the electric field data from each slice, following the definition of Γ_{analyte} in section 2.1.2. The electric field of the optical mode is predominantly confined over the substrate in all configurations, with over 70% of the field localized in this region.

To further assess the design of the PhCNC, the projected band structure ($\omega(k_x)$) for the tapered nano-sticks is numerically investigated. This calculation assumes translational symmetry (*x*) of the device (infinite array) to compute the eigenmodes of mirror segments, which are the electromagnetic waves that can propagate through the structure with a defined frequency [83]. Therefore, nano-sticks with vertical widths ($W_y(i)$) among the parabolic-width stack, from 1.4µm to 2µm, are selected while W_x remains constant. The complete band structure of each unit cell has been computed for TE modes (in-plane) within the reduced Brillouin zone, as illustrated in Figure 3.4.

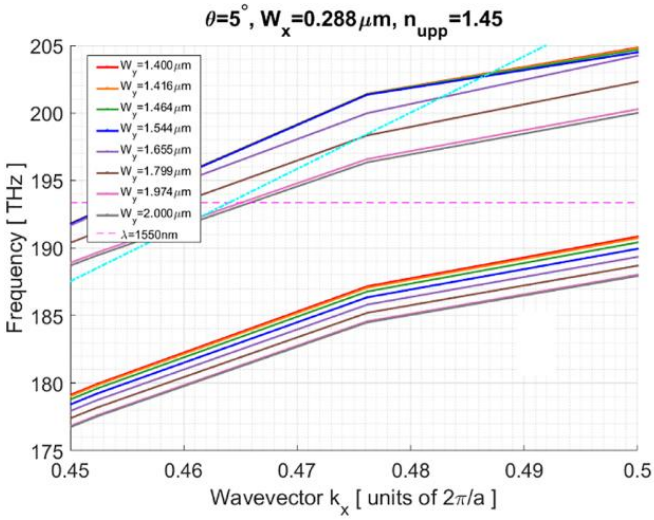

Figure 3.4 - Photonic band diagram of the angle sidewall PhCNC with SiO_2 cladding. The turquoise and green dashed lines correspond to the Silica and air light lines, respectively [1].

The band structure calculation aligns with the results presented in [47,49], where the cavity resonance lies within the band gap, close to the band-edge mode [36]. As observed in the plots, the W_y tapering of the nano-tick induces a shift and narrowing of the bandgap, resulting in mode confinement within the PhCN cavity. Propagating modes located at the edges (but external to) the bandgap in the ideal PhCNC with W_y = 1.4µm, become confined within the bandgaps of PhCNC with larger W_y values. This leads to the coupling of supported propagating modes into the center of the tapered PhCNC, where they are subsequently reflected back and forth inside it. The other edge sticks, with larger W_y values, effectively functioning as mirrors. It's important to note that the modes coupled into the cavity center become forbidden modes for the lateral mirror segments of the PhCNC (the lateral nano-sticks). Additionally, variation in W_x and upper cladding (n_{upp}) is also considered for further details refer to [1].

In the ongoing development of the asymmetrically cladded PhCNC design, further analysis into the response of the PhCNC system to changes in upper-cladding refractive indexes and Si_3N_4 stick sidewall angles, was conducted. The sidewall angle can mimic the tapering produced by the dry etch process. This effect has been explored in [84,85] revealing that high Q PhC cavities with hole tapering (angle sidewalls) can be achieved without the need for a complete TE-TM photonic bandgap. The Q-factor is influenced by coupling between the TE-like and TM-like modes [84,85] in asymmetric configurations where the out-of-plane symmetry is broken. The hypothesis is that the sidewall angle influences the overlap of the TE mode with one of the Si_3N_4, reducing TE-TM mode conversion. Therefore, how the PhCNC cavity responds to changes in upper-cladding refractive indexes and sidewall angles, was also examined.

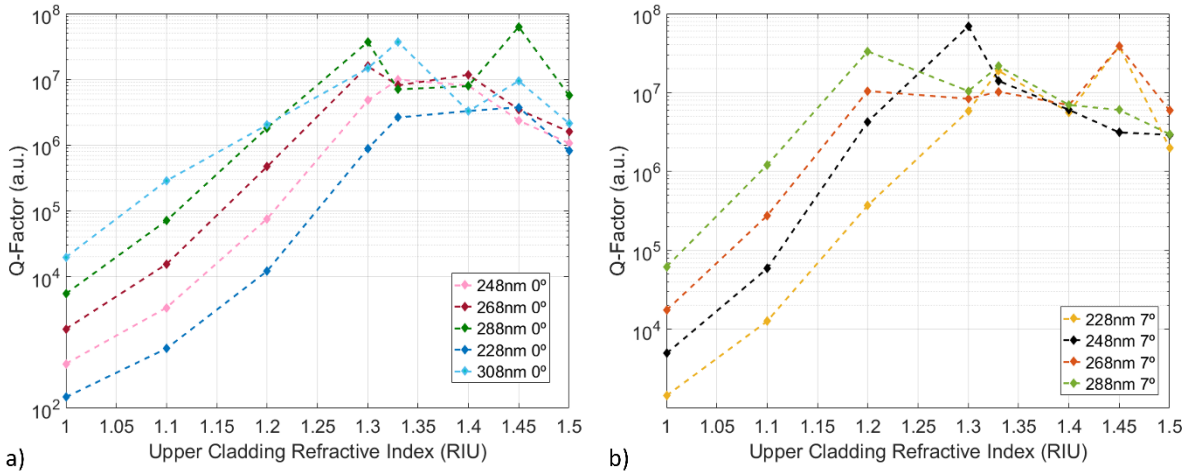

Figure 3.5 - Simulated Q-Factors of PhCNC with increasing upper-cladding refractive index. Each curve represents a cavity with a distinct nano-stick width, W_x, under two specific sidewall conditions: (a) 0 degrees and (b) 7 degrees. These configurations correspond to the measured cavity geometries [1].

The Q-factor trends for 1D Photonic Crystal (PhC) cavities with varying silicon nitride (SiN) stick width (W_x) and etching angles (0º, and 7º) configurations are depicted as a function of increasing upper-cladding refractive index, ranging from 1 to 1.5, as illustrated in Figure 3.5(a) and (b). These Q-factor trends exhibit bell-shaped curves, reaching their peak values in the vicinity of 10^8. The calculated data reveal a shift in the peaks of the Q-factor curves toward lower upper-cladding refractive indexes as the sidewall angles increase. This observation indicates that trapezoidal structures favor more asymmetric cladding configurations. It is important to note that, compared to rectangular stick configurations, Q-factor curves exhibit broadening and flattening with higher sidewall angles, enabling the attainment of high Q-factor values (≥10^6) across a broader range of upper-cladding refractive indexes. For instance, in Figure3.5(b) the configuration with W_x=288 nm and θ=7° cover the upper cladding RI range from 1.1 to 1.5, offering the potential to customize the desired cavity optical performance by manipulating the Si_3N_4 stick sidewall angles.

An increase in sidewall angle results in a slight shift of the bandgaps to lower frequencies. Furthermore, the bandgaps associated with trapezoidal sticks show a slight broadening [1]. The confinement of optical modes and the behavior of Q-factors in PhC cavities with asymmetric cladding and sidewall angles are significantly influenced by TE-TM mode coupling, which serves as a predominant loss mechanism. Consequently, the optical performance of PhC cavities exhibits distinctive asymmetric peaks (see Figure 3.5) corresponding to changes in cladding refractive index [84–86].

The influence of sidewalls breaks the vertical reflection symmetry of the structure, allowing confined TE-like cavity modes to couple to the resonant continuum of lossy TM-like modes. Previously for the case of 2D photonic crystal cavities with tapered airholes was found that the relation between the thickness and the taper can restore the original high Q-factor in the symmetric case [84–86]. For the given application, is feasible to think that the current thickness (300nm) exists an optimum angle sidewall that can restore the high Q factor. The optical loss of the cavity in an index-asymmetric structure occurs mainly in the in plane slab, because of TE-TM mode conversion.

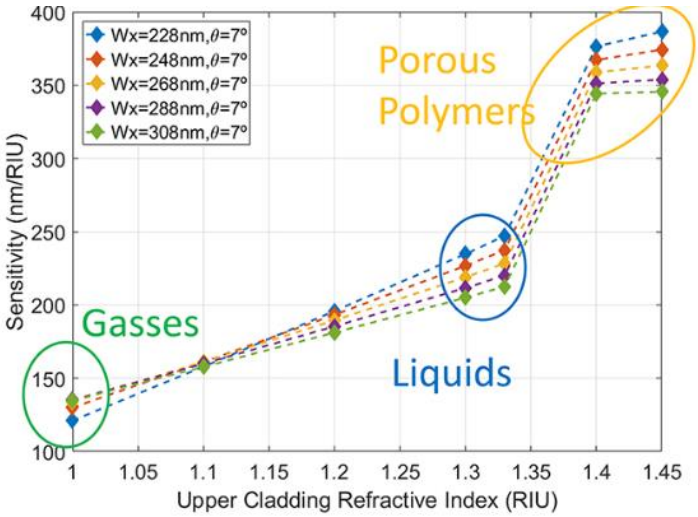

Figure 3.6 - Calculated sensitivity trend concerning the increasing upper-cladding refractive index for various nano-stick widths, W_x, and a sidewall angle of 5 degrees [1].

The RI sensitivity as a function of the upper-cladding refractive index was assessed by varying the stick width parameter in three different sidewall angle configurations (0°, 5°, and 7°) [1]. The sensitivity for the 5° sidewall angle configuration is presented in Figure 3.6. The sensitivity values are in the range of hundreds of nanometers per refractive index unit (nm/RIU) across the entire studied refractive index range (1-1.45). Specific attention was paid to refractive index ranges around 1 for gas sensing (e.g., air), near 1.33 for liquid sensing, and over 1.33 for porous polymers like SU8. While all geometries demonstrated high performance over the simulated upper-cladding refractive index range, the configurations with W_x = 308 nm and 7°, W_x = 248 nm and 7°, and W_x = 228 nm and 0° were found to be optimal for upper-cladding refractive index values of 1 (for gases), 1.3 (for liquids), and 1.4 (for spin-coated polymers), respectively.

The detection limit, as defined in Equation (2.14) in Section 2.2.2 was calculated across the entire investigated upper-cladding refractive index range. Detection limits as low as 4.6 x 10^{-5} RIU and 1.1 · 10^{-7} RIU were determined for upper-cladding refractive index values near 1 (for gases) and 1.3 (for liquids), respectively. These results were obtained with W_x set to 308 nm and sidewall angles of 5° and 7°.

The performance of the isolated cavity configuration has been discussed above. However, a crucial element of any integrated optical sensor device involves the injection and detection of light into and from the cavity. To achieve this, various approaches for accessing the PhCNC via a strip waveguide have been extensively explored. These investigations aim to identify the optimal solution in terms of optical performance, ease of fabrication, and characterization. Hence, the examination of the coupling mechanism to regulate the spatial modes excited in the waveguide-PhCNC is numerically and experimentally explored [87,88]. The side-coupled mechanism through a weakly tapered gap, led by an S-bend waveguide-cavity system, has been fabricated [1]. The manufactured configuration is shown in Figure 3.7(c).

3.1.2. Fabrication and Experimental Results

The integrated waveguide-PhCNC structures were manufactured at Tyndall National Institute in Cork, Ireland, utilizing conventional nanofabrication procedures and led by Simone Iadanza. These procedures were carefully adapted to ensure the required sidewall smoothness and verticality. In this study, the fabricated PhCNCs were designed to operate within the telecom

wavelength range between 1500 nm and 1600 nm, for characterization using the available optical setup. Details of the fabricated devices are presented in Figure 3 for both rectangular and trapezoidal cross sections.

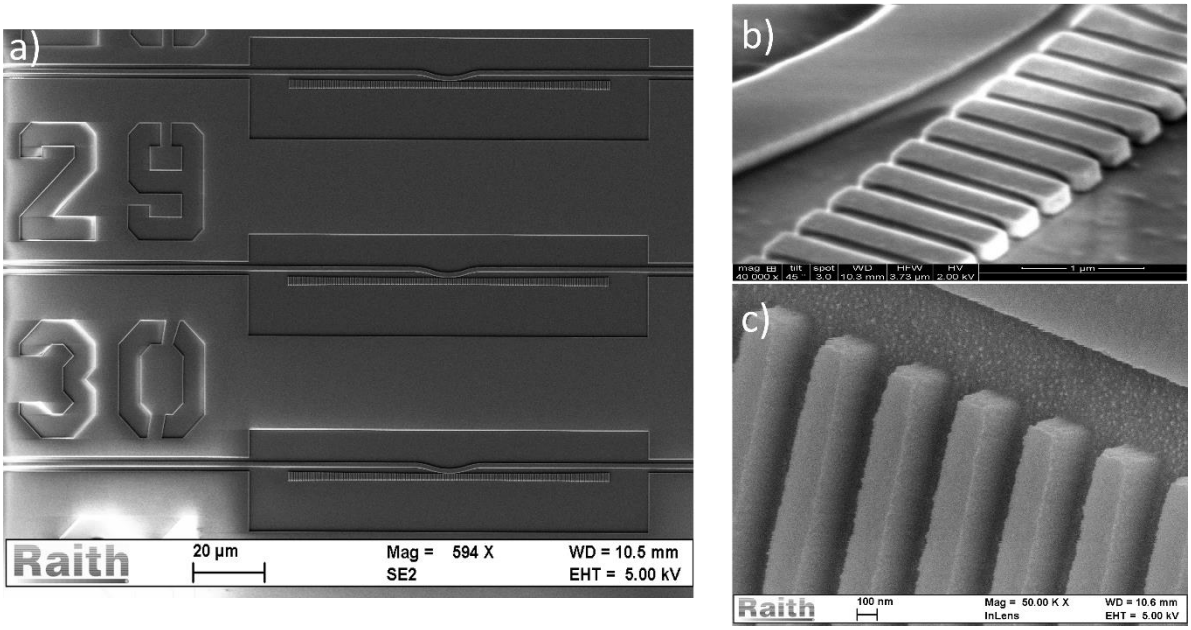

Figure 3.7 - (a) A scanning electron microscopy (SEM) image of the devices captured perpendicular to the chip surface using ZEISS equipment. (b) A ZEISS SEM image showcasing the rectangular cross-section devices, taken from a 45° angle. (c) An SEM image captured using Quanta equipment, displaying a device with trapezoidal cross-section sticks, also imaged from a 45° angle. The Fabrication work was done in conjunction with Simone Iadanza.

For device fabrication, firstly, a 450 nm thick layer of ZEP 520A resist was spin-coated onto a 300 nm thick Si_3N_4 layer deposited via Plasma Enhanced Chemical Vapor Deposition (PECVD). Subsequently, device layouts were imprinted onto the resist using Electron Beam Lithography (EBL) and then developed in a bath of n-Amyl Acetate solution. The patterns were subsequently transferred to the PECVD Si_3N_4 layer via an inductively coupled plasma (ICP) etching process involving SF_6:CHF_3 chemistry. Any remaining resist was later removed through an O_2 plasma ashing procedure, followed by immersion in a solution of 1165 Remover. The smoothness and verticality of the stick sidewalls were meticulously controlled by adjusting both the ICP power and etch pressure, ultimately achieving etching angles (θ) of 0° at etch pressures of 2.5 mTorr.

3.1.2.2. Passive measurements

Passive measurements were performed on the set of fabricated devices that better suited the comparison with the features predicted by the FDTD simulation. Passive measurements refer to the natural optical response of devices, to the input laser source without any gain medium involved. Thus, the fabricated pairs' sidewall angle and upper-cladding refractive index, (θ,n_{upp}), are 0°-SOG (n∼1.4), followed by 7°-SOG, then 7°-AIR and lastly 0°-AIR. The Q-factors of all the fabricated devices were determined by fitting each optical resonance with a Lorentzian function. The measured values fell within the range of $5{\cdot}10^3$ to $9{\cdot}10^4$, with the highest recorded Q-factor being $9{\cdot}10^4$. The best performance was observed in the group with SOG clad devices at 0° being consistent with the FDTD simulations.

The operational principle of the 1D PhC cavity refractive index sensor was evaluated by assessing the optical response of the air-clad devices (with a sidewall angle of θ = 7°) when

exposed to de-ionized water or a 10% aqueous sucrose solution. The liquids were applied to the top of the fabricated PhCNC using a microliter pipette via drop-casting. During these measurements, the sample was kept at a constant room temperature (T_{room} = 20.1 °C) by employing a Peltier element integrated into the aluminum sample holder. Figure 3.8 (a) presents a schematic representation of the experiment, where the fabricated PhCNC is surrounded by the target molecules that depending on their concentration will modify the bulk refractive index of the upper cladding. Figure 3.8(b) shows in red the measured spectra of the PhCN when surrounded by 10% aqueous sucrose solution.

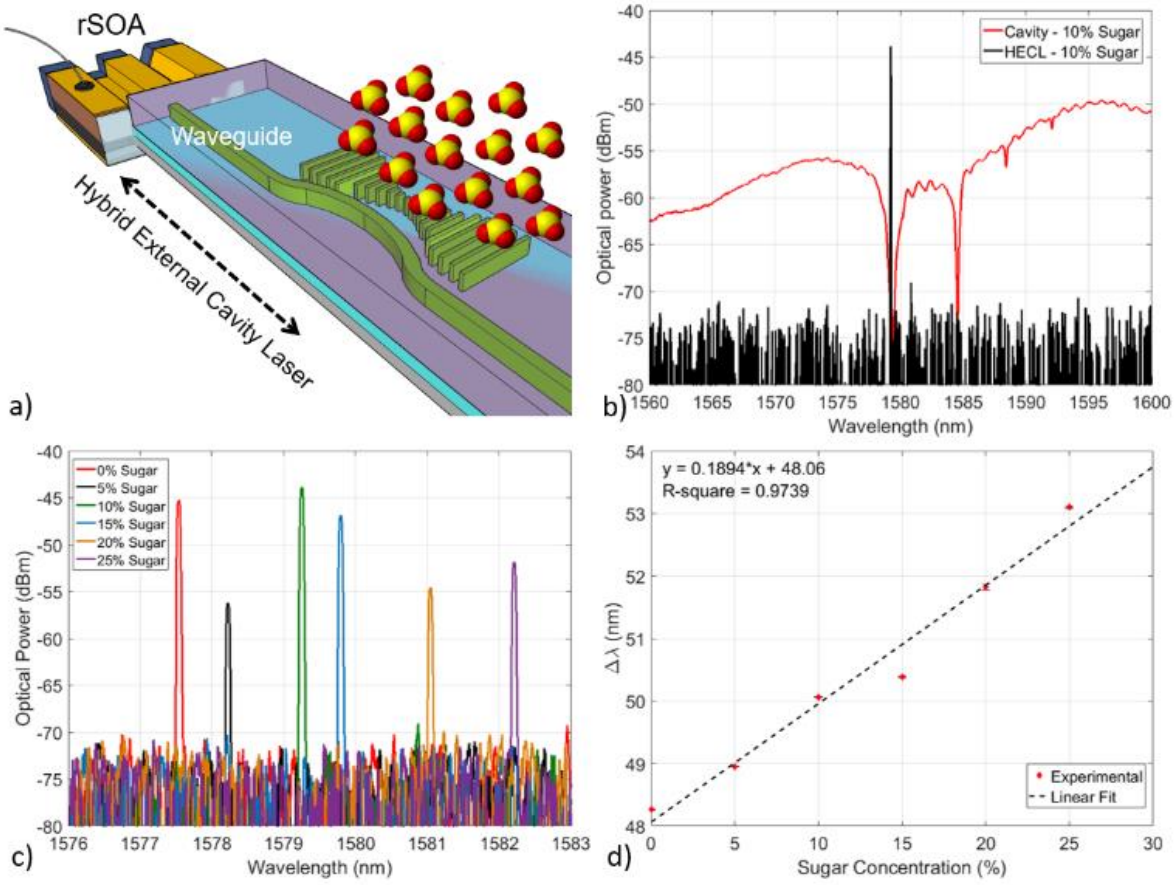

Figure 3.8 - (a) Schematic of Hybrid External Cavity Laser (HECL). (b) Overlap between the HECL lasing wavelength and the transmission dip of the transmission measurement in the PhCNC. (c) Lasing spectra of the HECL refractive index sensor in solutions of deionized water and increasing concentration of sucrose ($C_{12}H_{22}O_{11}$ – the most common form of sugar). (d) The related Calibration curve [2]. The experimental measurements were done in conjunction with Simone Iadanza and Taynara Oliveira.

A significant and rapid shift in the wavelength of the resonant modes towards longer wavelengths (redshift), while the fundamental modes maintained a high Q-factor, is validated by the experiment. This outcome aligns with the anticipated behavior for this specific device architecture. Notably, the resonance wavelength experiences a redshift as the sucrose concentration increases from 0% to 5%, 10%, 15%, 20%, and 25%. The microcavity employed for these measurements possesses a stick width (W_x) of 248 nm and a sidewall angle of 7°. The Q-factor of the measured resonance also increases from approximately 10^4 to around 10^5 as the refractive index (RI) of the solution rises. Specifically, the RI shifts from 1.33 for de-ionized water (DIW) to over 1.355 for sucrose concentrations above 15%. This trend aligns with the observations from simulations conducted with the same microcavity geometry. The sensitivity measured for this microcavity is approximately 150 nm/RIU, resulting in an experimental detection limit of 1.1 $\cdot 10^{-3}$ RIU.

3.1.2.3. Active measurements

Following the characterization of the optical performance of the nanocavities, a laser-based refractive index sensor concept utilizing these nanocavities is illustrated in Figure 3.8(a). This sensor incorporates a commercially available reflective semiconductor optical amplifier (rSOA) butt-coupled to the waveguide connected to the photonic crystal (PhC) cavity on the silicon nitride chip (Figure 3.8(a)), creating a hybrid external cavity laser (HECL) configuration [89].

As depicted in Figure 3.8(b), the emitted wavelength of the Hybrid Electrically Pumped Photonic Crystal Nanobeam Cavity Laser (HECL) must align with the PhCNC cavity reflection band. Since a portion of the PhCNC mode extends into the cladding, the laser device becomes highly susceptible to changes in the cladding material. Therefore, Figure 3.8(b) presents the spectra overlapping of the PhCNC with 10% aqueous sucrose solution in a passive and HECL configuration.

The lasing characteristics of this Si_3N_4 1D PhC cavity-based HECL reveal an output power in the milliwatt (mW) range and a stable single-mode lasing regime with minimal hopping across a wide range of injected currents (ranging from 25 to 65 mA), achieving a Signal-to-Mode Suppression Ratio (SMSR) of 40 dB.

During the exploration of the HECL's potential as a refractive index (RI) sensor, the analysis focused on the lasing wavelength's response to the introduction of sucrose solutions. These findings reveal a consistent and linear redshift in the wavelength as the sucrose concentration ranged from 0% to 25%, as illustrated in Figure 3.8(c) and Figure 3.8(d). The transition of the surrounding medium from one concentration to another results in a change in the upper-cladding refractive index (RI), which causes a redshift in the resonance wavelength of the PhCNC. Consequently, the lasing wavelength of the HECL is also shifted. The sensitivity of the passive cavity and HECL is similar ~150nm/RIU. Nevertheless, the HECL lasing line, characterized by a Q-factor exceeding $1.1 \cdot 10^5$ (constrained by the optical spectrum analyzer's resolution), exhibits a significantly narrower profile than the linewidth of the passive microcavity resonance (Figure 3.8(b)). Consequently, the HECL-based sensor reached an experimental detection limit of approximately $6.6 \cdot 10^{-5}$ RIU.

To the best of available knowledge, this represents the first demonstration of a RI sensor based on a Hybrid External Cavity Laser (HECL) thus avoiding the necessity for an external light source. This innovative approach enables a multitude of benefits, such as compactness, portability, high sensitivity, a low detection limit (iLOD), label-free detection, and a simplified fabrication process. The Silicon Nitride Photonic Crystal Nanobeam Cavity with a parabolic-width stack and engineered side walls may serve as a highly responsive transducer in photothermal sensing applications for both gases and liquids. A comprehensive description of this design and conducted measurements can be found in [1].

3.2. Elliptical Nano pillars

Sensing applications that rely on refractive index (RI) measurements require innovative cavity designs with high-Q factor and encapsulation to mitigate the inherent inaccuracies in the fabrication process. The fine-tuning of existing RI sensors based on Photonic Crystal Nanobeam Cavities (PhCNC) makes them exceptionally sensitive to variations encountered during fabrication. Such imperfections can significantly compromise performance, especially

in designs that demand precise features across the entire parameter space [1,57,80,90]. To address this challenge, the implementation of elliptically shaped nanopillars to broaden the optimal operational range is proposed. Schematics of the PhCNC under study are illustrated in Figure 3.9. Three complementary cross-sections of the PhCNC immersed in various analyte refractive indices (n_a), ranging from 1 (typical for gases) to 1.45 (SiO_2), are illustrated.

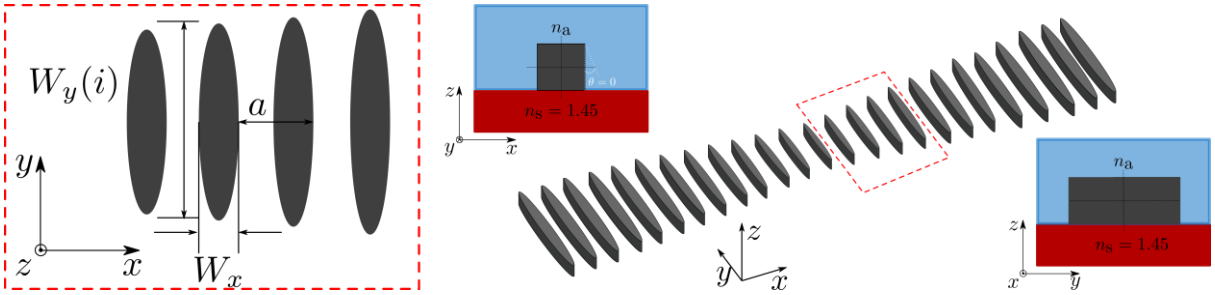

Figure 3.9 - Silicon Nitride Photonic Crystal Nanobeam Cavity with a parabolic-width stack of elliptical nanopillars. The vertical width of the stacks ($W_y\ (i)$) is modulated based on equation 3.1. The horizontal width W_x remains constant. The upper cladding, with refractive index n_a, is uniformly distributed in the surrounding volume. The structure is placed on a SiO_2 substrate with refractive index n_s.

In this structural arrangement, the major axis ($W_y(i)$) of the dielectric pillars is subject to quadratic variation, as defined by Equation 3.1. This variation extends from the central axis towards both extremes, where i ranges from 0 to $i_{\max}$. The minor axis of the pillars (W_x) remains constant. The refractive indices associated with the Silicon Nitride stack and the silica substrate are at 2 and 1.44, respectively.

The response of the Q-factor, as determined through 3D-FDTD simulations [82], was examined across a range of nanopillar widths W_x within two distinct shape configurations: rectangular and elliptical. The structural parameters were defined as follows: the lattice constant a was set to 496 nm, W_x was specified as $0.62a$, and W_y with a progression from $W_y(0) = 2.8a$ at the central axis to $W_y(92) = 4.0a$ on both sides.

Figure 3.10 (a) presents the comparison of calculated Q-factors exceeding 10^6 across a wide spectrum of elliptical nanopillar widths (W_x ranging from 228 to 308 nm in 20 nm increments), in contrast to rectangular counterparts with a specific optimal width (W_x=228nm). This demonstrates that elliptical nanopillars extend the Q-factor enhancement by up to one order of magnitude, transitioning from the localized optimal width of 288 nm to a broader range (>40nm).

The calculated field distribution (E_y) over a range of refractive indexes shows the energy is distributed in the cladding and confirms the interaction between the resonant mode and the upper cladding. Figure 3.10(b) presents the spatial distribution of the mode among the cavity when W_x=268nm, which corresponds to the maximum Q-factor in Figure 3.10(a). Further calculations quantify the sensitivity over hundreds of nm across the whole RI range, which combined with the higher Q-factors offer a significant design being highly resilient against fabrication tolerances.

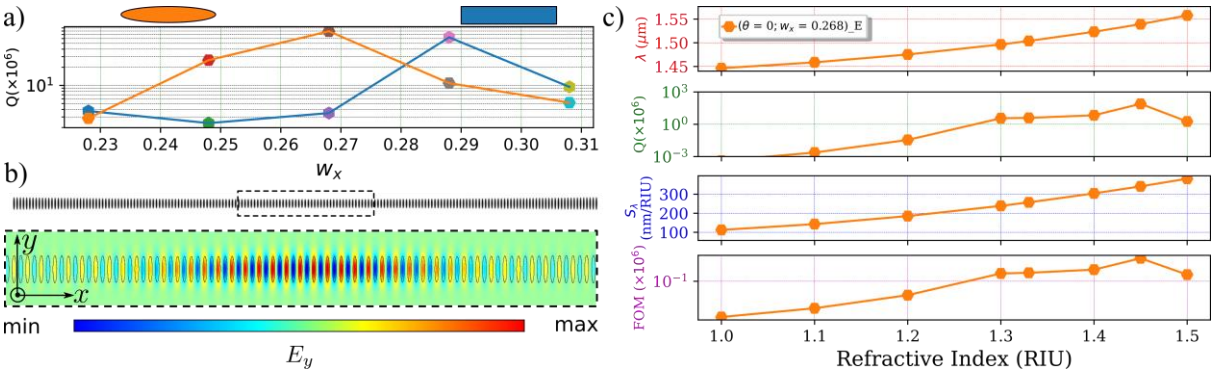

Figure 3.10 - (a) Calculated Q-factor for PhCNC using elliptical nanopillars (depicted in orange) and rectangular nanopillars (shown in blue) are presented across different minor axis widths (W_x), all cladded with a constant analyte refractive index of n_a=1.45. (b) Dielectric distribution of the proposed PhCNC, followed by the electric filed distribution (E_y) at a wavelength ~1531 nm (c) Fundamental mode's wavelength (λ), Q-factor (Q), Sensitivity (S_λ), and Figure of Merit (FOM) of the proposed PhCNC, spanning various upper cladding refractive indexes.

In Figure3.10(c) the calculated Q-factor shows the best suitability for aqueous analytes (n_a=1.31-1.33) with values exceeding 10^6. The computed Spectral Sensitivity (S) aligns with the experimental values reported for similar cavities, reaching values larger than 200 nm/RIU for liquids and over 100 nm/RIU for gases (n_a=1) [1]. The estimated Figure of Merit (SQ/λ_{res}) reaches as high as 10^5, influenced by the trade-off between S and Q.

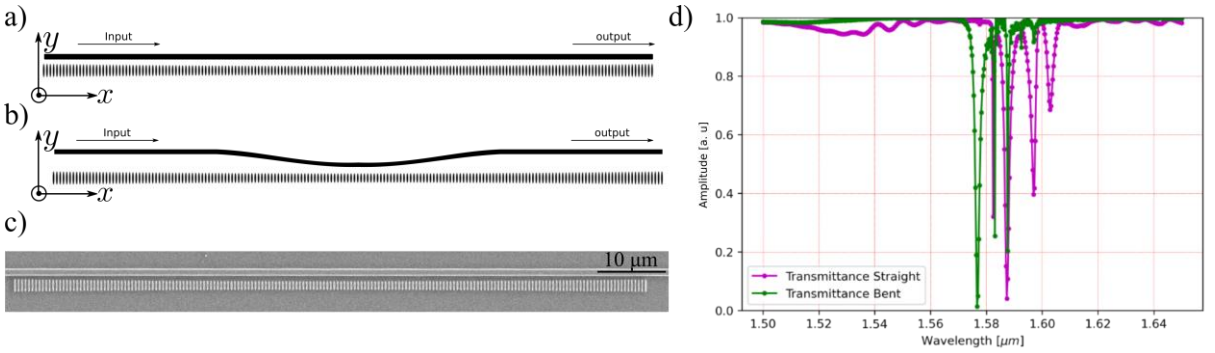

Figure 3.11 - (a) Dielectric distribution of the PhCNC for side-coupled to a straight waveguide. (b) dielectric distribution of the PhCNC when coupled to a S-bent waveguide. (c) SEM image of the fabricated device described in (a). (d) Calculated FDTD transmittance for the straight and bent waveguide depicted in (a) and (b). The Fabrication work was done in conjunction with Simone Iadanza and Artem Vorobev.

Extra losses can emerge within the coupler due to scattering losses, as well as unintended coupling into higher-order modes. When exploring multimode resonators, it is crucial to carefully consider the design of directional couplers. In addition to the necessity for minimal excess coupler loss (which contributes to parasitic losses), inadvertent coupling to higher-order modes can result in multiple sets of resonances characterized by distinct Free Spectral Ranges (FSRs), ultimately reducing the quality factor (Q) of the resonator. Therefore, the optimization of the coupling mechanism to control the spatial modes excited in the waveguide-PhCNC is investigated [87,88].

The first type of coupler under examination was the straight coupler, as presented in Figure 3.11 (a) and (c), where a straight bus waveguide was coupled to the PhCNC. Reducing the gap between the waveguide-cavity system resulted in an associated excess loss, leading to inefficiencies that constrained the quality factor [88]. Furthermore, these couplers exhibited significant coupling to higher-order modes, causing distortions in the resonator spectra. These observations were confirmed through FDTD calculations presented in Figure 3.11 (d).

In contrast, employing a weakly tapered layout makes it possible to tailor the directional coupler excitation to the PhCNC [88]. Thus, a weakly tapered gap between a S-Bent waveguide and the resonator, with parabolic width modulation, is achieved. A schematic of the S-Bend is presented in Figure 3.11 (b). This design will result in a more adiabatic transition region from the input bus waveguide (S-bent) to the coupling region when compared to straight couplers. As a result, this approach will reduce the excess loss of the coupler. FDTD calculations were conducted and are presented in Figure 3.11(d). The bent shape allows for more efficient excitation of the fundamental mode over the high-order modes.

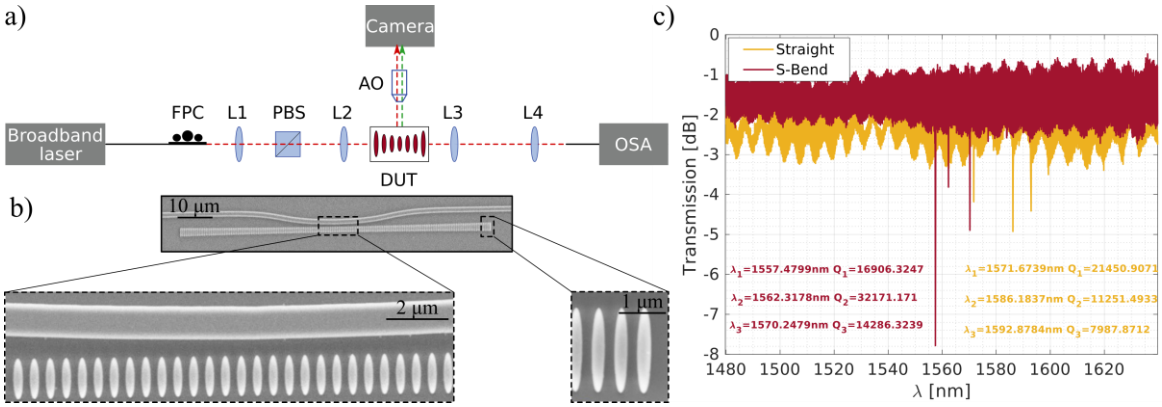

Figure 3.12 - Experimental setup for the characterization of the fabricated devices [1]. Lenses (L_1, L_2, L_3, L_4), Polarization Beam Splitter (PBS), Microscope Objective (AO), Fiber Polarization Control (FPC), PhCNC (DUT) (b) SEM image of a fabricated sample device with two insets detailing the coupling section and the elliptical shape achieved in fabrication (c) Transmittance of the PhCNC when a=516nm W_x=328nm is side-coupled to a straight or S-bend waveguide.

In contrast, Figure 3.12 (a) describes the experimental setup employed to characterize the fabricated straight coupler, as shown in Figure 3.11(c), and the bend coupler to the PhCNC presented in Figure 3.12(b). Details in the fabricated device in Figure 3.12(b) unambiguously illustrate the elliptical shape of the considered pillars. The measured transmittance spectrum of one of the proposed PhCNC structures side-coupled by a Straight and S-Bend waveguide with air cladding is presented in Figure 3.12(c). Three different resonant modes (1, 2, 3) are excited with an average FSR of 6.386 +/- 2.1892 [nm] between adjacent modes and Q-factor ranging from 10^4 to $3.2 \cdot 10^4$. These measurements are consistent with previous studies conducted on similar types of resonators [1].

In summary, a novel one-dimensional (1D) Photonic Crystal Nanocavity (PhCNC) design using elliptical nanopillars has been introduced. This design demonstrates high-Q performance, compact dimensions (approximately 100×10 µm^2), and resilience to fabrication errors within a margin of +/-40 nm. These attributes position it as a promising solution for refractive index sensing and as a transducer for photothermal spectroscopy, among other photonics applications in photonics research.

3.3. Slotted Nanobeam

In conventional photonic crystal nanobeam cavities, as described in the previous sections, achieving a high Q-factor implies strong confinement of the optical mode within the high-index material (e.g. Si, Si_3N_4). Almeida *et al.* [91] introduced the concept of "slot-waveguide" structures. These structures leverage the discontinuity of the optical field at a dielectric interface to support a propagation mode within a narrow gap of low refractive index. This innovative approach has attracted considerable interest within the sensing community and

has found implementations in the context of two-dimensional (2D) PhC cavities, Micro Ring Resonators, and Fabry Perot structures [70,71,92].

Various implementations of slotted Photonic Crystal Nanobeam Cavities (PhCNCs) have been documented [93–95]. For instance, slotted configurations with sidewall gratings and elliptical holes have been explored for applications in refractive index sensing and optical trapping [56,96]. Prior work has also investigated slotted geometries with modulated stack nanobeams in silicon [55,95]. In contrast, effective control of Q-factors has been achieved through the engineering of hole cross-sections within the taper and mirror regions of the cavity [94].

This section presents the design of a high Q-factor Slotted Photonic Crystal Nanobeam Cavity with a parabolic-width stack and engineered sidewalls.

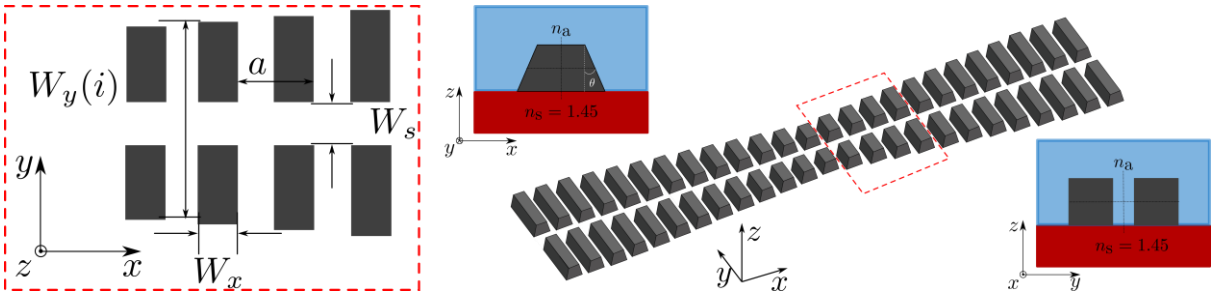

Figure 3.13 - Silicon Slotted Photonic Crystal Nanobeam Cavity with parabolic-width stack and engineered sidewalls. The vertical width of the stacks ($W_y(i)$) is modulated as per equation 3.1. The horizontal width W_x remains constant. The angle, θ, defines the lateral tilt of the side walls stacks. The upper cladding, with refractive index n_a, is uniformly distributed in the surrounding volume, including the slot region, extended along the entire device with a size of W_s. The structure placed on a SiO_2 substrate with refractive index n_s.

In Figure 3.13, a schematic representation of the slotted PhC stack mode-gap cavity, as considered in this research, is presented. In this structure, the vertical widths ($W_y(i)$) of the dielectric blocks are modulated by a quadratic law (equation 3.1), progressing from the center to both sides, where i ranges from 0 to $i_{\max}$ .The refractive indices of the silicon stack and the silica substrate are 3.46 and 1.44, respectively.

A numerical investigation of the impact of oblique sidewalls and the number of segments on the Q-factor of the proposed Silicon PhCNC is conducted. The geometric parameters of the structure were specified as follows: the lattice constant a was set to 410 nm, W_s (the width of the central slot) was 200 nm, W_x was defined as $0.4a$, and W_y from $W_y(0)$ =$3a$ in the center to $W_y(20)$ $6a$ on both sides.

Figure 3.14(a) illustrates the enhancement of the Q-factor in comparison to the vertical sidewalls (depicted in blue) for various sample refractive indexes. The most notable increase is observed at $n_a = 1$. On the other hand, for water-like samples with n_a=1.31-1.33 The tendency, is the same, however with a reduced boost [97]. In this context, Figure 3.14(b) demonstrates the effect of the number of segments (NG) on the Q-factor when n_a is fixed at 1, representing gas-like samples. The influence of the number of segments (NG) on the Q-factor, with the refractive index of the superstrate (n_a) held constant at 1, confirms that a significant enhancement of approximately one order of magnitude through the synergy of oblique angles and segment count.

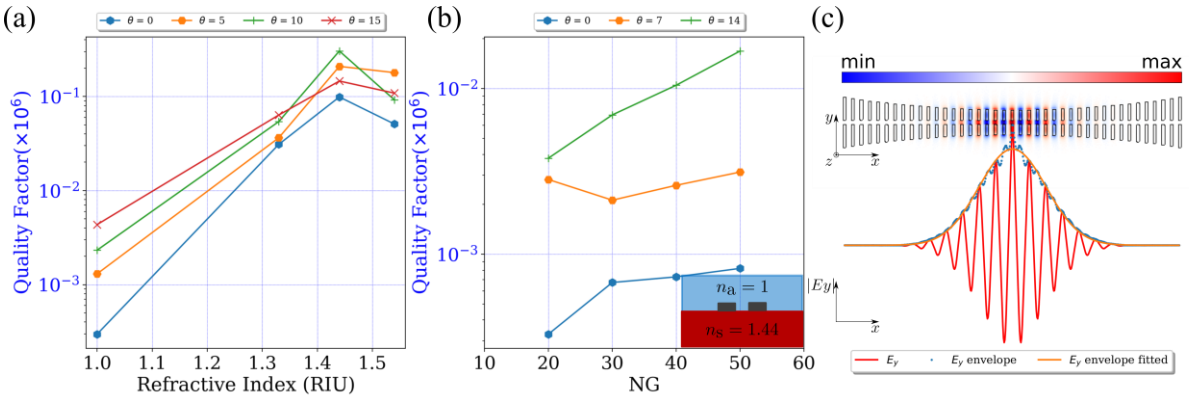

Figure 3.14 - (a) The Q-factor for various analyte refractive indices (n_a) while varying the sidewall angle (θ). (b) Number of Gaussian mirror segments (NG) and their effect on the Q-factor for n_a=1. (c) Dielectric distribution of the proposed cavity structure, with the electric field (E_y) at a wavelength of 1547.8 nm superimposed. At the bottom, a profile along the x-axis (slot region) with an overlaid Gaussian envelope fitting.

The field distributions were investigated and computed using the 3D Finite-Difference Time-Domain (FDTD) method [82] to monitor the fundamental mode supported by the structure described in Figure 3.13. In the illustration of Figure 3.14(c), the electric field amplitude of the fundamental mode (E_y component) at a wavelength of 1547.8 nm is presented. The field distribution profile demonstrates the matching of the intensity profile envelope with a gaussian function. Consequently, this observation highlights a crucial design characteristic considered for mitigating radiation loss [48].

This novel design demonstrates a significant enhancement of the Q-factor by two orders of magnitude compared to the vertical counterpart. This improvement can be attributed to variations in sidewall angles and the number of segments within the structure. Consequently, the combination of oblique angles and the number of segments allows for a two-order-of-magnitude improvement of the Q-factor. Future advancements in this field may provide opportunities for monitoring changes in sensing applications, especially for liquids with refractive indices near 1.33 (as shown in Figure 3.14(a), such as water).

Further optimization will involve a rigorous study of the sensitivity, in the reported cases where the Q-factor was high (>10^4). Similar devices report that the sensitivity tends to increase in correlation with the slot width, while the Q-factor experiences a significant exponential decrease as the slot width expands. Fabricated devices report experimental sensitivities ~400nm/RIU [95].

3.4. Summary & Perspective

Different approaches for achieving compact (~100 × 10 μm^2), easily fabricated (single etching) high Q-factor, and highly sensitive photonic cavities with exceptional sensitivity, under different upper cladding configurations were further discussed. The numerical simulations and the obtained experimental results all support the suitability of the proposed devices as refractive index transducers.

The systematic optimization of the geometrical parameters of the PhCNC with angled side walls was found to be very attractive in different sensing scenarios, despite the lower contrast associated with on-suspended configurations. The potential for customizing the optical characteristics of these devices when dealing with asymmetric cladding configurations, accomplished through the control of the etching angle, was shown. This parameter acts as an

additional and highly desirable property for adjusting the performance of microcavity-based refractive index sensors.

The elliptical nanopillar-based cavity offers a promising solution to address inherent inaccuracies associated with fabricated devices while maintaining a high Q-factor. On the other hand, the slotted configuration with angled sidewalls introduces an extra mechanism to compensate for the drop in Q-factor characteristic of highly sensitive photonic cavities.

The coupling optimization by the S-bend waveguide is fully transferable to all the discussed designs. Therefore, the complementarity of the designs studied opens the door for further optimization, in the sense of taking the best capabilities observed in each design.

The potential of PhCNCs as refractive index transducers has led to innovative research to enhance their capabilities. For instance, recent work has demonstrated the simultaneous sensing of refractive index and temperature by optimizing elliptical and slotted holes using artificial intelligence techniques [98]. Furthermore, PhCNCs employing elliptical holes to optimize a dielectric mode photonic crystal have been investigated [99]. These studies have illustrated their capacity to achieve high anti-interference performance, rendering them valuable for multifunctional sensing [100].

Another intriguing avenue of exploration involves utilizing PhCNCs with elliptical holes capable of supporting Fano resonances, which provide a unique approach to achieve multi-parameter sensing [101,102]. High-Q non-suspended nanobeam cavities on a 300-nm-thick Si_3N_4 platform featuring 1D slow-light photonic crystal waveguides and Bragg mirrors exhibit a cubic relationship between cavity length and Q-factor. This relationship enables the possibility of having significant Q-factors with shorter cavities [78].

Cumulatively, the results detailed in this thesis, combined with the collaborative efforts of the research community, represent a substantial advancement in the utilization of non-suspended PhCNCs for optical sensing applications. This progress opens doors to a wide range of possibilities, including simultaneous sensing of refractive index and temperature, as well as multi-parameter sensing capabilities.

Chapter 4 - PHOTONIC FANO CAVITIES BASED MICRO RING RESONATORS

Micro Ring Resonators (MRR) have shown a wide variety of application prospects, including optical communication, filtering, sensing, non-reciprocal transmission, optical switching, nonlinear optics, and more recently also in quantum optics [62,103–107]. The ability of MRRs to operate as a stand-alone device is dependent on their external connectivity. The most common coupling mechanism is codirectional evanescent coupling between the ring and an adjacent bus waveguide [64]. The transmission spectrum of a bus waveguide-MRR configuration usually exhibits dips around the MRR's resonances. The resonances' shape and location are quite susceptible to external factors, which can be favorable (as a tuning tool or for sensing) or detrimental (in terms of spectral filter stability). The advantages of MRRs are their compact footprint, low power consumption, convenience for integration, and stability making them a fruitful platform for the realization of optical sensors [13].

Devices characterized by a symmetric Lorentzian resonance lineshape, which is typically observed in the transmission spectrum of the MRRs, are known for modest resonant slopes, and low extinction ratios. An asymmetric resonance lineshape, also referred to as a Fano resonance, arises from superimposing the narrowband Lorentzian response on a broadband background field [108]. Fano resonances exhibit an amplified ON/OFF amplitude transition compared to classical Lorentzian-type resonators with higher quality factors, and steeper slope rates [109]. Alternatively, in the waveguide-MRR configuration, the coupling and decay rates can be controlled by inserting a small air-based Partially Transmitting Element (PTE) [110,111].

In this chapter, several designs of Fano-resonators based on MRRs are discussed. Here, the Fano-like shapes result from the interference between MRR's resonance modes, and the leaky quasi-transverse modes partially guided through a Photonic Crystal Nanobeam.

4.1. Fano resonance generation in a Photonic Crystal Nanobeam-assisted MRR

4.1.1. Principle

The distinctive Fano resonance, known for its characteristic asymmetry, emerges from the interference between a discrete state (narrow resonance) and a continuum (broad resonance) [108,112]. The bus waveguide's modes leakily transmitted through the periodic PhCN region as the continuum [28,113], instead of the usual broad resonance, and the cavity modes supported by a MRR as discrete states, are used. Notably, the transmittance and resonant modes in this configuration are generated in distinct physical channels. As depicted in Figure 4.1, the Fano resonator is constructed using a single-mode strip waveguide (position *i*), which

aligns with a Photonic Crystal Nanobeam, and subsequently establishes side-coupling with an MRR (position *ii*).

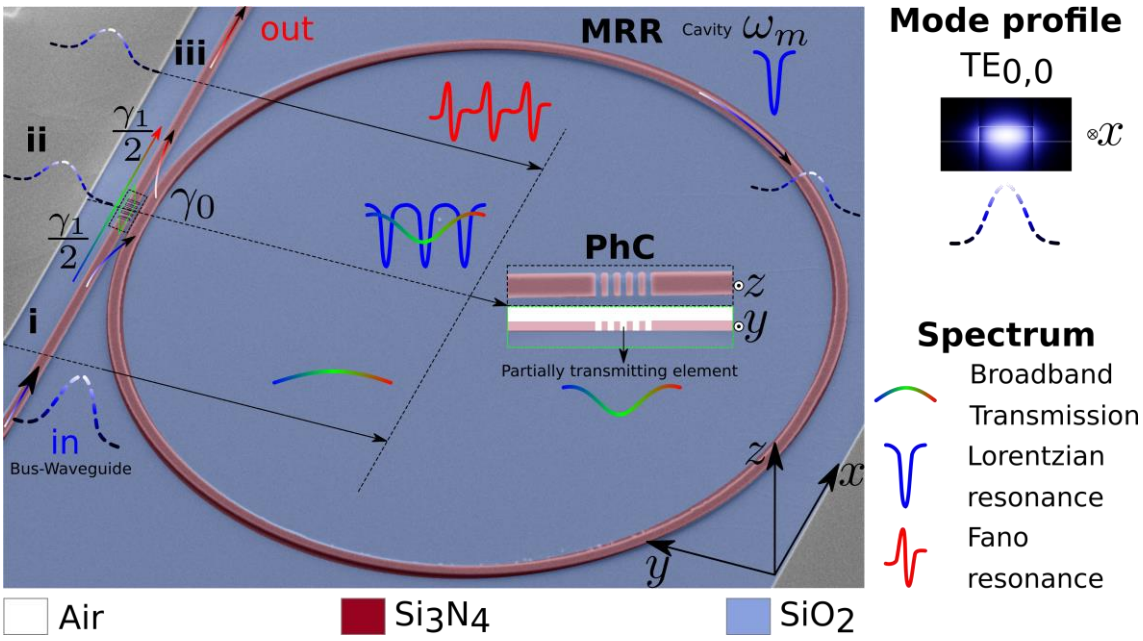

Figure 4.1 - Conceptual layout of the envisaged Fano cavity, which features a side-coupled Photonic Crystal Nanobeam to a Micro Ring Resonator. In the upper right section, the blue gradient dashed curve is employed to depict the spatial mode profile, specifically representing the TE-like propagating mode. Furthermore, the rainbow, red, and blue curves are indicative of the spectral line shapes corresponding to the propagating modes. This configuration allows for a clear visualization of the essential components and the mode profiles involved in the system.

The waveguide cross-section exhibits a symmetric spatial field distribution for the TE-like mode (electric field in the *x*–*y* plane) and it is represented by a blue gradient dashed line in the top left inset. A broad resonance corresponds to the spectral content of the TE-like propagation mode (Figure 4.1 position *i*) that interacts with the periodic waveguide region (PhCN). The spectral domain interference between the resonances supported by the MRR and the propagating light through the PhCN region is drawn in Figure 4.1 at position *ii*. Therefore, Fano resonances are identified at position *iii* in the bus waveguide, due to the mixing of the modes generated at position *ii*. The Fano cavity's principle of operation is illustrated by three planes denoted by black dashed lines (*i, ii, iii*) at various locations in Figure 4.1: position *i* at the input bus-waveguide, position *ii* at the coupling region PhCN-MRR, and position *iii* at the bus-waveguide's output.

When one or more cavities are coupled to a waveguide that supports a continuum of modes, Fano resonances for in-plane structures can be obtained [114,115]. In this case, the PhCN created by etching periodic air-based PTE in a Silicon Nitride strip waveguide drives the continuum. Figure 4.1 shows two cross-sections of the periodic waveguide at location *ii*. In such a system, the propagating mode of the waveguide must gently interact with the PTE for tuning the transmission spectrum response[36], and it can replicate the smooth and flat-like transition amplitude (further explanation of the design is given later in this section). The spectral transmission feature mentioned is shown by a rainbow gradient solid curve in Figure 4.1. On the other hand, MRRs support several resonances with prominent spectral dips, whose spacing is dependent upon the resonator length (see blue solid curve at location *ii* in Figure 4.1). Thus, the spectral response of the mutually connected PhCN-MRR displaying various Fano-like forms is sketched by the red solid curve at Figure 4.1 position *iii*.

The classical asymmetric Fano like-shapes can be characterized by the following equation [116–118]:

$$F(\omega) = A_0 + F_0 \frac{[q + 2(\omega - \omega_0)/\Gamma]^2}{1 + [2(\omega - \omega_0)/\Gamma]^2}, \tag{4.1}$$

where ω corresponds to the incident light frequency, ω_0 is the frequency of the cavity mode and Γ quantifies the resonant linewidth. F_0 and A_0 are associated with a scaling factor, and a constant shift, respectively. q is the unitless Fano asymmetry parameter. The calculated Lorentzian and Fano resonance centers at ω_0 are presented in Figure 4.2(a).

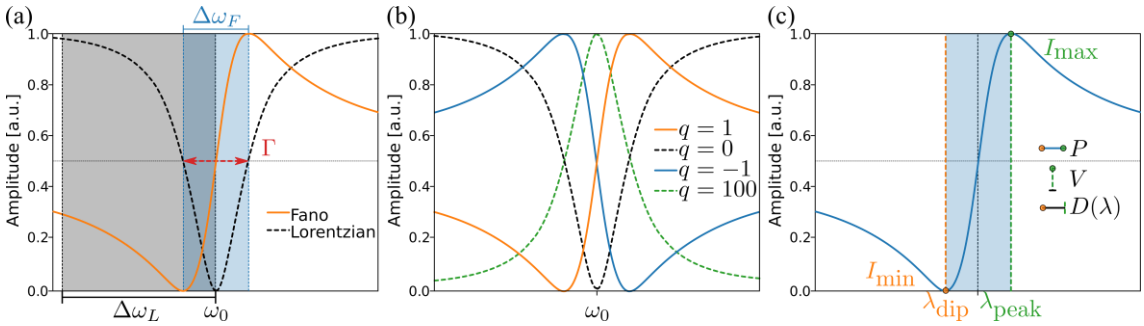

Figure 4.2 - Normalized transmittance amplitude of (a) Lorentz (dashed black) and Fano (filled blue) line shapes resonances centered at ω_0 , with linewidth Γ. The signal suppression level performance at the wavelength detuning between the maximum reflection and maximum transmission for both Fano and Lorentz are labeled as $\Delta\omega_F$ (light blue) and $\Delta\omega_L$ (light black) respectively. (b) Fano asymmetry parameter $-1 < q < 100$ associated with Lorentzian, Fano, and electromagnetically induced transparency-like resonances. (c) Performance metrics of an asymmetric line shape: Slope evaluation parameter (P), Visibility (V), and corresponding wavelength difference (D). The slope of the tangent line at the inflection point is defined as $\max\left(\frac{dI}{d\lambda}\right)$.

The frequency detuning $\Delta\omega$ needed to accomplish the ON/OFF amplitude transition in the Lorentzian and Fano profiles, respectively, is depicted by the overlaid curves drawn in Figure 4.2(a). Due to the sharp and asymmetric shape of Fano, a little shift (in units of Γ) will cause the Fano's amplitude change to be more significant than the Lorentzian one ($\Delta\omega_F < \Delta\omega_L$). The linewidth of the resonant cavity is equal to the minimum $\Delta\omega$ that permits the total signal suppression level of an asymmetric Fano resonance [114]. Based on the resonance tracking problem, this suggests that Fano resonances have a major advantage in developing more robust and efficient photonic integrated refractive index sensors, as compared to MRR alone [63].

A range of Fano resonance line shapes with different Fano asymmetry parameter (q) values is shown in Figure 4.2(b). When destructive interference between the discrete mode and the continuum occurs, the black dashed line (q=0) represents a symmetric Fano-like dip at a resonant frequency ω_0. A blue-parity Fano (transmission dip blue-shifted) is drawn with a filled blue line (q=1). Subsequently, a red-parity Fano (transmission dip red-shifted) is sketched with a filled orange curve (q=-1) [119]. On the other hand, the green dashed line (q=100) represents a Lorentzian shape without any discernible interference features. A precise design of the Fano asymmetry parameter q allows for the creation of any slope shape between the Lorentzian peak and the quasi-symmetric Fano dip[111,120].

A blue-parity Fano profile with multiple key characteristics is shown in Figure 4.2(c). Further analysis will be done based on sketched features. [119]. The fringe visibility in terms of the resonance's peak and dip intensity [121,122] is defined by V as follows:

$$V = \frac{I_{max} - I_{min}}{I_{max} + I_{min}}, \tag{4.2}$$

where I_{max} and I_{min} are the normalized minimum and maximum transmission, correspondingly. The wavelength difference between peak and dip is defined as

$$D(\lambda) = \left|\lambda_{dip} - \lambda_{peak}\right|, \tag{4.3}$$

where, $\lambda_{dip}$and λ_{peak} are the wavelengths at the dip and peak intensity, respectively. Here, the slope of the Fano resonance is defined as

$$P = \frac{V}{D(\lambda)}, \tag{4.4}$$

In [122], the $10\log(P)$ value is suggested in order to examine the Fano resonance's complex refractive index sensing characteristics. On the other hand, the ratio $\omega_0/\Delta\omega$, where $\Delta\omega$ is the full-width at half-maximum (FWHM), is usually defined as the quality factor on modern resonant structures (Lorentzian) [123]. In this study, the fitted parameters on equation (4.1) are used to determine the loaded Quality factor using the ratio ω_0/Γ.

The physical process underlying the suggested PhCN-MRR structures is the interference between two channels, as shown schematically in Figure 4.1 (note the color gradient-filled arrows in Figure 4.1). The first path represents the light traveling through the PhCN region, which drives the continuum. The second path consists of the incoming-outcoming light through the MRR-PhCN. The generation of Fano resonances in complex waveguide-resonator systems has been explained by several theoretical models, including the Fano-Anderson model [124–126], temporal coupled mode theory (TCMT) [127–129], and transfer matrix method [111,130]. Here, the TCMT formalism provides a qualitative explanation for the transmission behavior of the PhCN-MRR structure [114,131,118]. Therefore, one way to express the structure's transmission is:

$$T(\omega) = \left|-|t|^2 \pm i|t|\sqrt{1-|t|^2} + \frac{\gamma_1}{i(\omega_0 - \omega) + \gamma_C}\right|^2 \tag{4.5}$$

where t denotes the PTE's transmission coefficient [128]. The frequencies of the cavity resonance (ω_{m-th} at MRR) and the input signal are denoted by ω_0 and ω, respectively. With decay rates $\gamma_1/2$, the field in the MRR couples to the input and output ports (see Figure 4.1). As a result, $\gamma_C = \gamma_1 + \gamma_0$ defines the total decay γ_C in terms of the intrinsic loss rate of the MRR, γ_0. The cavity intrinsic and total quality factors, Q_0 and Q_C, can be linked to γ_0 and γ_C in this case as $\gamma_0 = \omega_0/2Q_0$ and $\gamma_C = \omega_0/2Q_C$. Furthermore, a cavity mode that is even (odd) regarding the mirror-reflection symmetry plane (transversal black dashed line in Figure 4.1) is indicated by a positive (negative) sign. Given a fixed intrinsic loss rate γ_0, it can be deduced that the transmission line shape, as expressed in equation (4.5), is mostly determined by the coefficients t and γ_1[118].

A recent example uses the essence of the model described by Equation 4.5 with a structure like the ones described in Chapter 3. The main difference relies upon the use of the air-band mode[129]. When considering the specific case of the MRR as a resonant cavity driving the discrete state required for the Fano resonance, is natural to think back reflections are exciting counter-propagating modes. These counterpropagating waves are integrated into a transfer matrix model that refines currently accepted models in the field of Fano resonances based on MRR [111].

4.1.2. Design and Simulations

The MRR (discrete state) and PhCN (continuum) are the two primary parts of the Fano cavity that were identified in the preceding section. Next, two types of Silicon Nitride Fano resonators—air-based circular hole and rectangular slot — on the generation of Fano shapes, are compared. As a result, a set of numerical calculations that were used to develop the fundamental components of the suggested device is provided. First, the uncoupled MRR and PhCNs followed by the side-coupled devices are presented.

4.1.2.1. Silicon Nitride Micro Ring Resonator

In general, the light in a MRR circulates in a bent waveguide usually supporting either TE-like or TM-like propagating modes. The guided modes mentioned, satisfy the resonance condition when the optical path length of the resonator is an integer multiple of the wavelengths [64].

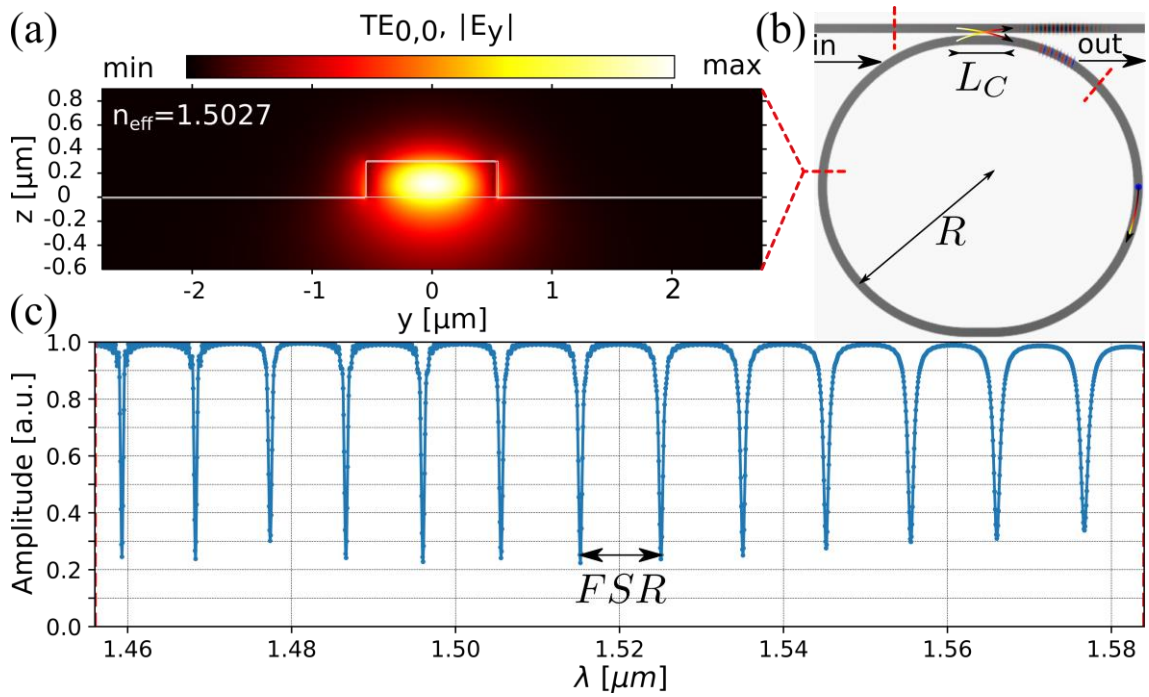

Figure 4.3 - The transversal electric field, TE-like, of the MRR strip waveguide, looped back on itself. (b) Dielectric distribution of a coupled MRR superimposed with the calculated E_y field of a broadband pulse time evolving in the structure. (c) Calculated spectrum of the racetrack MRR.

Figure 4.3. (a) present the calculated field distribution and n_{eff} of a TE-like propagating mode in a strip waveguide. In this work the bus waveguide and the MRR have the same cross section as shown in Figure 4.3(b) (red dashed lines). The 1.1µm width and 0.3µm thick strip of Si_3N_4 ($n_{Si_3N_4}$=2) is placed on top of a BOx (n_{SiO_2}=1.45) slab surrounded by air. The evanesced wave extends from the sidewalls interface and its power exponentially decreases with increased distance from the surface as shown in Figure 4.3(a). For TE-n_{eff}^{air}=1.5027, Figure 4.3 (c) shows the resonances (dips) obtained by 3D-FDTD, which differ in less than 1nm from the ones calculated using equation (2.6). The cavity mode is excited by codirectional evanescent coupling between closely spaced optical waveguides (color gradient arrows Figure 4.3 (b)). Figure 4.3 (b) details that the MRR round trip is defined in terms of of L_C as $L = 2\pi R + 2L_C$. L_C is the coupling distance between the MRR-waveguide. The straight section L_C acts as a directional coupler element to conveniently control the coupling strength, while the radius R of the circular section can be adjusted to control the cavity length to obtain the desired resonance wavelength and the resulting spacing between adjacent resonances known as the

Free Spectral Range (FSR). Here the coupling section and radius are fixed to 2.75µm and 16.27µm, respectively.

Well-established MRR models present different relations to enhance the features (e.g., Q-factor, FSR) of the MRR that can be rigorously analyzed through the equations described in [64]. In this sense, further analysis of the MRR waveguide is carried out to analyze the mode symmetries supported in two different telecom wavelength ranges: 1.330µm (O-band) and 1.550(C-band).

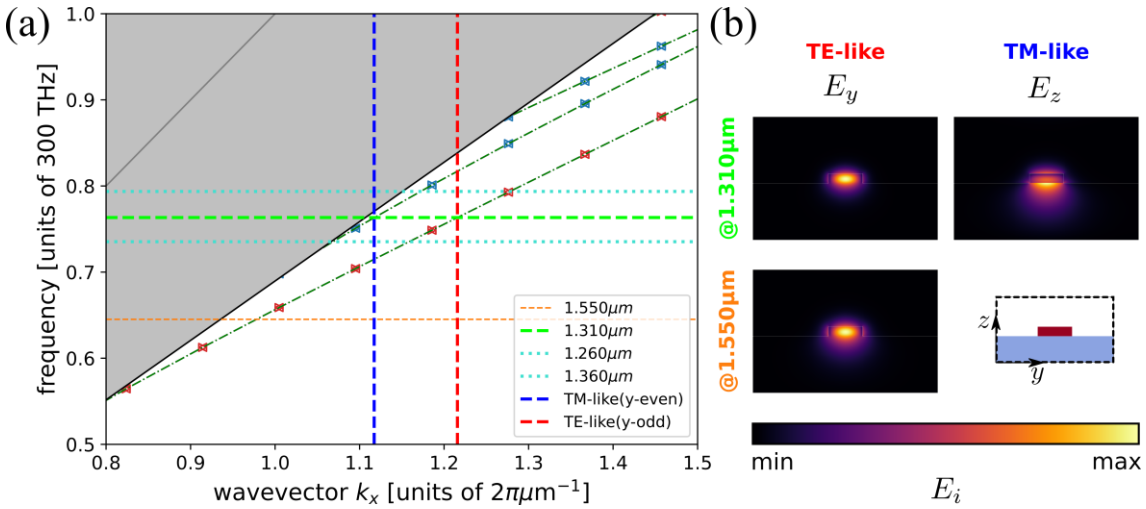

Figure 4.4 - Dispersion relation of the TE-like (y-odd mode) and TM-like (y-even) guided modes in the Si_3N_4 strip waveguide. (b) Calculated electric field distribution of the guided modes for TE and TM-like at 1.310µm and TE-like at 1.550 µm

The Si_3N_4 strip waveguide dispersion relation is shown in Figure 4.4(a). The guided bands are shown as green point-dashed lines that intersect red and blue triangle markers. Note that the strip waveguide is air-cladded and on a SiO_2 substrate. The TE-like symmetry mode is represented by the red triangular marker, and the TM-like symmetry mode is represented by the blue triangle marker. The SiO_2 light line is shown in black, while the air light line is represented by a dark gray line. The bands are naturally lossless and fully guided below the SiO_2 light line. The target wavelengths are shown by dashed horizontal lines in orange and lime, which are 1.550 µm (C-band) and 1.310 µm (O-band), respectively. The upper (1.260 µm) and lower (1.360 µm) limits of the Telecom O-band are indicated with cyan dotted lines. There is a single mode at 1.55 µm, as indicated by the orange dashed horizontal line that only crosses the lowest guided band once. Conversely, the horizontal lime dashed-line crosses over two guided bands. Red and blue dashed vertical lines, representing the TE-like and TM-like modes symmetry, are used to identify the two crossing places. As a result, the strip waveguide can guide both the TM-like mode with a prevailing E_z field and the TE-like mode with a dominant E_y field. Figure 4.4(b) shows the computed electric field distributions for the guided modes in the waveguide. It should be noted that the O-band's lower limit (1360 µm) roughly falls inside the single-mode operation cut-off. Then, multimode operation will be supported by higher frequencies.

4.1.2.2. Air-based circular holes Photonic Crystal Nanobeam-assisted Micro Ring Resonator

Initially, the work is restricted to circular holes, later rectangular slots will be considered as well. A PBG is used to define the 1D periodic structure as the one that constitutes the PhCN region of the waveguide [36,37]. It is well known that, independently of the refractive index contrast, all 1D periodic structures exhibit a PBG [36]. When the upper cladding and substrate

are similar (e.g., SiO_2, air), a clear PBG is observed. However, the symmetry break induced by the SiO_2 layer, suggests that some even/odd modes mixing could occur and the PhCN will hold partially guided modes in the lossy regime. This statement can be analyzed by means of the band structure of one unit cell of the PhCN region, presented in Figure 4.5(a).

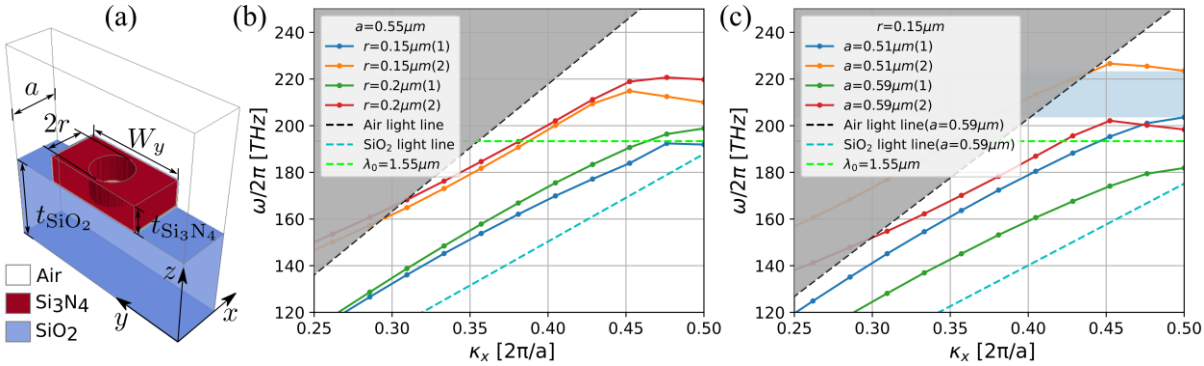

Figure 4.5 - (a) air-based circular hole-based PhCN unit cell. (b) Band diagram of the TE-like (y-odd mode) modes, with the lowest two bands (1, 2) shown for waveguides with large (r=0.2µm) and small (r=0.15µm) hole radius considering a fixed periodicity a=0.55µm. Frequencies corresponding to extended states propagating on air above the light line are shaded in gray. The blue-shaded region corresponds to the photonic band gap constituted between the dielectric-like (blue-dotted line) and air-like (orange-dotted line) bands, respectively. (c) Band diagram of the TE-like modes bands (1, 2) shown for waveguides with large (a=0.510µm) and small (a=0.590µm) hole periodicities considering a fixed radius r=0.15µm

The first design constraint is for the waveguide width, equivalent to 1.1µm. The projected band structure $\omega_n\ (k)$, considering the propagation along x direction (k_x) is shown in Figure 4.5(b). The parameter n refers to the band number. The lowest two bands are peaked as (1) and (2), respectively. The calculated bands are above the SiO_2 light line in a lossy regime. Figure 4.5(b) presents the calculated band diagram for a unit cell with periodicity a = 0.55 µm and radius r = [0.150; 0.200] µm. The blue-shaded region in Figure 4.5(c) represents the stop band created between the two lowest even quasi-guided modes when a = 0.510 µm and radius r = 0.150 µm [36,132]. Furthermore, Figure 4.5(c) shows the calculated band diagram for a fixed radius r = 0.150µm and several periodicities a= [0.510;0.590] µm. The quasi-guided modes (1) and (2), can be tuned by means of the a/r ratio to match the range of frequencies where the continuum is required to be for the Fano interference phenomena. Here telecom C-band is center at 1.55µm (light green dashed line, Figure 4.5(b)), or the O-band centered at 1.310µm. Interference between the MRR's resonances and either one of two edges of the stop band of the PhCN will lead to the targeted shape. The leaking mechanism [132] can be further suppressed by the reduction of the refractive index contrast with the upper cladding. Therefore, cladding the device with a common solvent (e.g. deionized water, ethanol) will bring the PhCN from a leaky to a guiding regime [97] (refractive index sensing in aqueous solutions). In periodic structures with a PBG constituted by fully guided modes, the high-frequency band edge is mostly localized in the low-index region, while the low-frequency band edge is mainly distributed in the dielectric. When there is a match between the electric field of the MRR's resonant modes and the PhCN's band edges, the coupling rate (large γ_1 equation 4.5) between the MRR and PhCN can be enhanced [118].

Complementary, 3D FDTD simulations were conducted to corroborate the findings because a dispersion relation calculation implies an infinite extent of the device (x-axis), and the intended PhCN has a finite length (see Figure 4.6). Perfectly matched layer boundary conditions were considered [82].

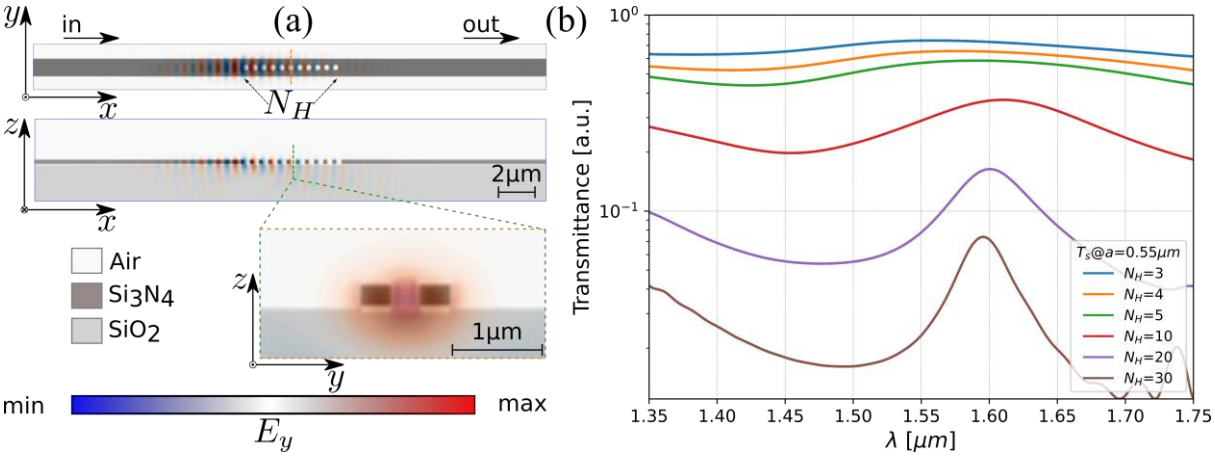

Figure 4.6 - (a) Dielectric distribution of the uncoupled PhCN superimposed with the calculated E_y distribution of a broadband pulse time evolving in the structure. Complementary cross-sections are presented. (b) 3D-FDTD calculated transmission spectra for different number N_H of air-based circular holes with fixed a=0.550μm, r=0.150μm.

The incident light E_y is calculated by time evolving a broadband Gaussian pulse along the PhCN for a fixed filling factor (r/a) as a function of N_H. N_H is the number of holes added to the bus waveguide as shown in Figure 4.6(a). The FDTD shows the portion of the propagating mode being pulled down to the substrate and scattered to the air, as shown in Figure 4.6(a). Supplementary, the normalized transmission spectra in Figure 4.6(b) state the dependence of the transmittance of the pure PhNC with respect to N_H. A higher number of defects will imply a reduction in the transmission amplitude of the frequencies surrounding the quasi-guided bands. Unambiguously a stop band with an edge around 1.580μm is observed. The transmission coefficient (t equation 4.5) of the quasi-guided modes through the PhCN is a defining parameter for the required Fano shape[118]. Therefore, independent control of the continuum by tunning N_H, is demonstrated based on the waveguide modes leakily transmitted through the periodic PhCN region.

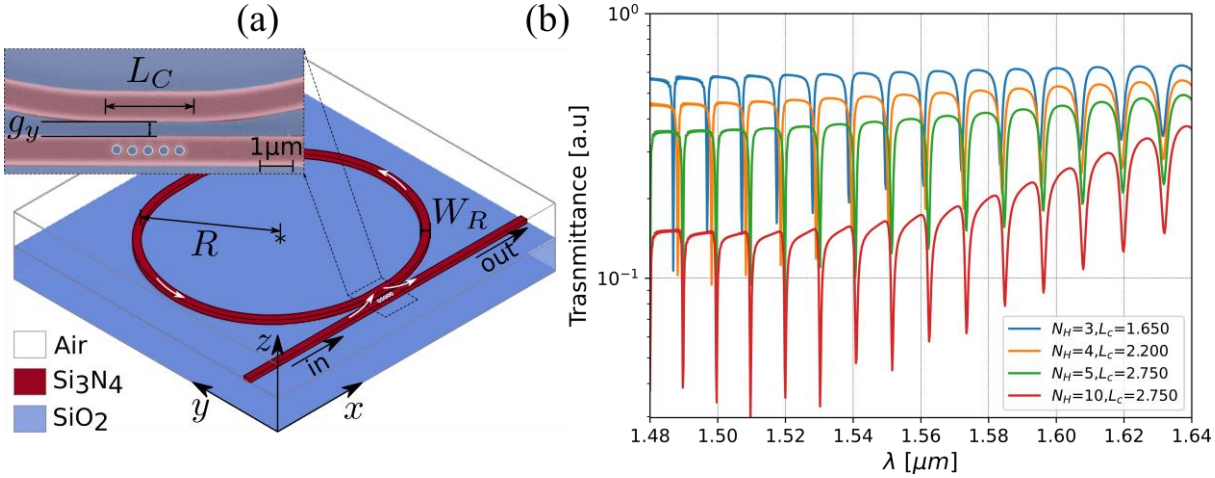

Figure 4.7 - (a) Schematic of the PhCN-MRR air-based circular holes considered with fixed R with different ranges of N_H=5 and L_C= N_H a. Upper-left inset shows the colored SEM image of one fabricated device. (b) 3D-FDTD calculated transmission spectra of similar devices in (a) for fixed coupling gap g_y=0.250μm and N_H=[3,4,5,10].

Figure 4.7(a) depicts the first type of Fano resonator based on the air-based circular holes PhCN-MRR structure taken into consideration in this work. Two semi-circular sections of radius R, width W_R, and a coupling section L_C form the racetrack MRR. The number of lattice periods N_H on the PhC will be matched by the coupling section length L_C. The coupling length (L_C) over which two closely spaced waveguides are coupled together, and their gap separation

(g_y) determine the coupling strength between them. The position of the Fano resonance is mainly dependent on the MRR resonance mode. Therefore, changes in the roundtrip path of the racetrack ring, $L(L_c)$, will produce the red shifting observed in Figure 4.7(b). On the other hand, g_y also affects the Fano resonance's asymmetry. The computed 3D-FDTD spectra are calculated in the region where the stop band edge, as shown in Figure 4.6(b), exists. The baseline of the spectra presented in Figure 4.7(b) is mostly determined by the transmittance envelope of the PhCN region (See, Figure 4.6(b)), while the strength of the asymmetry is led by g_y and N_H.

4.1.2.3. Air-based rectangular slots Photonic Crystal Nanobeam-assisted Micro Ring Resonator

The second design explores a periodic array of air-based rectangular slots with periodicity along the axis of propagation. Figure 4.8 (a) presents the unit cell of the PhCN region. In general, the light propagating through periodic slab waveguides (e.g. subwavelength) can be analyzed by the dispersion relation [75,89,90]. The band diagram derived for a unit cell with a width W_s= 2(0,100;0,1375) µm and periodicity a=0.55µm is shown in Figure 4.8(b). The width of the air-based rectangular slots was considered as W_s. The computed band diagram with a fixed W_s= 2(0,200) µm and a periodicity a= [0.510;0.590] µm is displayed in Figure 4.8(c). The leaky guided modes will move toward higher frequencies (shorter wavelengths) with an increase in breadth. Under the same principle described in the previous section, the waveguide modes partially guided through the PhCN will lead the continuum.

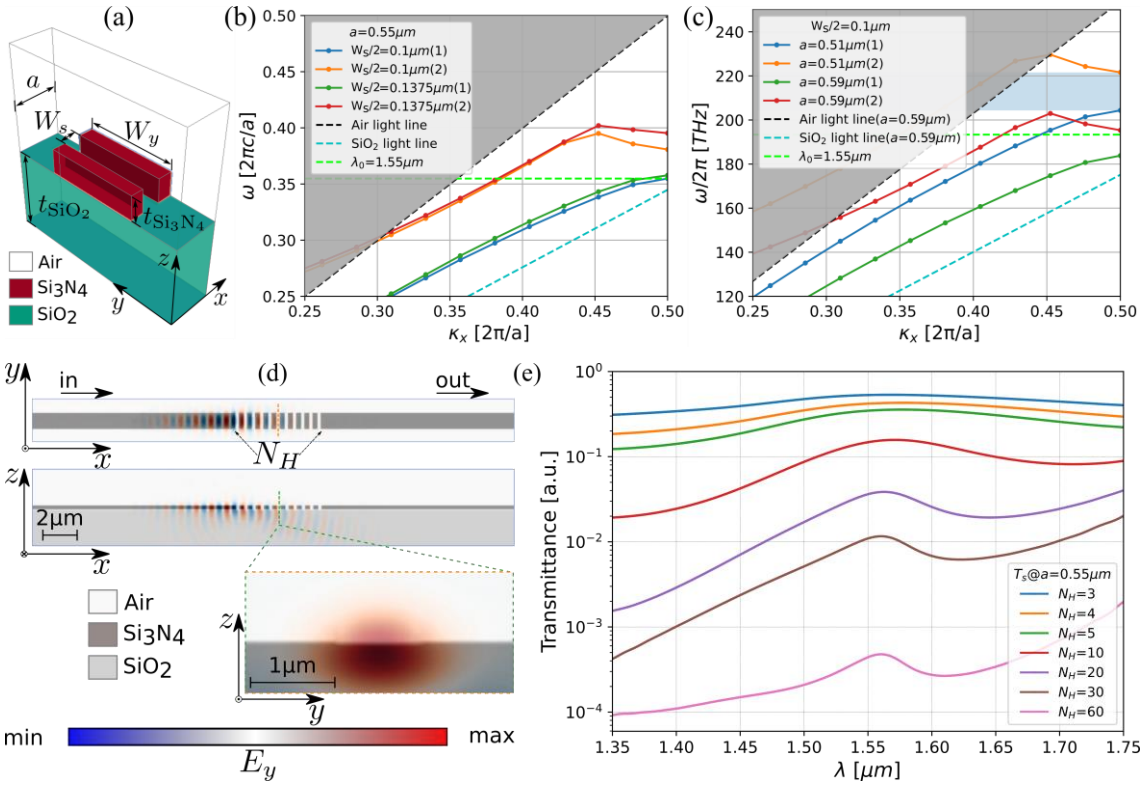

Figure 4.8 - (a) Air-based rectangular slots PhCN unit cell. (b) Band diagram of the TE-like modes, with the lowest two bands (1,2) shown for waveguides with large (W_s=0.275µm) and small (W_s=0.2µm) slot width for a fixed periodicity a=0.55µm. (c) Band diagram of the TE-like bands (1,2) for waveguides with large (a=0.510µm) and small (a=0.590µm) slot periodicity considering a fixed slot width W_s=0.2µm. The blue-shaded region between the two first guided modes corresponds to the photonic band gap. (d) Calculated E_y distribution of a broadband pulse time evolving in the dielectric distribution of the uncoupled PhCN region. (e) 3D-FDTD calculated transmission spectra for different numbers, N_H, of rectangular air-based slots with fixed a=0.550µm, W_s=0.275µm.

A snapshot of the electric field (E_y) propagating through the PhCN region is shown in Figure 4.8(d). The propagating mode's portion that is being pulled down to the substrate and scattered into the air is depicted in the 3D-FDTD simulation presented in Figure 4.8(d) [82]. By inspection, it is possible to verify that the first three air-based rectangular slots of the PTE exhibit a greatly scattered optical power of the propagating pulse. The field distribution inside the slot (low-index region) at the PhNC's symmetry plane is depicted in the cross-section of Figure 4.8(d). As a result, the dependence of the pure PhNC's transmission versus N_H is seen in the transmittance spectra shown in Figure 4.8(e). A higher number of rectangular slots will lead to a lower transmission coefficient for the frequencies that surround the band stop (~1.55µm Figure 4.8(e)). This numerical finding also validates the ability to alter N_H to change the transmission coefficient of the PTE-based PhCN (continuum) within the structure. Compared with the circular holes, the rectangular slots reflect a more drastic impact on the transmission amplitude.

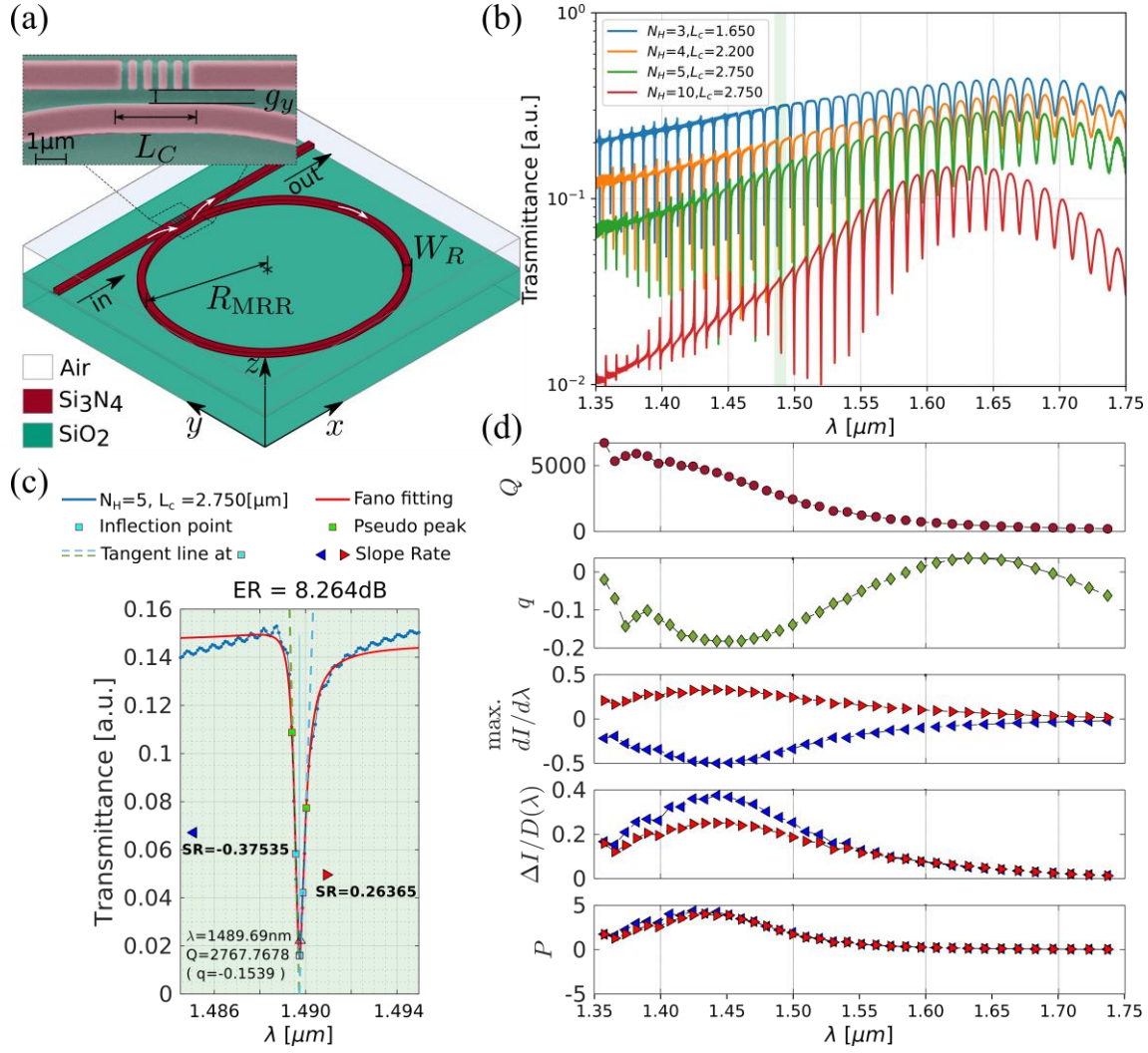

Figure 4.9 - (a) Air-based rectangular slots PhCN-MRR designed with fixed R_{MRR}, N_H=5, and L_C= $N_H a$. Upper-left inset shows the colored SEM image of one fabricated device. (b) 3D-FDTD calculated transmittance spectra of the device in (a) for different coupling length L_c and N_H. (c) Extracted Fano resonance parameters (Eq. 2-5) from the transmittance of the PhCN-MRR with L_c=2.750µm and N_H=5. (d) Extracted parameters from the full wavelength range of the simulated spectra in (b) and (c). The right and left tile of the resonance is drawn with a filled red and blue horizontally oriented triangle, respectively.

Figure 4.9 depicts the Fano resonator based on an air-based rectangular slot PhCN-MRR structure considered in this section. The racetrack MRR has a coupling section L_C, width W_R, and radius R_{MRR}, which corresponds to the number of lattice periods N_H on the PhCN. The coupling strength is determined by the interaction length (L_C) over which the waveguides are linked together and the gap separation (g_y) between them. As a result, the influence of N_H and L_C in the Fano, shape is analyzed using the 3D-FDTD. The computed spectra of the PhCN are displayed in Figure 4.9(b). The baseline in the transmittance of the PhCN-MRR is determined by the response of the uncoupled PhCN (see Figure 4.8 (d)), whereas the degree of asymmetry is determined by N_H.

The moderately high Q-factor (2768), the extinction ratio (ER=8.264 dB) in the Fano line presented in Figure 4.9(c), and the asymmetry (q=-0.15), result in a slope increment of around 1.5 compared with Lorentz shape. From the computed spectra shown in Figure 4.9 (b), Q, q, $\max\left(\frac{dI}{d\lambda}\right)$, $\Delta I/D(\lambda)$, and P are calculated at all wavelengths and presented in Figure 4.9(d). The Fano asymmetry parameter (-0.15) and average Q-factor (2768) for the sample resonance presented in Figure 4.9(c) can be further examined using the slopes at the two tails of the dip (λ_{dip}). At the inflection point, the maximum slope rate, $\max\left(\frac{\mathrm{dI}}{\mathrm{d}\lambda}\right)$, is related with a ratio of 0.38/0.26. Interestingly evolution of the Fano asymmetry parameter among all the wavelengths is enveloped by the modulation in the transmission coefficient of the PTE. Besides the highest Q-factor is not the one with the highest slope. Ideally, when the phase shift between the two interfering states is π/4 (~q=1), there is a maximum interference between the two states, and SR reaches its maximum value [111]. Conversely, for the resonance's extreme points ($\lambda_{\mathrm{dip}}, \lambda_{\mathrm{peak}}$), the slope $\Delta\mathrm{I}/\mathrm{D}(\lambda)$ decreases to about half for the left tile and remains constant for the right (refer to Figure 4.9(d)). To determine a consistent slope for the resonance dip, a pseudo-peak to locate a point in the linear zone (where the slope differs by no more than 10% from the slope at the inflection point), is used. In essence, both the pseudo-peak and the dip will be symmetric concerning the inflection points. Consequently, P, which considers the contrast (V) of the Fano line, likewise clearly illustrates the distinct difference between the slopes of the two tails of the resonance. Therefore, the suggested metrics validated through simulation that the PhCN-MRR resonator is capable of supporting Fano shapes. Therefore, a structure supporting Fano shapes at all resonance modes of the MRR is presented.

4.1.3. Fabrications and experimental results

The integrated Fano systems, discussed in section 3, have been fabricated through conventional nanofabrication processes in which the processing steps were adjusted to achieve the required circular and rectangle air-based holes PhCN-MRR.

A 4” bulk silicon wafer that had been thermally oxidized and had a BOX thickness of 2 µm was combined with a 300 nm thick Si_3N_4 layer that had been deposited using plasma-enhanced chemical vapor deposition (PECVD). Initially, the wafer was spin-coated with a 450 nm-thick layer of ZEP 520A resist. The target layout was generated in a bath of n-Amyl Acetate solution for 90 seconds and then washed with IPA after being patterned on the resist using electron beam lithography (EBL) at a power of 100 kV. Later, the patterns were transferred to the PECVD Si_3N_4 layer using an inductively coupled plasma (ICP) etch step with a 3:5 ratio and an etch rate of about 45 nm/min in SF_6:CHF_3 chemistry. The remaining resist was eliminated with an O_2 plasma ashing phase and a 30-minute immersion in 1165 remover. Finally, a cleaning cycle using IPA, Acetone, and Piranha etching was carried out.

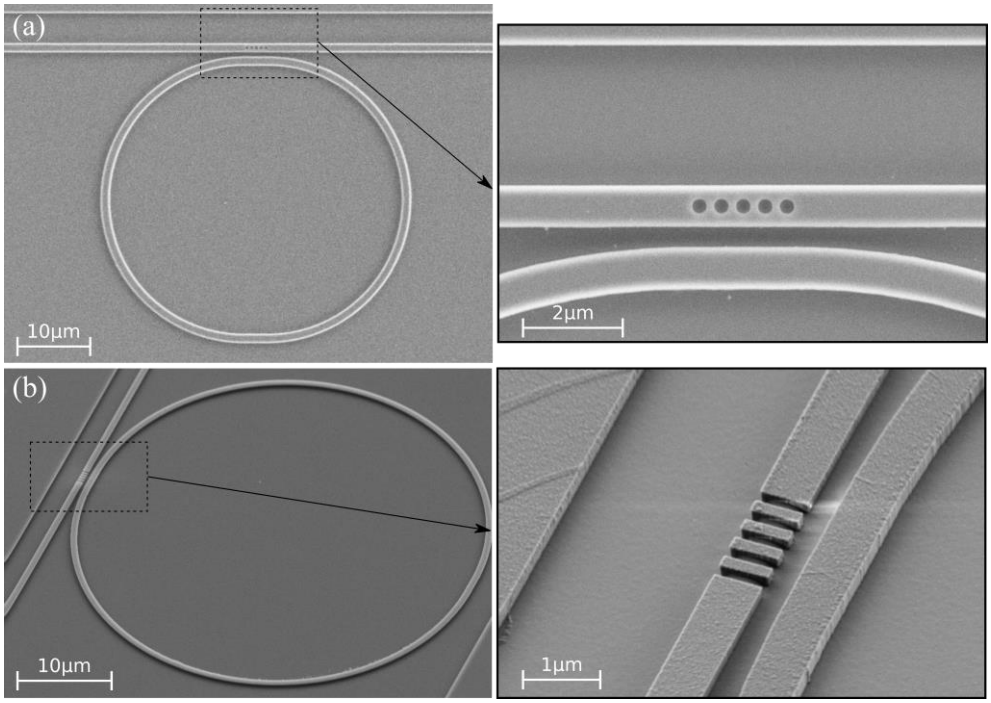

Figure 4.10 - Scanning Electron Microscope images of the fabricated devices on a Si_3N_4 slab (0.300µm thick). (a) Top view of the fabricated air-based circular holes PhCN-MRR. Detail of the coupling region with fixed a=0.550µm, r=0.150µm and g_y=0.350µm. (b) Lateral view of the fabricated air-based rectangular slots PhCN-MRR. Zoomed image of the coupling region a=0.550µm, $2r$=0.200µm and g_y=0.450µm. The fabrication work was done in conjunction with Artem Vorobev.

An end-fire setup (like the one in [1]) was used to optically measure the produced devices. A hybrid system of fibers and spot-size conversion lenses is used to butt-couple the light from an ASE broadband source (Amonics ALS) into the waveguide. The spectral response of the devices under test is obtained through an optical spectrum analyzer. To switch between TE-like (in-plane) and TM-like (out-plane) modes at 1310 nm, polarization optics were added to the actual setup to adjust the propagating polarization along the waveguides.

4.1.3.2. TE-like mode at C-band

The fabricated devices in both configurations: circular holes and rectangular were characterized for different operation scenarios. At first, the TE-like operating at Telecom C-band was considered. The waveguide's dispersion relation presented in section 4.1.2.1 ensures the single-mode operation of the intended MRRs at 1.550µm. Consequently, a study on a collection of air-based circular hole PhCN-MRRs, wherein both the number of PTE's unit cells (N_H) and the coupling gap (g_y) were systematically varied, while keeping all other parameters constant, as illustrated in Figure 4.10(a), was performed. The spectrum depicted in Figure 4.11(a) showcases the presence of high Q-factor resonances (with values reaching 10^3) and a notable Fano asymmetry parameter (>0.15) for all resonances within the C-band. The measurement in Figure 4.11(a) was achieved in the air-based circular hole PhCN-MRR with a fixed N_H=5 and g_y=0.250 µm.

In Figure 4.11(b), a series of fabricated optical devices designed with a fixed gap g_y of 0.250 µm, alongside lattice periodicity and air-hole radii of 0.55 µm and 0.15 µm, respectively, is presented. Subsequently, the corresponding spectra, centered around 1564 +/- 3 nm, for varying numbers of PTEs (N_H = 3, 4, 5) are shown in Figure 4.11 (c-e). The observed shift in the resonant wavelength is a direct consequence of alterations in the resonant condition,

arising from slight changes in the PhCN's lattice unit and the resultant modification in the roundtrip length of the MRR [64].

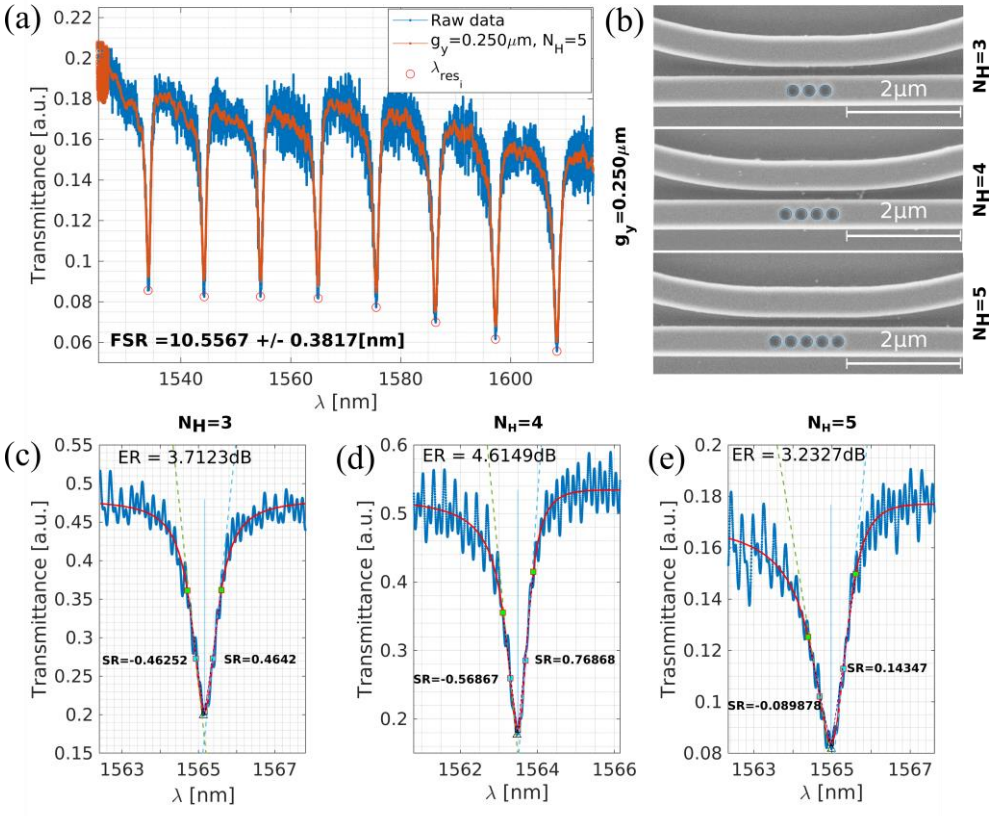

Figure 4.11 - TE-like (C-band) red-parity Fano spectrum obtained by (a) Air-based circular holes PhCN-MRR with constant values of g_y=0.250µm and N_H=5. (b) Top view of the manufactured resonators with constant values of g_y=250µm and N_H=3,4,5. (c-e) Specific resonances originating from PhNC-MRR with g_y=0.250µm and N_H=3,4,5 respectively. The dataset is represented in blue, with the Fano fit shown in red. Furthermore, visual markers denoting the experimental dip (depicted as a black triangle), the fitted dip (represented by a black square), the inflection point (indicated with a cyan-filled square), and pseudo peaks (distinguished by green-filled squares) are included. This work was done in conjunction with Artem Vorobev.

To analyze the experimental data, the spectrum (blue) was fitted with equation (1) shown in red. This fitting process allowed us to extract key parameters, including the linewidth (Γ), Q-factor (Q), Fano asymmetry parameter (q), and the slope rate (SR). Notably, a fitting window width equivalent to 50% of the Free Spectral Range (FSR) for resonance, was considered. The SR was calculated at the inflection points on both sides of the resonance dip, where the maximum $dI/d\lambda$ is achieved. The observed trend revealed that the asymmetry (q) consistently increased with higher values of N_H, displaying a ratio of 0.2037/0.0016. Meanwhile, the Q-factor experienced a decrease from $2{\cdot}10^3$ to $1.5{\cdot}10^3$ as the extinction ratio (ER) reduced.

One interesting observation among Figures 4.11(c-e) is the proportional relationship between the SR, Q-factor (narrow linewidth), and q (higher ER) concerning the characteristics of the Fano device with N_H=3. Moreover, analysis of other configurations of PhCN-MRRs with different g_y values (0.250 µm, 0.350 µm, and 0.450 µm) were conducted. Notably, high-Q and low asymmetry (q) in devices with broader gaps are observed. This aligns with the observations in the 3D-FDTD simulations, as presented in Figure 4.7(b) [64]. This strengthening of the Fano effect at lower wavelengths is attributed to the localized wavelength range where the stop band's edges manifest [118].

Second, a set of air-based rectangular holes PhCN-MRR is characterized. In Figure 5(a), the device's transmittance shows an unambiguous periodic Fano resonance pattern characterized by an FSR of approximately 10.3248 +/- 0.6626 nm. Notably, this dataset enables the observation of variations in the Fano effect concerning wavelength across the entire range of measured spectra and the pair (N_H, L_C).

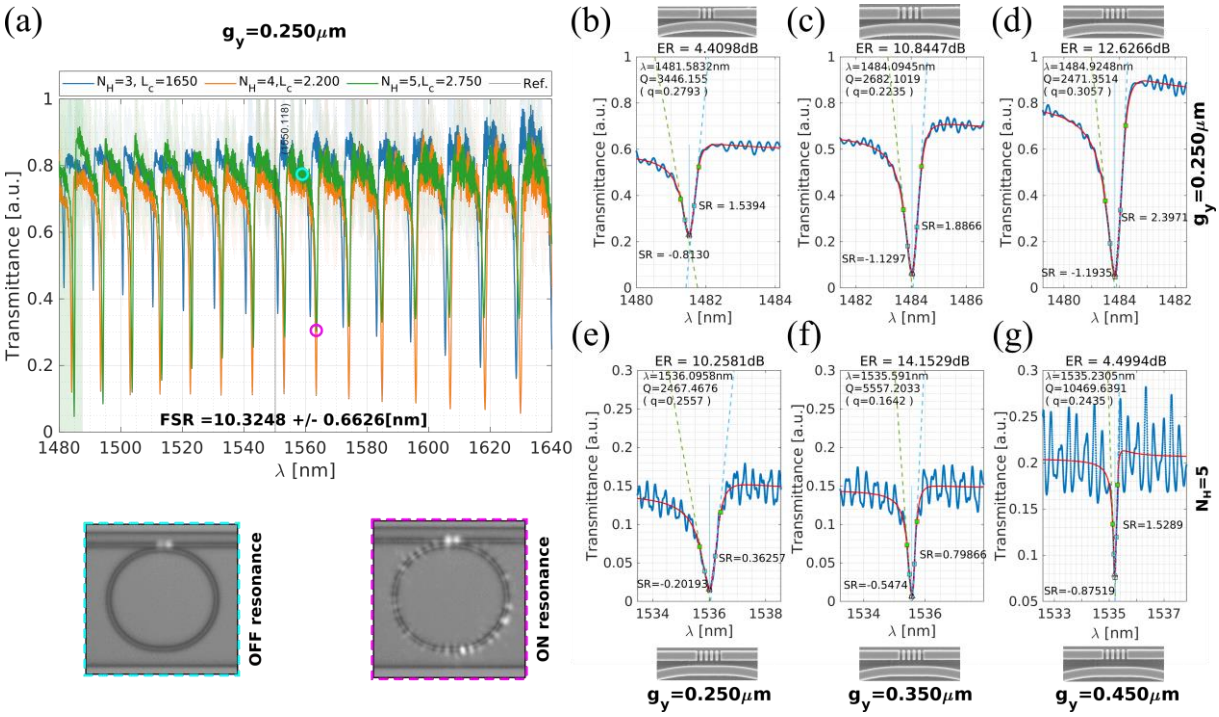

Figure 4.12 - (a) TE-like (SLC-band) blue-parity Fano spectrum obtained for (a) Air-based rectangular slots PhCN-MRR featuring a fixed g_y=0.250µm and varying N_H=3,4,5. Top SEM image in the NIR region of the fabricated device when it is subjected to light at the wavelengths corresponding to both the ON and OFF resonance states. (b-d) Experimental and fitted Fano resonance curves for the PhNC-MRR with specific wavelengths centered around 1485 +/- 5 nm wavelengths considering different values of N_H= [3,4,5]. (e-f) Measured transmittance of the PhCN-MRR with N_H set at 5, while the coupling gap (g_y) is varied, taking on values of 0.250 µm, 0.350 µm, and 0.450 µm. This work was done in conjunction with Artem Vorobev.

In Figure 4.12(b-d), a series of distinct devices with a fixed coupling gap (g_y) of 0.250 µm is presented, offering a systematic investigation of the influence of N_H. A decrease in the Q-factor by approximately 20% is observed as N_H increases from 3 to 5. This decrease can be attributed to the broadening of the blue shift of the dip compared to a Lorentzian profile. Simultaneously, the Fano asymmetry parameter experiences a consistent increase of 9%. It is important to stress the enhancement observed in the slope rate (SR), which increases by approximately 1.55 times, and the ER, which exhibits an approximately threefold increase. This observation implies that the fine-tuning of the gap (g_y) for critical coupling is no longer a stringent requirement. The amplitude ratio between discrete and continuum states significantly contributes to the enhancement of the ER of the Fano resonance [133]. Consequently, N_H can effectively modulate this amplitude ratio between the quasi-guided mode through the PhCN and the discrete resonances of the Micro-Ring Resonator (MRR). On the other hand, Figure 4.12(e-g) a set of PhCN-MRR with fixed N_H critical coupling is anticipated at a gap size of 0.350 µm. However, it's important to note that despite a twofold increase in the Q-factor for a gap size of g_y=0.350 µm (as shown in Figure 4.12(f)), the ER experiences a decline. This trend persists for the PhCN-MRR with a coupling gap of g_y=0.450 µm (as shown in Figure 4.12(g)), where the Q-factor elevates to approximately 1.05 x 10^4 (5-

fold). However, the SR increases consistently. Despite the Fano asymmetry parameter (q) being comparable to that of the g_y=0.250 µm configuration, the ER is reduced at broader gap sizes.

4.1.3.3. TM-like mode at O-band

TM-like modes, characterized by their perpendicular orientation to the chip plane, exhibit notable distinctions in their electric field intensity profiles when compared to TE-like modes within a rectangular-core waveguide. In this case, a significant proportion of the electric field intensity is distributed both above and below the waveguide core, extending into the surrounding cladding and substrate. Therefore, a more pronounced interaction between light and matter is expected. In the context of applications related to liquid sensing, it has been demonstrated that losses due to water absorption are 10 times lower at wavelengths around 1310 nm in comparison to those at 1550 nm [73].

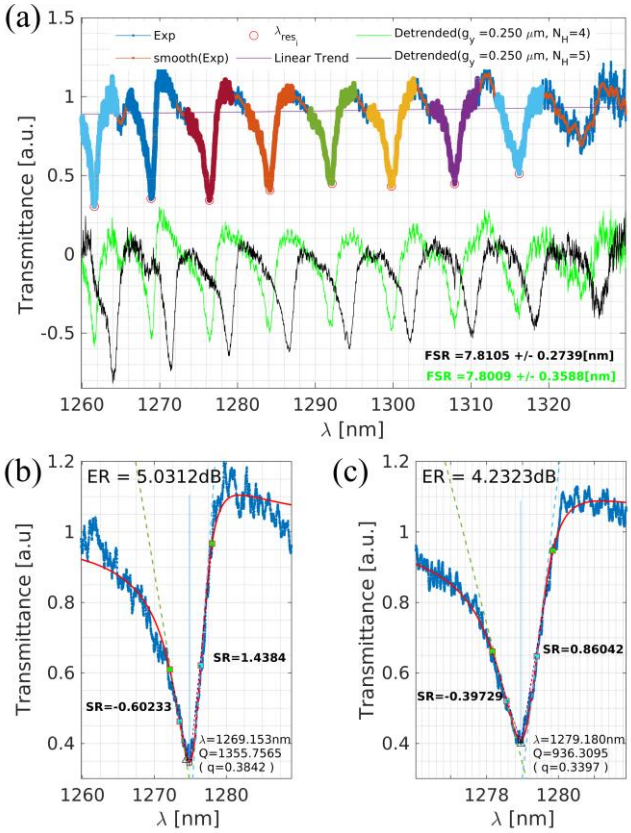

Figure 4.13 - TM-like (O-band) Fano spectrum of the air-based circular holes PhCN-MRR with constant g_y=0.250µm and varying N_H= [4,5] are measured (depicted in green and black, respectively). the diverse set of colors overlaid on the experimental data corresponds to the specific number of data points considered for each resonance. (b-c) Selected resonances originating from PhNC-MRR with g_y held at 0.250µm and N_H set to 4 and 5, respectively. This work was done in conjunction with Artem Vorobev.

To illustrate this point further, a detailed comparison involving a Si_3N_4 MRR utilized as a biosensor has been conducted [73]. This comparison involves the MRR operating around 1550 nm with the TE mode and at 1310 nm with the TM mode. Note that the cross-section of the waveguide used in this biosensor is consistent with those employed in the fabrication of the Fano device reported in Figure 4.11 (width of 1.1 µm and thickness of 0.3 µm). For consistent comparison across resonators operating within different wavelength ranges, a normalized sensitivity has been introduced (refer to Chapter 2). The improved sensitivity observed when utilizing the TM mode at 1310 nm in aqueous solutions makes it reasonable to focus on

enhancing the shape of the resonance using the Fano effect, with the slope of the resonance being the pivotal determinant factor[63].

In Figure 4.13 (b-c), the calculated parameters for the PhCN-MRR with air-based circular hole design, maintaining a fixed coupling gap (g_y) of 0.250 µm and varying N_H to 4 and 5, are presented. A direct relationship between increased asymmetry and a higher slope rate (SR), is evident in Figure 4.13(b). This connection implies that greater asymmetries result in more substantial variations in the slopes of the Fano line. Moreover, ER in this configuration exceeds the values found in TE cases shown in Figure 4.11 (c-e). The dispersion introduced by the fitting process, which arises due to the number of data points included, is explored. Figure 4.13(a) visually represents this by employing a range of colors to schematically depict the dataset per resonance. When the feature under scrutiny (the Fano line) isn't fully reconstructed, particularly the peak and dip, an increase in uncertainty regarding the fitted parameters is obtained. However, it's important to note that the measurements performed consistently display good agreement, with a goodness-of-fit exceeding 75% for window sizes corresponding to a fraction of the FSR (>25%). In contrast to Figure 4.13(b-c), a distinct influence of the coupling gap width was observed in the experimental characterization of complementary devices. As this parameter increases from 0.250 µm to 0.450 µm, there is a corresponding rise in the Q-factor alongside a reduction in asymmetry. This is directly associated with changes in the slope rate (SR), which either increases or decreases in proportion to the Q-factor alterations.

4.1.3.4. Water cladding

According to the motivation in the previous item, the performance of the rectangular slot PhCN-MRR in the presence of aqueous solutions was performed by a drop cast experiment with deionized water (DIW).

In Figure 4.14(a), the drop-casting experiment is schematically illustrated. It involves a newly fabricated Si_3N_4 PhCN-MRR placed on a thermally stabilized holder and completely covered with a drop of deionized water (DIW). Figure 4.14(b) showcases an increase in the Fano asymmetry parameter (q) while maintaining a consistently high Q-factor within the targeted spectral range. Simultaneously, the relative variations in the slope rate (SR) consistently align with the discussions on asymmetry. Figures 4.14(c) and 4.14(d) present the sample resonances for the rectangular slot PhCN-MRR with air and water cladding, respectively. These plots reveal a q increment of approximately 1.55 times when a drop of DIW is introduced. Additionally, the relative ratio of the slopes is approximately 2, which, in conjunction with the differences in the heights of the inflection points (cyan-filled squares) on the resonance curves, reaffirms the anticipated Fano-like shape.

Despite the increased asymmetry, it's noteworthy that the ER of the resonance in the case of water cladding is approximately half that of the air-cladding, representing the typical behavior of most devices with a fixed coupling gap (g_y) of 250 µm. As the coupling gap widens, the Q-factor increases by about two-fold along with the ER, reaching approximately 18 dB, and a natural enhancement in SR. However, the Fano asymmetry parameter experiences a drop. It's worth mentioning that each coupling gap configuration results in a different coupling rate between the PhNC and the MRR. Consequently, a higher Q-factor in the discrete resonance (MRR) signifies an improvement in the Fano shape. As a result, wavelength shifts and asymmetry can be associated with the real and imaginary components of the refractive index in the upper cladding, as demonstrated in [122]. Based on these findings, the Si_3N_4 rectangular

slot PhCN-MRR emerges as a promising candidate for applications in sensing, whether for liquids or gases. 3D-FDTD simulations estimate a bulk sensitivity of at least ~156 [nm/RIU] for a waveguide-MRR structure in the presence of water. Furthermore, there is a clear enhancement of the Fano asymmetry parameter (q) with the N_H for the tested devices. This reaffirms the dependence of the Fano shape on both N_H and g_y. Importantly, even though the device was originally designed to operate with TE-like modes and air cladding, and improved performance for water as a cladding, further optimization can be pursued to enhance the sensitivity of a photonic transducer based on Fano resonances, particularly within an intensity-based scheme for refractive index sensing [63].

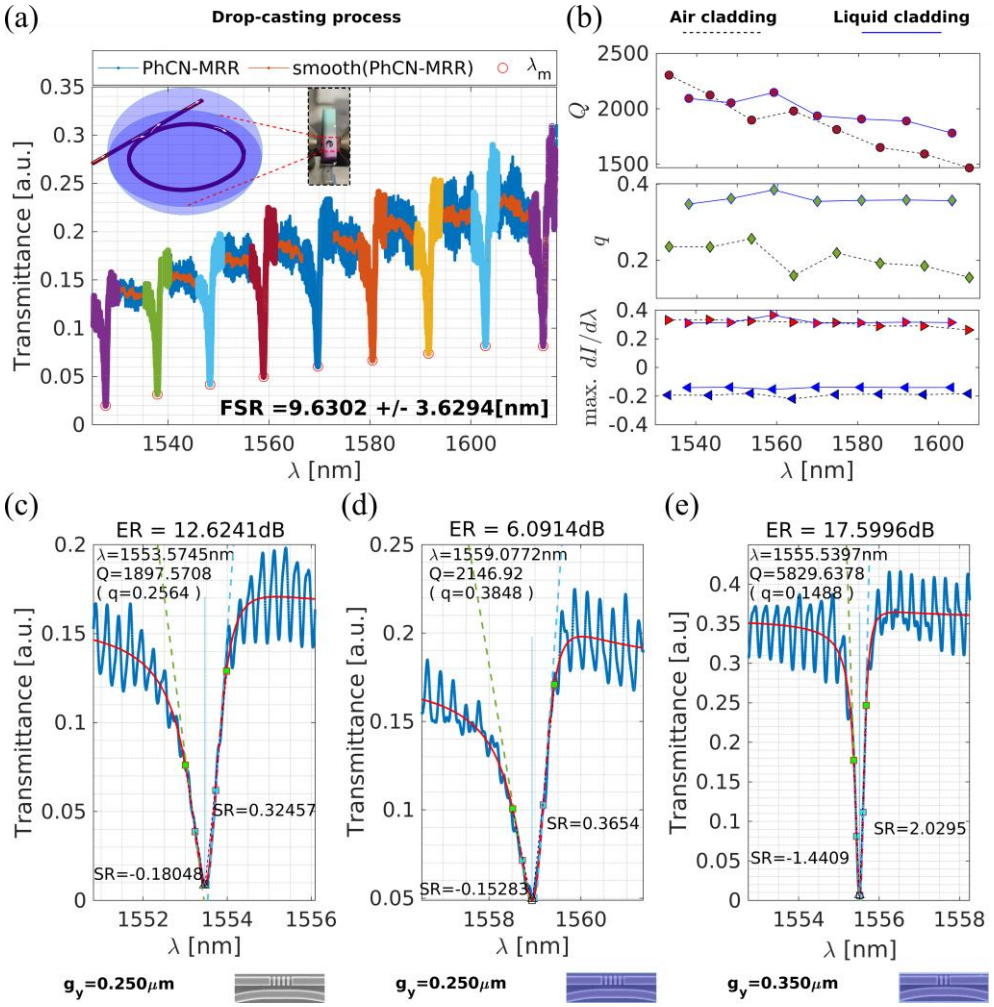

Figure 4.14 - (a) TE-like (C-band) Fano spectrum for rectangular slots based on PhCN-MRR while they are immersed in water. The device maintains fixed parameters set to g_y=250µm and N_H=5. An inset in this figure depicts a schematic representation of the drop-casting procedure employed. (b) Calculated metrics encompassing Q, q, $\max(dI\backslash d\lambda)$ of the manufactured device. This analysis considers two distinct upper cladding conditions: one with deionized water (DIW), depicted by the blue-filled line, and the other with air cladding, represented by the black dashed line. (c) Experimental blue-parity Fano resonance is obtained when the upper cladding consists of air. (d) A closer look at the Fano resonances observed in devices with water as the upper cladding material. (e) Transmittance for PhCN-MRR with g_y=350µm and N_H=3 for water cladding. This work was done in conjunction with Artem Vorobev.

4.2. Summary & Perspective

A novel and compact approach to realize a high Q-factor and a substantial Fano asymmetry parameter (q) in Si_3N_4 Photonic Crystal Nanobeam-assisted Micro Ring Resonators is demonstrated experimentally. This innovative structure yields a Q-factor of 10^4 and a remarkable Fano asymmetry parameter (q) for both air and liquids, specifically deionized water (DIW). The performance of the PhCN-MRR structure can be carefully tuned based on factors such as the coupling gap (g_y), geometry (circular hole or rectangular slot), and the length of the PhCN region (N_H), significantly impacting both the Q-factor and q-asymmetry.

Almost destructive interference within a narrow resonance bandwidth of approximately 100 pm, is achieved. Notably, the fabricated Si_3N_4 PhCN-MRRs offer portability, compactness (lab-on-a-chip), a high Fano asymmetry parameter (q, up to ~0.4), sensitivity (~160 nm/RIU), and a straightforward design and manufacturing process. Moreover, the device offers the flexibility for separated control of both Q-factor and q-asymmetry, making it a strong contender for refractive index sensing applications.

Of particular significance is the operational versatility of the developed devices, operating with TE-like modes at 1550 nm, as well as TM-like modes at 1310 nm for both air and liquid solutions. This adaptability offers valuable insights into strategies for sensitivity enhancements compared to prior implementations primarily focused on single-mode TM at 1310 nm [73].

In summary, a fully integrable and compatible refractive index sensor based on Fano resonances, offering promising prospects for a wide range of applications in the field of photonics and optical sensing, is presented. In the context of PTS, the inherent improvement in the slope of the resonance will directly enhance sensitivity and the limit of detection. This is particularly significant for optimized systems where the transduction mechanism involves detecting the optical intensity at a fixed wavelength, such as at the inflection point of the resonances. The excellent results, among other features, are derived from proper tracking of the slope of the resonances used to transduce the PTS signal [9,10,134]. Therefore, the current implementation of PTS systems could further benefit from the Fano shape. Additional improvements will be realized through a rigorous comparison with a suitable model that can consider the direct characteristics of the PTE including in the Fano design [111].

Furthermore, surface functionalization with a biorecognition layer deposited onto the PhCN-MRR introduces the potential to modify the effective refractive index of guided modes through selective binding of target molecules[19]. This feature could add a layer of selectivity to the proposed Fano resonator.

Chapter 5 - MICROFLUIDICS INTEGRATION

The Silicon Nitride photonic refractive index sensors discussed in the previous chapters have been developed to achieve enhanced Q-factor and sensitivity through various design scenarios. Simultaneously, these sensors aim to minimize the required sample volume for transducing photo-induced refractive index changes. Therefore, a strategy to manage low sample quantities, whether in gas or liquid phases, is essential [30].

Microfluidics is a multidisciplinary field that deals with the manipulation of extremely small fluid volumes, typically ranging from 10^{-9} to 10^{-18} liters, within microchannels sized between tens and hundreds of micrometers. The primary advantage of microfluidics lies in its ability to reduce reagent consumption for analysis due to the miniaturized channel dimensions, resulting in much smaller sample volumes, typically measured in femtoliters to nanoliters [135]. Similarly, concerning analytical chemical separation systems, microfluidic systems also allow for fast analysis. This technological approach also paves the way for the development of portable on-site testing devices applicable in various contexts, including micrototal analysis systems (μTAS)[136], lab-on-a-chip (LOC)[137] platforms, actuators[138], and compact point of care (POC) devices[137]. These devices are designed to incorporate multiple functions such as mixing, sorting, temperature control, fluid pumping, sensing, detection, and analysis, all within a user-friendly and cost-effective format[139].

Advanced optofluidic integration techniques enable POC tests with simultaneous multiplexed detection for multiple targets, automated sample processing within a single chip, and reduced dependence on off-chip components[135]. Successful integration of photothermal spectroscopy, with micro/nanofluidic devices has been achieved, particularly, those based on thermal lens spectroscopy using a microscope [140]. This chapter presents a demonstration of successful microfluidic integration of a single-etched Si_3N_4 chip in a microfluidic system. for refractive index sensing.

5.1. Material platforms

When selecting a material platform for microfluidic channels, it's crucial to consider the degree of integration, functionality, and utilization one requires. Additional aspects like optical transparency, compatibility of solvents, and gas permeability also have to be considered.

Silicon and glass were the first types of materials adapted to the design of microfluidics [141]. Silicon allows for fabrication through both additive and subtractive methods. However, its high elastic modulus presents challenges in creating high-performance microfluidic components like valves and pumps. Surface modification with silanes, introducing silanol (-Si-OH) groups, has been successfully employed in various biological applications[142].

Furthermore, silicon is transparent to infrared but not visible light, but this limitation can be addressed by incorporating transparent substrates such as glass or polymer in hybrid systems.

Microstructures on glass are typically created using wet or dry etching techniques [143]. For sealing, thermal fusion bonding is widely adopted, and the performance of the channels is sensitive to temperature pretreatment. Consequently, it is necessary to maintain the cleanliness and smoothness of the glass surface. Furthermore, glass exhibits biocompatibility, minimal nonspecific adsorption, and impermeability to gases, making it highly suitable for microfluidic applications[142].

Within the domain of microfluidic device fabrication, polydimethylsiloxane (PDMS), an elastomer, has been a predominant choice for use as substrate material since the 1990s and continues to play an important role in contemporary applications. PDMS is favored for its accessibility, cost-effectiveness, and fast fabrication processes. The liquid prepolymer can be thermally cured at moderate temperatures (typically ranging from 40 to 70 °C), rendering it compatible with nanometer-scale casting facilitated by photoresist templates [144]. These templates, significantly more straightforward and economical to prepare than their silicon or glass counterparts, allow for easy separation of PDMS due to its inherently low surface energy. PDMS-based microfluidic chips can be sealed reversibly, enabling conformal integration with other PDMS chips, glass, or diverse materials via straightforward surface contact. Irreversible bonding, on the other hand, can be accomplished by either oxidizing the PDMS surface using plasma treatment or employing a thin PDMS layer as an adhesive.

PDMS microfluidic devices are extensively applied, particularly in areas such as cell screening, cell culture, and biochemical assays. Its remarkable capability to manipulate reduced amounts of liquid volumes, down to picoliter and femtoliter scales, makes it an invaluable tool for conducting single-cell analysis [145]. One notable advantage of PDMS is its gas-permeable nature, a feature indispensable for sustained cell culture in hermetically sealed microchannels. However, it is important to note that PDMS favors bubble formation due to its gas-permeable nature, a challenge that must be addressed in experiments and designs.

On the other hand, thermoplastics represent a class of polymers that exhibit the unique property of becoming pliable and moldable when heated to their glass transition temperature (T_g). Upon cooling, they solidify once again. Researchers can leverage this property to fabricate diverse structures using various polymer processing methods, including injection molding and compression molding [142]. PMMA, PS, and PC are some examples of thermoplastic materials.

Poly (methyl methacrylate) (PMMA) is synthesized from methyl methacrylate polymerization. PMMA can be patterned via injection molding or hot embossing, making it suitable for the creation of thermoplastic microfluidic networks. It possesses an elastic modulus of 3.3 GPa, excellent optical transparency spanning from visible to UV wavelengths, and can be modified to enhance resistance against alkali, acid, and organic solvents. Various methods have also been applied to adjust the wettability of PMMA surfaces[146]. However, it's important to note that long-term exposure to organic solvents and high temperatures can lead to the deformation of PMMA channels, which imposes limitations on its extended use in certain applications.

Polystyrene (PS), derived from the polymerization of styrene, is typically solid at room temperature but can be molded when heated to its T_g at around 100 °C. To enhance its hydrophilicity, surface modifications like plasma oxidation or chemical treatments are

necessary. PS-based microfluidic devices show promise for cell culture applications, addressing the non-specific adsorption issue associated with PDMS devices[147].

On the other hand, Polycarbonate (PC), synthesized from bisphenol A and phosgene, boasts low moisture absorption, high resistance, and an excellent T_g (approximately 145 °C). It has found utility in polymerase chain reactions. However, limitations include susceptibility to specific organic solvents and UV absorption[148].

Additionally, there are innovative approaches to accelerate the concept-to-chip development process. For instance, pressure-sensitive adhesive (PSA) tapes, that can be micro-structured, and efficiently bond various industrial-relevant polymeric materials like PMMA, PC, PS, cyclic olefin polymer (COC/COP), and polyethylene terephthalate (PET/PETG). This means that the same types of polymeric materials can be used consistently in the entire chip development process. Therefore irreversible bonding between PDMS and PMMA mediated by a double-sided PSA tape has been demonstrated [149,150].

5.2. Bonding Strategies

Sealing is extremely important in microfluidic device fabrication. A key challenge involves achieving strong and reliable bonding, given the relatively weak interactions between substrates [142]. Suboptimal bonding can lead to the formation of air bubbles between bonded surfaces, resulting in leakage and compromising the quality of microfluidic devices. Consequently, numerous research efforts are dedicated to developing robust sealing techniques that can significantly enhance the commercial viability of these devices.

Sealing strategies have been extensively studied for the development of robust techniques that can be used in specific scenarios, such as PDMS with rigid surface materials like thermoplastics (e.g., PMMA). The use of one or two silane reagents can produce a surface chemical modification in PDMS that turns into a stronger bond. Key attributes, including the types of substrates involved (e.g., PDMS-PMMA), the strength of the bond, and the bonding conditions (e.g., temperature, pressure, and duration), have been compiled in [142]. A shared characteristic of these approaches is the use of O_2 plasma treatment on the surfaces to facilitate bonding, followed by surface modification with compounds like 3-aminopropyl triethoxysilane (APTES), among others.

In this context, a novel and cost-effective approach has been devised to establish a robust bond between PMMA and PDMS layers at room temperature within less than 5 minutes. This method combines the use of biocompatible adhesive tape and oxygen plasma treatment. The resulting PDMS-PMMA bond exhibits hydrolytic stability and can handle high fluid flow without any risk of leakage[149]. The Pressure Sensitive Adhesive (PSA) does not require any chemical treatment. Acrylic-based PSA tape and silicon-based PSA tape are recognized by their biocompatibility, addressing concerns related to direct contact with substances inside the microchannels.

A pressure-sensitive adhesive tape consists mainly of elastomers such as rubbers, acrylates, and silicones. The simplicity in application compared to liquid adhesives, and reduced assembly time for microfluidic devices make it pertinent for rapid prototyping. Their use ensures a uniform adhesive layer at the interface of two substrates. PSA tapes have demonstrated their capability to resist high pressure and elevated temperatures without

deformation or entering microchannels, thus mitigating concerns regarding microchannel blockage.

5.3. Integration with Si_3N_4 Photonic Cavities

Usually, Si/Si_3N_4 chips have a deposited cladding layer of SiO_2 to protect the device and enhance the guiding capabilities of the waveguides[30]. Then, a set of localized opening widows is created to expose the photonic cavities (e.g., MRR, PhCNC) to the sample. Later, the microfluidic channel on top will carry the target fluid towards the refractive index transducers. The presence of silica is highly convenient for its compatibility with PDMS surfaces. It allows after oxygen plasma treatment a robust sealing facilitated by hydrogen bonding. One drawback is that one requires at least two steps in the fabrication of the integrated chip to create the opening windows in the deposited layer of silica.

The earlier introduced pressure-sensitive adhesive as a ready-to-go strategy for robust bonding, can also be microstructure. Despite, there being no reported strategies that combine Si_3N_4 surfaces with PSA for microfluidics, its micro structuring capability was exploited and the realization of bonded microchannels in the top of a single etch Si_3N_4 chip was demonstrated. The micro structuring of PSA offers several advantages, including enhanced design flexibility, quick fabrication, and easy assembly of biochips.

Four biomedical-grade adhesive materials that are quick to use for making prototypes (<1 hour), were carefully examined in [150]. Their precision, physical and optical properties, as well as compatibility with biological systems, were studied. Although all four adhesives were found to be biocompatible, additional characterization to highlight significant differences in their cutting behavior, adhesion to glass and polymers, and gas permeability, was conducted.

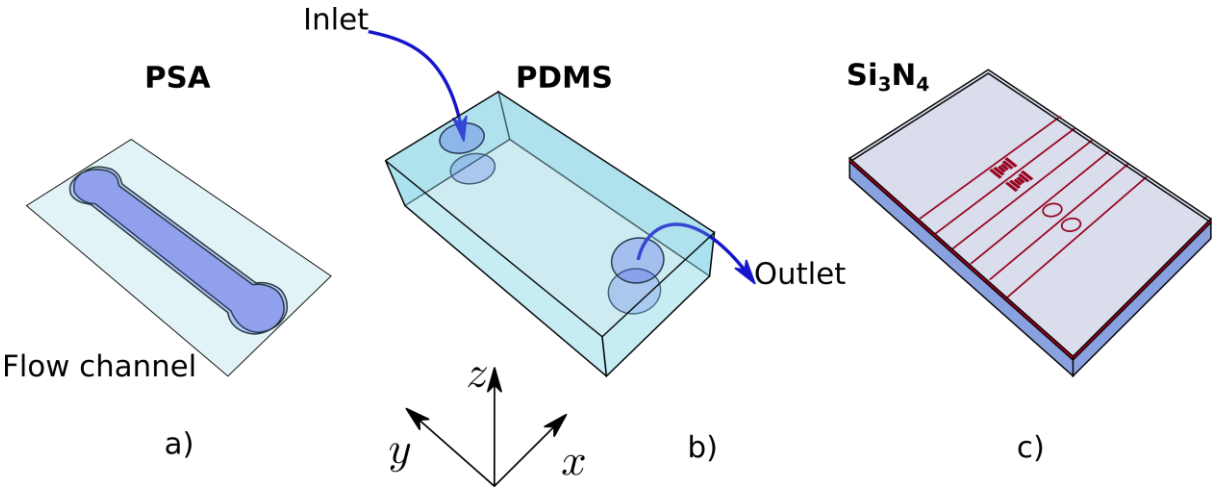

Figure 5.1 - (a) PSA Microstructure (b) Cut PDMS foil (c) Si_3N_4 chip with integrated refractive index transducers.

The established collaboration with the Cell Chip group at TU Wien led by Prof. Peter Ertl and his student Dipl.-Ing. Silvia Schobesberger allows to have support in the fabrication of microfluidics channels based on PSA. The adhesive used was a transparent double-sided pressure-sensitive adhesive tape containing a 12.7 µm thick polyester film with MA-93 as acrylic pressure-sensitive adhesive (17.78 µm on each side) with a total thickness of 48.26 µm (with liners 149.86 µm).

The following protocol produced reliable results in creating a microfluidic flow cell on the chip for liquid handling:

- PDMS casting
- CAD drawing with the shape of the channel and PDMS foil. For the test reported in this document a straight channel with ~2mm long and 0.5mm width has been realized. The depth of the channel will be ~50µm.
- The adhesive (with liners) was cut, using a vinyl cutter, and prepared for bonding. This implies the removal of the excess adhesive that will create the opening for the channel (see Figure 5.1(a)).
- The square PDMS foil, previously cut at a similar size to the Si_3N_4 chip is prepared with punched 1.5 mm holes for inlet & outlet access (see Figure 5.1(b)).
- Oxygen plasma bonding of PDMS and adhesive is performed (see Figure 5.1(a)&(b)).
- Bonding to Si_3N_4. (see Figure 5.1(a-b) &(c)).
- Strength bonding for one hour at room temperature, the chip is fixed between two glass slides with clamps.

To ensure the bonding the chip was tested with a peristaltic pump at a rate of 132µL per minute for 5.5 hours without any leakage. Later tests demonstrated that after one month of fabrication, the bonding was still tight.

5.4. Refractive index Sensing

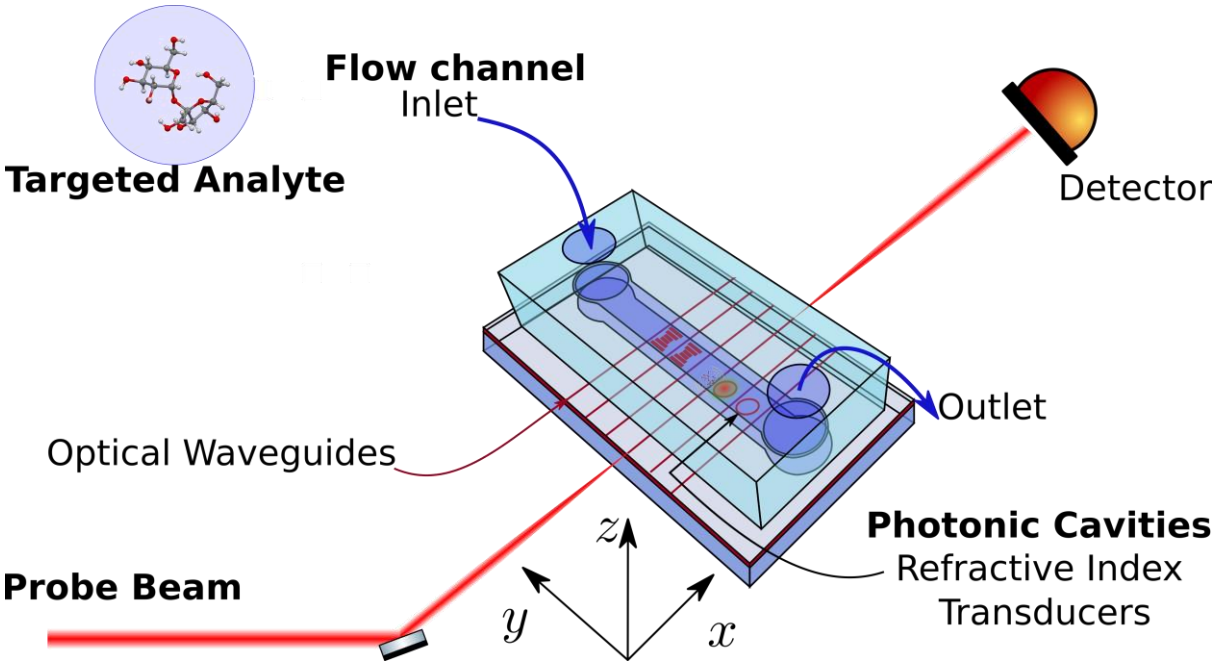

Figure 5.2 - Schematic of the characterization carried out with the fabricated microfluidics and the Si_3N_4 refractive index transducers designed.

Once the microfluidic cell has been achieved, a refractive index sensing experiment can be carried out. Figure 5.2 shows a schematic of the intended experiment. The light emitted from a probe beam is butt-coupled to the Si_3N_4 chip. The light guided through waveguides is side coupled to the photonic cavities, previously designed, whose upper cladding is exposed to the liquid flowing in the microfluidic channel. At the output, a detector interrogates the changes in the features of the resonators that will transduce any refractive index variation in the fluid.

Such refractive index variations are first mimicked by the variation of the target analyte concentration. The target analyte will be flowing through the inlet and outlet ports associated with the microfluidic cell.

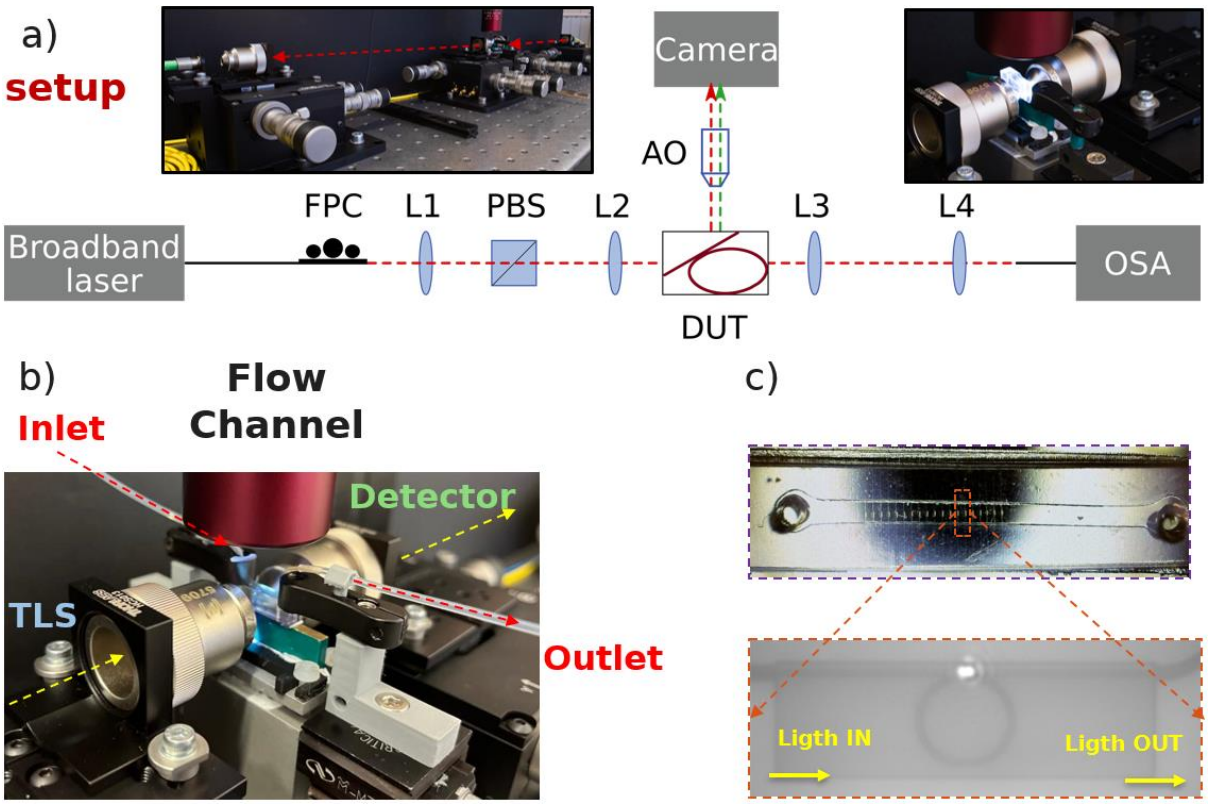

Figure 5.3 - Experimental setup for the characterization of the fabricated devices [1]. Lenses (L1, L2, L3, L4), Polarization Beam Splitter (PBS), Microscope Objective (AO), Fiber Polarization Control (FPC), MRR-PhCN (DUT) (b) Close view of the experimental setup at the interface between liquid handling and optics. Tunable Laser Source (TLS) (c) Top view of the fabricated microfluidic channel bonded to the Si_3N_4 chip. Detail of the light scattered in the devices while there is a constant flow (up to down) and light is coupled (left to right).

Figure 5.3(a) shows a schematic of the experimental setup addressed, with some real view insets, to reproduce the schematic in Figure 5.2. In this sense, the probe beam corresponds to an NIR laser directed into the waveguide using a system of fibers and spot-size converting lenses. The resulting optical output from the waveguide, which carries the cavity's spectral response, was collected using a photodetector. Figure 5(b) presents a detailed view of the built assembly. The path of light and fluids is transversal. From the bottom a thermally stabilized holder and from the top an apochromatic microscope objective. From the top, it is possible to inspect both the microfluidics channel and the scattered light when light is coupled to the device. The photonic cavity in Figure 5.3(c) corresponds with an MRR that is used to transduce the refractive index variations.

To demonstrate refractive index sensing in the built ensemble, a set of aqueous glucose solutions is prepared. The concentrations go from 10 to 50 mg/mL with steps of 10 mg/mL. The temperature of the holder was set to 24 +/- 0.002°C, as the one measured in the laboratory environment (~24°C), with an environmental humidity of ~56%. The measurements were performed at a constant flow of 70 µL/minute. At first, the spectral response of the MRR is registered, as presented in Figure 5.4(a). Here the reconstructed resonances in a window of 10 nm are presented for a glucose concentration of 10 mg/mL. Figure 5.4(a) presents in vertical red lines the position of the resonance feature (minimum)

used to reconstruct the wavelength shift produced by the different concentrations. The selected resonances and the corresponding wavelength shift are presented in Figure 5.4(b).

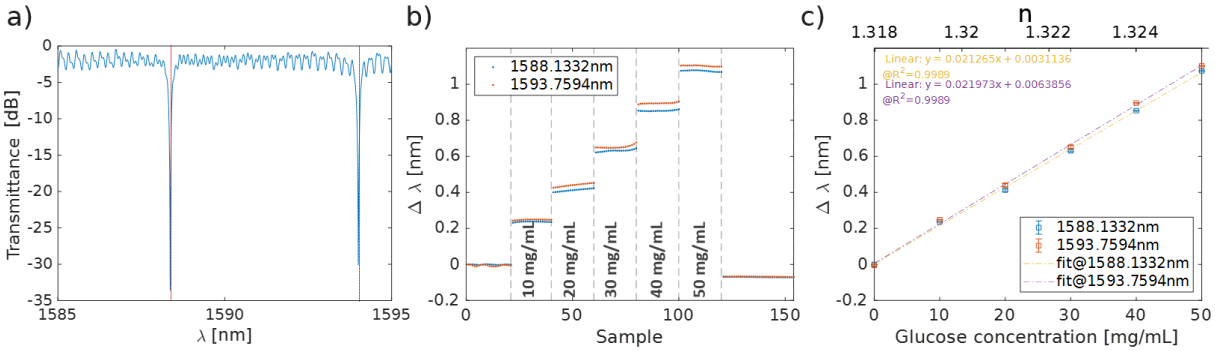

Figure 5.4 - (a) Transmittance of a sample MRR-PhCN with 10 mg/mL of Glucose flowing in the top. (b) The wavelength shift of the resonances in (a) under different concentrations from 10 to 50 mg/mL in increasing order and then flashed with water (c) Calibration curves associated with the experiments in (b).

A step-like function is shown in Figure 5.4(b) representing the evolution of the experiment for different concentrations and then back to the starting point (0% concentration). The wavelength shift is then translated into the calibration curve presented in Figure 5.4(c). Here, the concentrations are translated into refractive indexes based on [73]. The calculated sensitivities are ~138 nm/RIU and ~142nm/RIU, respectively. It may be concluded that a full demonstration of the system operation for the fabricated microfluidics has been achieved.

5.5. Summary & Perspective

An easy-to-go approach to implement microfluidic channels on top of a single etch Si_3N_4 photonic structure is demonstrated. The no need for extra fabrication steps makes them feasible for fast evaluation of refractive index sensors dealing with aqueous solutions. Refractive index sensing of glucose aqueous solutions in constant flow is demonstrated. Further development of the system will come through the assessment of the discussed photonic cavities in previous chapters, with intensity-based schemes suitable for PTS.

Complementary, 3D printing technology allows the customization of microfluidic systems (sub-10 µm features) for automated control of a MRR's resonance wavelength, including on-chip mixing [151]. Further improvements will be made by custom 3D printing technology to directly interface with silicon photonic devices [152]. This eliminates the need for the laborious fabrication and bonding of discrete layers, and it allows to use of the device volume in all three dimensions, facilitating highly integrated component placement and fluidic routing. Significantly, this technology allows for rapid device fabrication, typically requiring less than 15 minutes, and offers flexibility in modification and testing. Additionally, by adding gas analysis in the same platform is possible to realize a universal nanophotonic-microfluidic sensor [30]. Last, these advancements can be realized despite the type of nanostructure, as was previously demonstrated by the Microfluidic tuning of photonic crystals for spectral filtering [153].

Chapter 6 - Conclusions & Outlook

This chapter delves into the impact of the conducted research on the development of a lab-on-chip PTS sensor. It showcases advancements in the design and development of mid-infrared (MIR) metasurfaces for near-field enhancement, as well as ongoing efforts to optimize and expand the system to various applications. Finally, the thesis concludes with key remarks.

6.1. Outlook

In addition to the results discussed in the previous chapters, which aim to provide new integrated refractive index transducers, this section also explores resonance structures that can enhance the interaction of the target analyte with the pump beam in a PTS system.

6.1.1. MIR Metasurfaces (collaboration with Artem Vorobev and Giulia Malvicini)

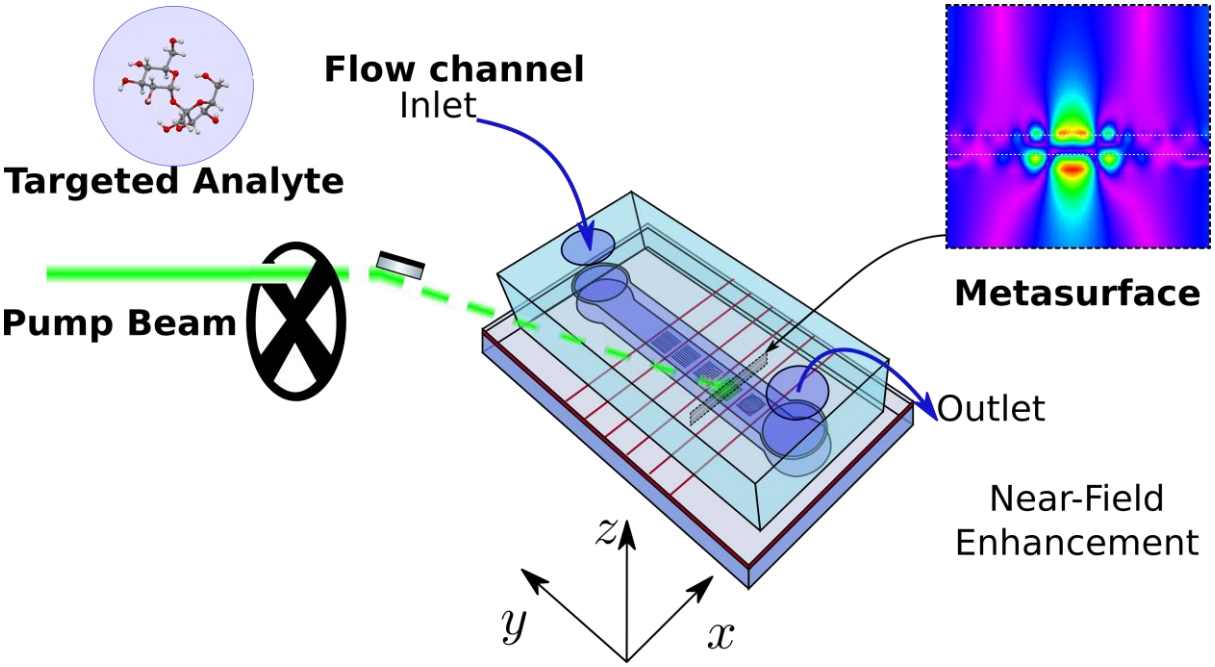

Figure 6.1 - Schematics representation of a MIR meta surface for near field enhancement.

Metasurfaces operating in the mid-infrared range exhibit significant potential as essential components for integrated sensing due to their capacity for achieving high sensitivity, precise compositional discrimination, and minimal energy dissipation [154]. Therefore, resonant dielectric metasurfaces, in the MIR region, can enhance infrared absorption, thus improving sensitivity. Moreover, the volume region where the near-field field enhancement occurs plays a central role in defining the detection limit for sensing applications. In contrast to other alternatives, photonic structures like dielectric metasurfaces have minimal energy losses and

offer high-Q factors, strong amplitude resonances, and near-field enhancement at the microscale [31]. This makes them ideal for studying analytes, such as those present in biological samples. Silicon metasurfaces in the mid-infrared range could be a better choice for detecting large molecules and bio-systems inside the body, and for use in microfluidic systems [154]. Figure 6.1 presents the corresponding schematic to illustrate the intended application as a standalone device, or as an extra degree of freedom for the improvement in the PTS signal. By interrogating the resonances present in the transmission or reflection spectrum, the metasurface can be used for refractive index sensing. On the other hand, near-field enhancement at the pump beam side in a PTS system can be considered.

6.1.1.2. Guided Mode Resonances

Dielectric gratings have the potential to achieve exceptional performance in sensing applications through the support of guided-mode resonances (GMRs) and bound states in the continuum (BICs). Both phenomena can lead to exceptionally high Q-factors and significant localized field enhancements [155]. These structures have been extensively investigated because of their practical implementation and versatile performance. By adjusting factors like the lattice constant, fill factor, thickness, angle of incidence, and permittivity, dielectric gratings with GMRs offer precise control over both the far-field light patterns and the distribution of light in their immediate vicinity [34].

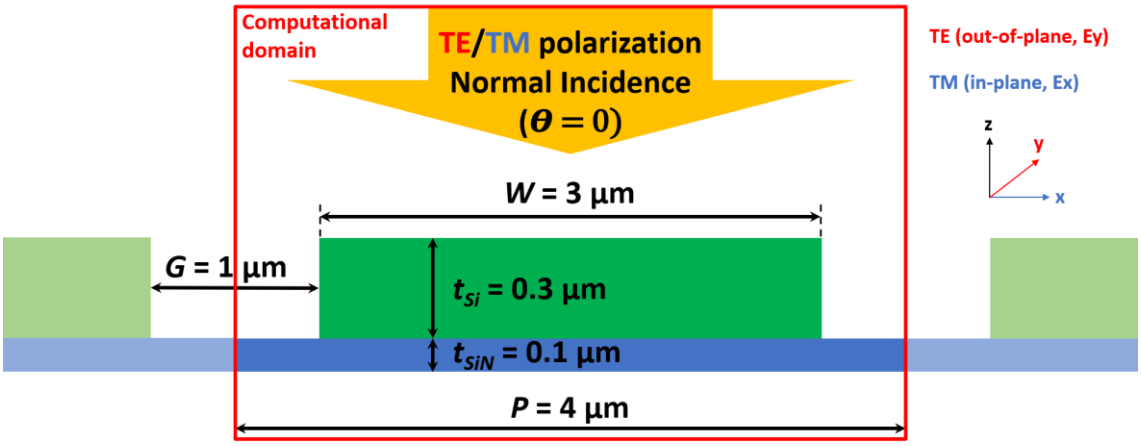

Figure 6.2 - Cross section of the proposed dielectric grating that supports GMR. Pattern Silicon with thickness t_{Si}, resting in a membrane of Silicon nitride with thickness t_{SiN}. The filling factor, FF, is defined by the product between the silicon width, W, and the lattice constant, P. The etched space, G, is therefore defined as P-W. Normal incidence (θ=0 with respect to the vertical) is considered.

Near-field enhancement is explored based on GMR employing the geometry presented in Figure 6.2. The 1D metasurface is composed of a symmetric silicon grating deposited in a Silicon Nitride membrane. The translational symmetry, of the structure allows the reduction of the computational domain to the unit cell, squared in red (see Figure 6.2). The resonant characteristics of the device are analyzed through Rigorous Coupled Wave Analysis (RCWA) ensuring the convergence [156]. RCWA is a technique that has been implemented using advanced algorithms including fast Fourier factorization and generalized transmission line formulation.

The response of the periodic waveguide in Figure 6.2 is analyzed either TE (out-of-plane, E_y) or TM (in-plane, E_x) at normal incidence (θ=0°). The calculated total transmission spectrum is shown in Figure 6.3 (a). Among the three Fano-like resonant features present in the spectrum the one at 4.18 µm, corresponds with the narrower resonance in the spectrum. The calculated steady-state field profile in the structure of the dominant electric component, E_x,

is presented in Figure 6.3 (b) and (c). Figure 6.3(b) corresponds with the spatial distribution of the electric field at the maximum of the resonance and Figure 6.3 (c) corresponds to the minimum. The calculated field distributions are in agreement with similar configurations presented in [155]. The overlap of the mode's spatial distribution on top of the structure ranges from 37% to 40%, so according to the perturbation theory, a high sensitivity may be expected. A different case is observed for TE polarization where the overlap between the electric field and the top of the grating is ~13%. Besides, the Q-factor of resonance at TM increases by a factor of 29 with respect to TE. Such an ability to enhance the Q-factor, and the spatial distribution of the mode, provides the current dielectric device with excellent capabilities for sensing.

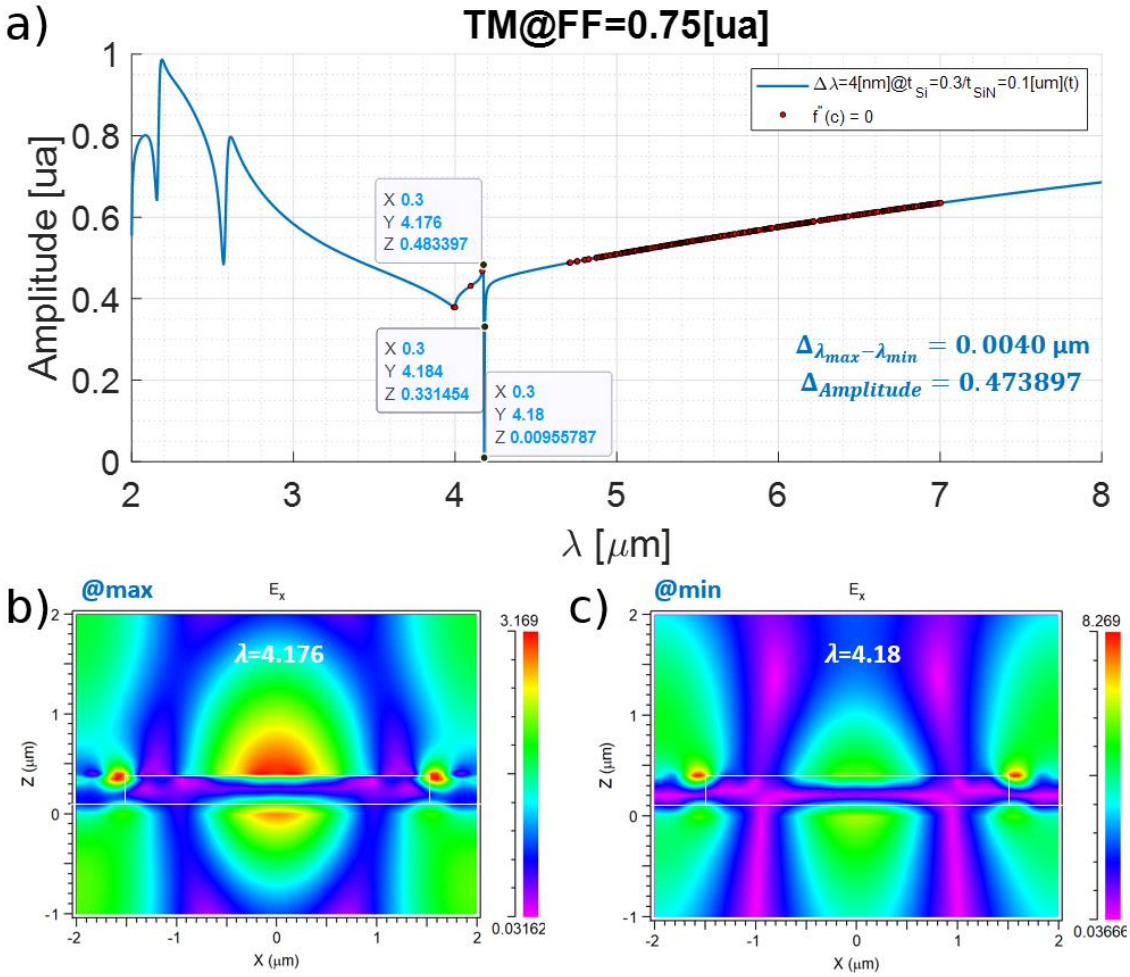

Figure 6.3 - (a) Calculated transmission of a dielectric grating with FF=0.75 at TM polarization. (b)Electric Field distribution, E_x, of the grating at a wavelength of the resonance at peak (@max). (c) Distribution of E_x in the 1D waveguide at the wavelength of the resonance dip (@min). The output fields are normalized to the input and given in arbitrary units.

Additional flexibility could be achieved by examining the reflection spectra, which exhibit similar characteristics as the transmission spectra. Extra data analysis was carried out to optimize the structures considering the fabrication constraints. The comparison is a matter of evaluation due to the fabrication to finalize. On the other hand, the generation of quasi-BIC resonances that hold ultra-high-Q, are being investigated by the introduction of asymmetry in the lattice constant of the binary grating under study, [155].

6.1.1.3. Fabrication

Inherently, the design proposed is challenging due to the tiny membrane of the Si_3N_4 where the patterned Si will rest. The first fabrication attempt began with a layered structure of Poly-Si-Si_3N_4-SiO_2-Si wafer. As the proposed structure required the fabrication of a membrane, the process was divided into two stages:

- Patterning the 1D metasurfaces design on the Poly-Si layer through photolithography and dry etching.
- Patterning the windows in the SiO_2-Si substrate using photolithography and dry etching.

The first iteration of the fabrication process is shown in Figure 6.4.

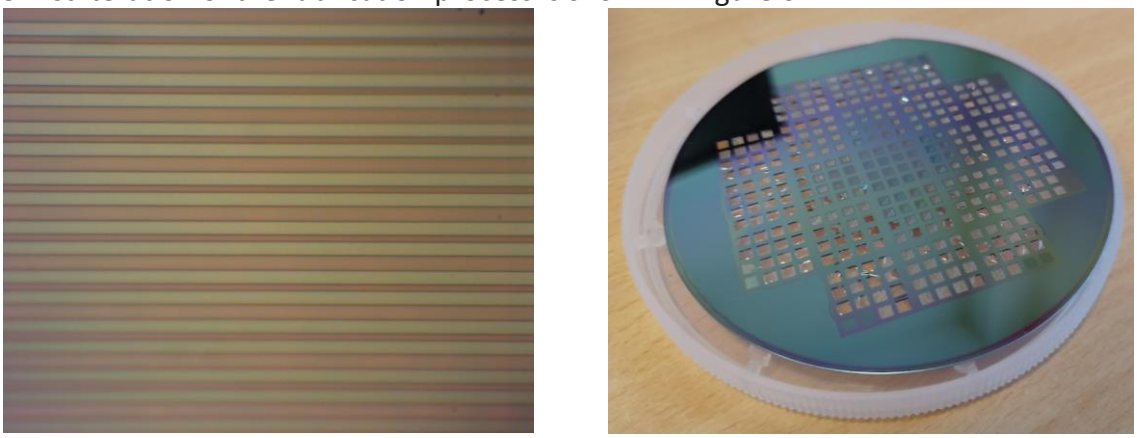

Figure 6.4 - (a) Microscopic image detail of one of the fabricated devices. (b) Fabricated wafer.

The challenges regarding the metasurface fabrication are under current investigation. The fragility of the metasurface's fine structure has been observed to be susceptible to alterations caused by pressure fluctuations within the fabrication chamber. An avenue for further exploration involves the cultivation and patterning of this structure on transparent substrates, such as Calcium Fluoride (CaF_2) or Barium Fluoride (BaF_2), which will be the subject of subsequent research.

6.1.2. Integration in a photothermal system (Collaboration with Giovanna Richiutti)

As a part of the collaborations established between members of the OPTAPHI consortium, the first attempt to realize PTS on the chip was successfully demonstrated by Giovanna Richiutti. A schematic representation of the conducted experiment is presented in Figure 6.5. The modulated pump beam is shined on top of the thin polymer layer that coats the Si_3N_4 chip. The generated refractive changes in the polymer, due to the pump beam photo-induced thermal transitions, were retrieved through a PhCN-MRR (chapter 4). Two sets of design layouts were provided to experiment with the facilities of Munster Technological University. Further collaboration is ongoing to extend this finding to the other photonic cavities discussed in this thesis. Besides, it is expected to move on to liquid and gas phase analytes. A manuscript with PTS on-a-chip for polymer analyte is in preparation.

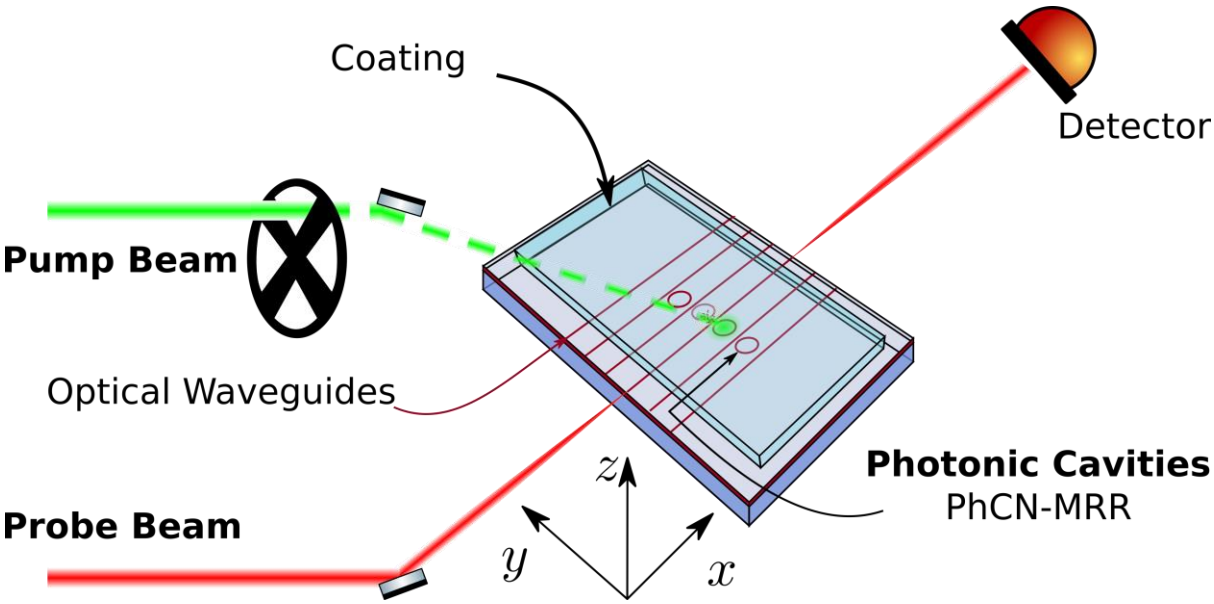

Figure 6.5 - First attempt PTS on -a-Chip using PhCN-MRR as a refractive index transducer.

6.1.3. Flow injection analysis and Fiber coupling

As demonstrated in Chapter 5, the current system at TU Wien allows the manipulation of reduced volume of aqueous solutions through microfluidics. Therefore, static and flow measurements of refractive index were demonstrated. In this sense, further effort is put into the realization of Flow Injection Analysis experiments with the tested refractive index transducers as a detector.

Flow Injection Analysis (FIA) is a widely used analytical technique that involves the manipulation of a sample zone within a well-designed flow network, ultimately leading to a flow-through detector. This method is characterized by several key attributes, which include rapid analysis, continuous flow, precise control (e.g., flow rates, injection volumes), sample segmentation, and reduced sample consumption among many others. The flow-through detector is a crucial component of FIA, as it continuously monitors the sample as it passes through. Besides, FIA can incorporate sample dilution and mixing steps within the flow network, ensuring that the sample is prepared appropriately for analysis. Depending on the detector type, it can measure various parameters, including absorbance, fluorescence, conductivity, or electrochemical signals. Therefore, the aim is to introduce photonic cavities as a detector in a FIA-like system. The photonic detector will transduce the refractive index changes in the dilutions flowing through it.

Moving towards this goal, further characterization of the intended detectors is being matter of the current study. The demonstrated operation of the microfluidic system moves us a step ahead. With the same goal, fiber coupling to the chip is being explored by either, grating couplers or butt-coupled fibers. Butt-coupled fibers are being bonded into the chip. This approach has been already tested to assess how the features are affected in this sense.

6.2. Conclusions

In conclusion, this research centered on the design, simulation, and experimental characterization of high Q-factor photonic cavities as an innovative refractive index transducer for photothermal spectroscopy. Several compact variations of Si_3N_4 Photonic Crystal Nanobeam cavities and Micro Ring Resonators, aiming to generate both symmetric

and asymmetric Fano resonances, are explored. The characterized response of the fabricated devices demonstrates their suitability for PTS applications. Furthermore, active sensing via HECL configuration, the concept of near-field enhancement through metasurfaces, and the integration of liquid cells by microfluidics are also explored. This comprehensive approach substantially narrows the gap toward realizing a photonic-integrated photothermal spectroscopy sensor.

The figure of merits exhibited by the angle-sided wall Photonic Crystal Nanocavity (PhCNC) has been demonstrated to be robust across various sensing scenarios, even in the presence of lower contrast linked with non-suspended configurations. Nevertheless, it is important within the scope of this investigation to highlight the potential for tailoring the optical properties of these devices in the context of asymmetric cladding arrangements, achieved through precise control of the etching angle. This factor presents itself as an additional and highly desirable degree of freedom to fine-tune the performance of cavity-based refractive index sensors. Furthermore, this investigation extends to the exploration of the Hybrid External Cavity Laser (HECL) configuration. This result opens a promising avenue to face the limitations that passive devices present for optical sensing.

Similarly, the elliptical nanopillar-based PhCNC presents a potential solution for mitigating the influence of the intrinsic inaccuracies observed in manufactured devices, all while preserving a high Q-factor. Conversely, the slotted PhCNC configuration featuring side wall angles introduces an additional mechanism to compensate for the drop in Q-factor. These valuable results will give insights into new geometries that can combine the individual advantages of the three explored PhCNCs.

As an alternative, a novel and compact Fano resonator based in a Si_3N_4 Photonic Crystal Nanobeam-assisted Micro Ring Resonator has been experimentally demonstrated. A high Q-Q-factor and a substantial Fano asymmetry parameter are achieved. Additionally, the steeper slopes of Fano resonance could give rise to further improvement in terms of analytical sensitivity when used in PTS. The two variations of this innovative structure have been designed, simulated, and experimentally characterized. Complementary, demonstration in different sensing scenarios confirms the flexibility of PhCN-MRR.

The observed drop in the Q-factor with an increment of the asymmetry, actually states an important point regarding the possibility of using the current device as a mechanism of steeper resonance linewidths. However, this issue could come from the leaky nature of the quasi-guided mode through the PhCN. Therefore, further experiments to examine the guided regimen of the propagating mode can certainly increase the Q-factor while the asymmetry increases.

Aiming of a miniaturized sensor, the microfluidic cell is bonded successfully onto Si_3N_4. The benefits of microfluidics were proven by measuring aqueous glucose solutions, demonstrating the operability of the implemented liquid handling. This opens the door for further testing of the proposed transducers in applications like liquid chromatography or flow injection analysis.

On the other hand, metasurfaces for near-field enhancement applications can be suitable to boost the interaction of the excitation (pump) laser with the sample, optimizing the performance of a PTS system. Besides, it comes itself as a potential refractive index sensor.

In summary, the study presented in this Ph.D. thesis offers valuable insights for the design, simulation, and experimental characterization of resonant structures that can be integrated into PTS systems, but not limited to these. Additionally, several approaches to facing different constraints of a PTS system have been explored. The presented work paves the way for further advancements in this exciting area of research that combines multiple disciplines.

APPENDIX A– COMPUTATIONAL PHOTONICS

This appendix presents some general points about the simulations conducted and the characteristics of the software used.

A.1 FDTD

FDTD was originally named Yee's method after Kane S. Yee, who introduced the formalism in 1966 [157]. Extensive study and development by Allen Taflov and others from 1974 through the early 21st century, was conducted. Since its inception, FDTD techniques have become widely employed to address various electromagnetic challenges in both research and industry. Presently, FDTD is extensively utilized in nanophotonics.

FDTD is a computational method that resolves Maxwell's equations by discretizing a specific volume of interest in both time and space. This discretization is always tied to a designated grid where the electromagnetic field is reconstructed (Yee grid). For complete formalism of the method, the reader can refer to [158]. The last chapter of this book also introduces the FDTD solver described in the following subsection.

A.2 Meep

Meep, an open-source Python package, is utilized for conducting FDTD (Finite-Difference Time-Domain) calculations. Its initial development dates back to 2009 at the Massachusetts Institute of Technology [82], where it was originally coded in C++ and integrated with Scheme [159]. In 2017, a Python version of Meep was introduced. Leveraging the FDTD method, Meep offers a versatile platform for tackling various electromagnetic challenges, including photonic Crystal cavities and metasurface design.

A Meep script typically involves several key steps:

- Environment definition, which encompasses settings like resolution, grid volume, materials, and boundary conditions.
- Geometry definition allows for the specification of structures and substrates.
- Incident field definition, addressing field type, wavelengths, direction, polarization, and related parameters.
- Simulation parameter definition, including the simulation duration (time units).
- Execution of the simulation.
- Extraction of desired physical quantities from the compiled simulation results, such as electric and magnetic fields and refractive indexes."

Apart from its efficiency, the open-source nature of Meep is a valuable attribute. Furthermore, it benefits from a highly engaged community, always prepared to offer assistance for any issues that may arise. This is also advantageous to perform simulations in

High-performance computing infrastructures. Some of the results presented in this document received support from CINECA, Italy with ISCRA C projects: ASTREA, METAFORE, and trymendoza23 with available computing hours in the Galileo (earlier version), Marconi, and g100 clusters.

A.2.1 Time-domain Simulation

A time-domain electromagnetic simulation essentially involves the evolution of Maxwell's equations over time within a finite computational volume, effectively serving as a numerical experiment [82]. This method allows for the calculation of a diverse range of valuable parameters. Some of the key applications include:

- *Transmittance and Reflectance Spectra:* Through Fourier-transforming the response to a short pulse, a single simulation can provide scattering amplitudes across a broad spectrum, offering insights into how electromagnetic waves propagate through a given medium.
- *Resonant Modes and Frequencies:* By analyzing the system's response to a short pulse, it is possible to extract information about the frequencies, decay rates, and field patterns of harmonic modes in both lossy and lossless systems. This extends to systems like waveguides and cavity modes, shedding light on their behavior.
- *Field Patterns* (e.g., Green's Functions): The simulation can elucidate field patterns in response to arbitrary sources through continuous-wave (CW) inputs at a fixed frequency (ω). This is instrumental in understanding how electromagnetic fields interact with various structures and sources.

A.2.2 Convergence Test

FDTD simulations presented in this document were subject to convergence test verification. Resonant structures that support high-quality factors (like the ones in Chapter 3) are susceptible to variabilities in the computational domains that could reduce the accuracy of the results. Regarding the resolution of the simulations, harmonic Inversion of Time Signals by the Filter Diagonalization Method (FDM) [160] was used to extract the frequency and the Q-factor of the optical resonance modes in the proposed Photonic Crystal Cavities. The field components in the optical cavity can be described with a discrete, finite-length time series $f(t)$, that consists of a sum of finitely-many sinusoids (possibly exponentially decaying), within the specified bandwidth as:

$$f(t) = \sum_{n} a_n \, e^{-jw_n t} \tag{A.1}$$

where, the method aims to determine the frequency, decay constants, amplitudes, and phases of the sinusoids. It is important to stress that this method can give good results even when: the recording time is reduced, there are several oscillators in a noisy signal, and weak signals are superposed on top of much stronger signals of similar frequency [82]. Therefore, in the case of the PhCNC, a validation of the computational model was conducted on a symmetric refractive index configuration, in this case, the upper cladding refractive index was equal to the substrate (n_s=n_{upp}), Figure A1 shows the influence of the time series length on the Q-factor and the resonant frequency.

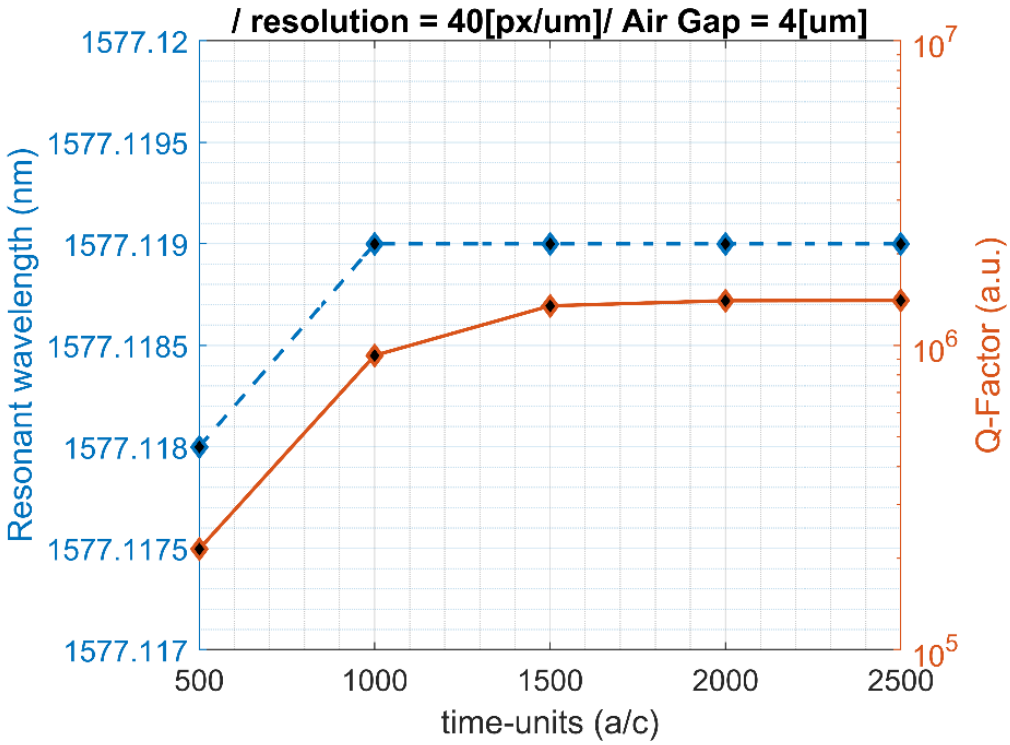

Figure A1. Resonant wavelength and Q-Factor against the time units considered to validate the computational model of the proposed PhCNC for fixed resolution of 40[px/µm], Air Gap of 4µm, perfectly matched layer, PML=1µm. The time-units region used in the simulations (>2000 a/c), in which the Q-factor has converged. a, periodicity, and c speed of light.

Naturally, the increment in the time units used for the calculation impacts the stability of the calculated Q-Factor and resonant frequency (blue dashed curve in Figure A1), showing that at least 2000 time units are needed. Besides, longer time series will improve the frequency resolution of the corresponding spectra. In all simulations, t=2500 (TBC) was used. Besides, a similar analysis was performed on the spatial resolution of the computational domain. Hence, a grid resolution of 40 pixels/µm (spatial step of 25nm) was set to confluent into a stable calculation.

A.2 MPB

Two common computational electromagnetic approaches for studying dielectric structures are the frequency-domain and time-domain methods. In the previous section, a time domain method was introduced. Each method holds a distinct place in a photonic designer's toolkit, each offering its own set of advantages and disadvantages.

MPB operates in the frequency domain. This means that the eigenstates and eigenvalues of Maxwell's equations using a plane-wave basis, are directly computed. In this approach, each computed field corresponds to a specific frequency. In contrast, time-domain techniques, such as those used in Meep software, iterate Maxwell's equations over time. Consequently, the computed fields have a definite time at each time step but not a single, well-defined frequency.

In the context of frequency-domain eigenproblems, the objective is to determine the band structure, denoted as $\omega(k)$, and the corresponding fields associated with it. This is achieved by formulating the problem as a finite matrix eigenproblem, where $Ax=\omega^2 Bx$, and employing linear algebra techniques to compute a selection of eigenvectors (x) and their corresponding

eigenvalues (ω^2). This approach allows for the systematic investigation of how different frequencies (ω) are related to specific wave vectors (k) and how these relate to the material's properties, offering valuable insights into the behavior of electromagnetic waves within dielectric structures [36].

APPENDIX B – 1D PHOTONIC BAND GAP IN 1D PHOTONIC CRYSTAL

This appendix aims to add more details into the formation of the photonic band gap into a one-dimensional photonic crystal. The content is presented based on [161].

The formation of the photonic band gap can be attributed directly to the phenomenon of destructive interference arising from multiple reflections of light as it traverses the photonic crystal (PhC) and interacts with the interfaces between regions of differing dielectric constants. The periodic perturbation introduced into the electromagnetic field within the material, resulting from the modulation of the refractive index, which is closely associated with the dielectric constant, leads to the formation of Floquet-Bloch waves. These waves act as carriers of optical energy distribution within the photonic crystal [36].

A one-dimensional photonic crystal can be effectively represented as a homogeneous medium in the x and y dimensions while exhibiting a periodic modulation of the dielectric function along the z-axis. This modulation is described by $\varepsilon(z) = \varepsilon(z + \kappa a)$, where a signifies the periodicity, and κ takes on integer values such as κ = …, -1, 0, 1, 2, ..., as visualized in Figure B.1(a). Here, an electromagnetic (EM) wave propagating exclusively along the direction of the permittivity modulation within the medium (the z-axis), is considered. Consequently, the wave vector components in the x and y dimensions become null, in contrast to the component along the z-axis, denoted as $\vec{k}$ for the sake of simplicity.

The periodic physical characteristics of the material allow us to treat the propagating wave within the multilayer film mathematically as Bloch waves, by Bloch's theorem [36].

$$E_k(z) = e^{-ikz} u_k(z) \tag{B.1}$$

where $u_k(z)$ corresponds to the periodic envelope function with the same periodicity as the one for the periodic dielectric function of the medium. $u_k(z)$ can be expressed in the Fourier series as:

$$u_k(z) = \sum_{n=-\infty}^{\infty} E_n e^{inGz} \tag{B.2}$$

This result stems from the inherent periodic nature of the function, which takes the form $u(z) = u(z + \kappa a)$, where κ is an integer. In the context of Equation B.2, $G = 2\pi/a$ represents the lattice vector. By substituting k with $k + 2\pi/a$ in Equation B.1, the following expression is obtained:

$$E_{k+\frac{2\pi}{a}}(z) = e^{-ikz}\left(e^{-\frac{i2\pi z}{a}} u_{k+\frac{2\pi}{a}}(z)\right) \tag{B.3}$$

the enclosed term within the brackets is also subject to periodicity, resulting in k being a periodic function with a period of $2\pi/a$. Consequently, k' can be represented as $k + 2m\pi/a$, where m is an integer (m = ..., -1, 0, 1, 2, ...).

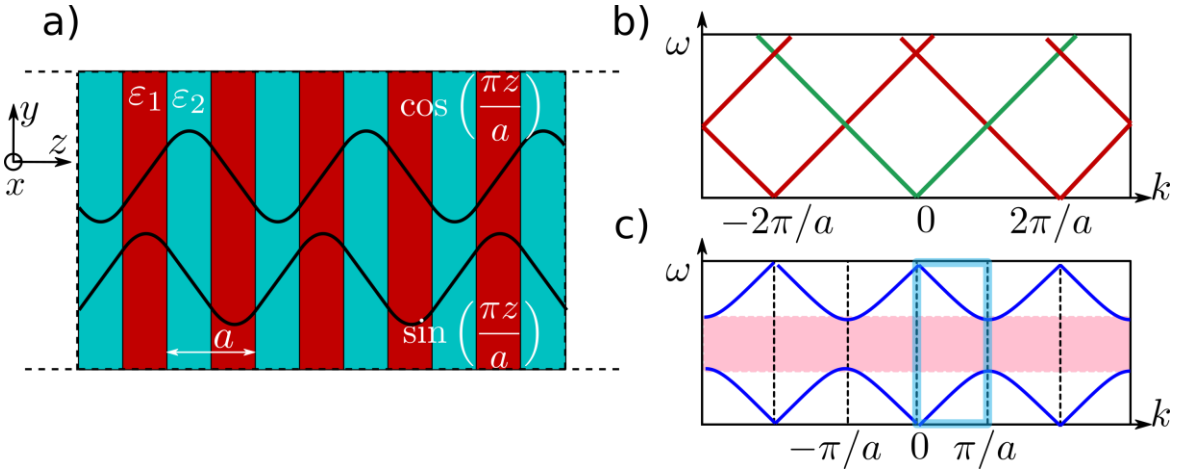

Figure B.1 (a) This diagram depicts a material with one-dimensional periodicity along the z-direction. The regions with high dielectric constants (ε_1) are highlighted in dark red, while the low dielectric constant regions (ε_2) are represented in dark blue. The black curves illustrate the two possible modes distributions at $k = \pm\pi/a$. The mode with a lower frequency, denoted as ω_{low}, tends to concentrate its energy in the high dielectric constant regions (ε_1), while the mode at a higher frequency, ω_{high}, tends to distribute its energy in the low dielectric constant regions (ε_2). (b) In this diagram, the dispersion relation, $\omega(k)$ corresponds to the propagation of light along the z-direction in a homogeneous medium, indicated by the dark green lines. The presence of arbitrary periodic characteristics generates a periodic repetition of the dispersion curves at $k' = k + 2\pi/a$ indicated with dark red lines. (c) The dispersion relation in this diagram represents the propagation of light along the z-direction in a medium that is periodic along the z-axis. A photonic bandgap (depicted by the dark pink rectangle) is formed due to the splitting of the degeneracy of the modes at $k = \pm\pi/a$. The irreducible Brillouin zone is delineated by the light blue rectangle. Adapted from [161].

In the case of a homogeneous medium characterized by a dielectric constant ε, synthetically modulated with a period a, the dispersion relation (band structure) takes on a straightforward form $\omega(k) = ck/\sqrt{\varepsilon}$ (light line) as depicted in Figure B.1(b). This relation repeats for each k', where $k' = k + 2m\pi/a$ (illustrated by dashed lines). Despite the homogeneity of the medium, one can effectively treat each k' as equivalent to k. Further simplification arises from symmetry considerations, as all the relevant information regarding the dispersion can be found within the quasi-periodic region $-\pi a < k < \pi a$, referred to as the Brillouin zone. Within this zone, the region $0 < k < \pi a$ defines the Irreducible Brillouin zone.

Therefore, the existence of two modes within the medium, characterized by a frequency $\omega = c\pi/a$, described by $e^{\pm i\pi z/a}$, is observed. These modes are described by $f(z) = \cos(\pi z/a)$ and by $g(z) = \sin(\pi z/a)$, which correspond to standing-wave solutions of the wave equation in a periodic medium, as shown in Figure B.1(a). The homogeneity of the dielectric properties of the medium leads to degeneracy between these two modes, meaning they share the same frequency.

Nevertheless, the degeneracy between these modes can be disrupted through a perturbation of the dielectric constant within the multilayer medium with periodicity a, expressed as $\varepsilon(z) = 1 + \Delta cos(2\pi z/a)$. This perturbation implies that the same structure can accommodate two different wavelengths of light at the same k-vector. As a result, these modes correspond to two distinct frequencies, denoted as ω_{high} and ω_{low}, with $\omega_{high} > \omega_{low}$.

However, due to the translation symmetry associated with periodicity, the accommodation of these modes is limited to two specific scenarios. As illustrated in Figure B.1(a), the low-frequency modes tend to concentrate their energy in the high-ε region (high-index material), while the high-frequency modes localize a larger portion of their energy in the low-ε region (low-index). This spatial distribution of energy results in the emergence of a finite range of frequencies for which the energy distribution is prohibited (k_z possesses a non-zero imaginary part), and modes cannot propagate in the periodic medium (Figure B.1(c)).

Mathematically, this phenomenon is described by solving the Hamiltonian form of Maxwell's equations in the presence of a periodic potential, leading to the identification of the forbidden-frequency range known as the photonic bandgap. This term draws an analogy with the electronic bandgap in semiconductors, originating from solutions of Schrödinger's equation in a periodic potential. Practically, light at frequencies falling within the photonic bandgap is reflected by the 1D periodic materials, often referred to as Bragg reflectors, as their reflective properties are influenced by the Bragg effect. The width of the photonic bandgap, denoted as $\Delta\omega$, increases with the dielectric constant (refractive index) contrast $\Delta\varepsilon$ between the two distinct repeating layers of the medium.

The $\omega(k)$ dispersion relation of photonic crystal structures is commonly referred to as the band diagram (band structure). This diagram characterizes the crystals in k-space, which is the spatial Fourier transform of the real space lattice of the crystal. It serves as a crucial tool for classifying the properties of photonic crystals. The higher-order repetitions of the dispersion curve in the band diagram can be visualized as the curve of the first zone being folded back into the zone at the edge. Consequently, it is evident that the irreducible Brillouin zone, mentioned earlier in the paragraph, is sufficient to describe the properties of any reciprocal periodic medium [161].

REFERENCES

[1] S. Iadanza, J.H. Mendoza-Castro, T. Oliveira, S.M. Butler, A. Tedesco, G. Giannino, B. Lendl, M. Grande, L. O'Faolain, High-Q asymmetrically cladded silicon nitride 1D photonic crystals cavities and hybrid external cavity lasers for sensing in air and liquids, Nanophotonics. 11 (2022) 4183–4196. https://doi.org/10.1515/nanoph-2022-0245.

[2] T. Oliveira, S. Iadanza, J.H. Mendoza-Castro, M. Grande, L. O'Faolain, Silicon Nitride 1D Photonic Crystal Cavity Hybrid Laser for Refractive Index Sensing in Liquid and Gaseous Media, in: 2023 Conference on Lasers and Electro-Optics Europe & European Quantum Electronics Conference (CLEO/Europe-EQEC), 2023: pp. 1–1. https://doi.org/10.1109/CLEO/Europe-EQEC57999.2023.10231533.

[3] J.H. Mendoza-Castro, A.S. Vorobev, S. Iadanza, B. Lendl, M. Grande, L. O'Faolain, Fano Resonances in a Photonic Crystal Side-Coupled Micro Ring Resonator for Refractive Index Sensing, in: 2023 Conference on Lasers and Electro-Optics Europe & European Quantum Electronics Conference (CLEO/Europe-EQEC), IEEE, Munich, Germany, 2023: pp. 1–1. https://doi.org/10.1109/CLEO/Europe-EQEC57999.2023.10231647.

[4] J.H. Mendoza-Castro, A.S. Vorobev, S. Iadanza, B. Lendl, M. Grande, L. O'Faolain, Q-Factor Optimization in Photonic Crystal Nanobeam Cavities Based on Elliptical Nanopillars for Refractive Index Sensing, in: 2023 Conference on Lasers and Electro-Optics Europe & European Quantum Electronics Conference (CLEO/Europe-EQEC), IEEE, Munich, Germany, 2023: pp. 1–1. https://doi.org/10.1109/CLEO/Europe-EQEC57999.2023.10232053.

[5] A.S. Vorobev, J.H. Mendoza-Castro, S. Iadanza, B. Lendl, M. Grande, L. O'Faolain, Enable Fano resonances lineshapes in a Silicon Nitride Photonic Crystal-MicroRing structure, in: 2023 IEEE Silicon Photonics Conference (SiPhotonics), IEEE, Washington, DC, USA, 2023: pp. 1–2. https://doi.org/10.1109/SiPhotonics55903.2023.10141919.

[6] J.H. Mendoza-Castro, A.S. Vorobev, S. Iadanza, T. Oliveira, B. Lendl, L. O'Faolain, M. Grande, Compact side-coupled Silicon Nitride Photonic Crystal Nanobeam Cavity for refractive index sensing, in: 2023 IEEE Silicon Photonics Conference (SiPhotonics), IEEE, Washington, DC, USA, 2023: pp. 1–2. https://doi.org/10.1109/SiPhotonics55903.2023.10141917.

[7] J.H. Mendoza-Castro, L. O'Faolain, M. Grande, Q-factor enhancement in photonic crystal cavities based on trapezoidal slotted nano-sticks for refractive index sensing, in: 2021 Conference on Lasers and Electro-Optics Europe & European Quantum Electronics Conference (CLEO/Europe-EQEC), 2021: pp. 1–1. https://doi.org/10.1109/CLEO/Europe-EQEC52157.2021.9542649.

[8] A. Fathy, Y.M. Sabry, I.W. Hunter, D. Khalil, T. Bourouina, Direct Absorption and Photoacoustic Spectroscopy for Gas Sensing and Analysis: A Critical Review, Laser & Photonics Reviews. 16 (2022) 2100556. https://doi.org/10.1002/lpor.202100556.

[9] J.P. Waclawek, C. Kristament, H. Moser, B. Lendl, Balanced-detection interferometric cavity-assisted photothermal spectroscopy, Opt. Express, OE. 27 (2019) 12183–12195. https://doi.org/10.1364/OE.27.012183.

[10] J.P. Waclawek, V.C. Bauer, H. Moser, B. Lendl, 2f-wavelength modulation Fabry-Perot photothermal interferometry, Opt. Express, OE. 24 (2016) 28958–28967. https://doi.org/10.1364/OE.24.028958.

[11] Introduction, in: Photothermal Spectroscopy Methods, John Wiley & Sons, Ltd, 2019: pp. 1–56. https://doi.org/10.1002/9781119279105.ch1.

[12] M. Soler, M.C. Estevez, M. Cardenosa-Rubio, A. Astua, L.M. Lechuga, How Nanophotonic Label-Free Biosensors Can Contribute to Rapid and Massive Diagnostics of Respiratory Virus Infections: COVID-19 Case, ACS Sens. 5 (2020) 2663–2678. https://doi.org/10.1021/acssensors.0c01180.

[13] M.A. Butt, N.L. Kazanskiy, S.N. Khonina, G.S. Voronkov, E.P. Grakhova, R.V. Kutluyarov, A Review on Photonic Sensing Technologies: Status and Outlook, Biosensors. 13 (2023) 568. https://doi.org/10.3390/bios13050568.

[14] N.L. Kazanskiy, S.N. Khonina, M.A. Butt, A Review of Photonic Sensors Based on Ring Resonator Structures: Three Widely Used Platforms and Implications of Sensing Applications, Micromachines. 14 (2023) 1080. https://doi.org/10.3390/mi14051080.

[15] D.-Q. Yang, B. Duan, X. Liu, A.-Q. Wang, X.-G. Li, Y.-F. Ji, Photonic Crystal Nanobeam Cavities for Nanoscale Optical Sensing: A Review, Micromachines. 11 (2020) 72. https://doi.org/10.3390/mi11010072.

[16] Project 1.3 – OPTAPHI, (n.d.). https://www.optaphi.eu/projects/project-1-3/ (accessed November 5, 2023).

[17] Project 3.2 – OPTAPHI, (n.d.). https://www.optaphi.eu/projects/project-3-2/ (accessed November 5, 2023).

[18] Project 3.3 – OPTAPHI, (n.d.). https://www.optaphi.eu/projects/project-3-3/ (accessed November 5, 2023).

[19] S. Hassan, C.C. Schreib, X. Zhao, G. Duret, D.S. Roman, V. Nair, T. Cohen-Karni, O. Veiseh, J.T. Robinson, Real-Time In Vivo Sensing of Nitric Oxide Using Photonic Microring Resonators, ACS Sens. 7 (2022) 2253–2261. https://doi.org/10.1021/acssensors.2c00756.

[20] Y. Chen, W.S. Fegadolli, W.M. Jones, A. Scherer, M. Li, Ultrasensitive Gas-Phase Chemical Sensing Based on Functionalized Photonic Crystal Nanobeam Cavities, ACS Nano. 8 (2014) 522–527. https://doi.org/10.1021/nn4050547.

[21] A. Tittl, A. Leitis, M. Liu, F. Yesilkoy, D.-Y. Choi, D.N. Neshev, Y.S. Kivshar, H. Altug, Imaging-based molecular barcoding with pixelated dielectric metasurfaces, Science. 360 (2018) 1105–1109. https://doi.org/10.1126/science.aas9768.

[22] D.J. Blumenthal, R. Heideman, D. Geuzebroek, A. Leinse, C. Roeloffzen, Silicon Nitride in Silicon Photonics, Proceedings of the IEEE. 106 (2018) 2209–2231. https://doi.org/10.1109/JPROC.2018.2861576.

[23] Q. Qiao, J. Xia, C. Lee, G. Zhou, Applications of Photonic Crystal Nanobeam Cavities for Sensing, Micromachines. 9 (2018) 541. https://doi.org/10.3390/mi9110541.

[24] M.W. Puckett, K. Liu, N. Chauhan, Q. Zhao, N. Jin, H. Cheng, J. Wu, R.O. Behunin, P.T. Rakich, K.D. Nelson, D.J. Blumenthal, 422 Million intrinsic quality factor planar integrated all-waveguide resonator with sub-MHz linewidth, Nat Commun. 12 (2021) 934. https://doi.org/10.1038/s41467-021-21205-4.

[25] C. Wei, J. Li, Q. Jia, D. Li, J. Liu, Ultrahigh-Q lithium niobate microring resonator with multimode waveguide, Opt. Lett., OL. 48 (2023) 2465–2467. https://doi.org/10.1364/OL.489387.

[26] A. Vasiliev, A. Malik, M. Muneeb, B. Kuyken, R. Baets, G. Roelkens, On-Chip Mid-Infrared Photothermal Spectroscopy Using Suspended Silicon-on-Insulator Microring Resonators, ACS Sens. 1 (2016) 1301–1307. https://doi.org/10.1021/acssensors.6b00428.

[27] Y. Ota, R. Katsumi, K. Watanabe, S. Iwamoto, Y. Arakawa, Topological photonic crystal nanocavity laser, Commun Phys. 1 (2018) 1–8. https://doi.org/10.1038/s42005-018-0083-7.

[28] L. Gu, B. Wang, Q. Yuan, L. Fang, Q. Zhao, X. Gan, J. Zhao, Fano resonance from a one-dimensional topological photonic crystal, APL Photonics. 6 (2021) 086105. https://doi.org/10.1063/5.0060007.

[29] M. Scherrer, S. Kim, H. Choi, C.-W. Lee, K. Moselund, Topological lasing from embedded III-V 1D photonic crystal lattices in the telecom O-band, in: Active Photonic Platforms XIII, SPIE, 2021: pp. 9–13. https://doi.org/10.1117/12.2594421.

[30] A. Kuzin, V. Chernyshev, V. Kovalyuk, P. An, A. Golikov, R. Ozhegov, D. Gorin, N. Gippius, G. Goltsman, Hybrid nanophotonic–microfluidic sensor for highly sensitive liquid and gas analyses, Opt. Lett., OL. 47 (2022) 2358–2361. https://doi.org/10.1364/OL.457309.

[31] S. Kharratian, D. Conteduca, B. Procacci, D.J. Shaw, N.T. Hunt, T.F. Krauss, Metasurface-enhanced mid-infrared spectroscopy in the liquid phase, Chem. Sci. 13 (2022) 12858–12864. https://doi.org/10.1039/D2SC03927C.

[32] P. Tonkaev, Y. Kivshar, All-dielectric resonant metaphotonics: opinion, Opt. Mater. Express, OME. 12 (2022) 2879–2885. https://doi.org/10.1364/OME.467655.

[33] K. Koshelev, S. Kruk, E. Melik-Gaykazyan, J.-H. Choi, A. Bogdanov, H.-G. Park, Y. Kivshar, Subwavelength dielectric resonators for nonlinear nanophotonics, Science. 367 (2020) 288–292. https://doi.org/10.1126/science.aaz3985.

[34] K. Koshelev, Y. Kivshar, Dielectric Resonant Metaphotonics, ACS Photonics. 8 (2021) 102–112. https://doi.org/10.1021/acsphotonics.0c01315.

[35] F. Yesilkoy, E.R. Arvelo, Y. Jahani, M. Liu, A. Tittl, V. Cevher, Y. Kivshar, H. Altug, Ultrasensitive hyperspectral imaging and biodetection enabled by dielectric metasurfaces, Nat. Photonics. 13 (2019) 390–396. https://doi.org/10.1038/s41566-019-0394-6.

[36] J.D. Joannopoulos, ed., Photonic crystals: molding the flow of light, 2nd ed, Princeton University Press, Princeton, 2008.

[37] E. Yablonovitch, T. Gmitter, K. Leung, Photonic band structure: The face-centered-cubic case employing nonspherical atoms, Phys. Rev. Lett. 67 (1991) 2295–2298. https://doi.org/10.1103/PhysRevLett.67.2295.

[38] S. John, Strong localization of photons in certain disordered dielectric superlattices, Phys. Rev. Lett. 58 (1987) 2486–2489. https://doi.org/10.1103/PhysRevLett.58.2486.

[39] T. Asano, S. Noda, Photonic Crystal Devices in Silicon Photonics, Proceedings of the IEEE. 106 (2018) 2183–2195. https://doi.org/10.1109/JPROC.2018.2853197.

[40] J.S. Foresi, P.R. Villeneuve, J. Ferrera, E.R. Thoen, G. Steinmeyer, S. Fan, J.D. Joannopoulos, L.C. Kimerling, H.I. Smith, E.P. Ippen, Photonic-bandgap microcavities in optical waveguides, Nature. 390 (1997) 143–145. https://doi.org/10.1038/36514.

[41] J. Olthaus, P.P.J. Schrinner, D.E. Reiter, C. Schuck, Optimal Photonic Crystal Cavities for Coupling Nanoemitters to Photonic Integrated Circuits, Advanced Quantum Technologies. 3 (2020) 1900084. https://doi.org/10.1002/qute.201900084.

[42] M. Gehl, R. Gibson, J. Hendrickson, A. Homyk, A. Säynätjoki, T. Alasaarela, L. Karvonen, A. Tervonen, S. Honkanen, S. Zandbergen, B.C. Richards, J.D. Olitzky, A. Scherer, G. Khitrova, H.M. Gibbs, J.-Y. Kim, Y.-H. Lee, Effect of atomic layer deposition on the quality factor of silicon nanobeam cavities, J. Opt. Soc. Am. B, JOSAB. 29 (2012) A55–A59. https://doi.org/10.1364/JOSAB.29.000A55.

[43] Y. Akahane, T. Asano, B.-S. Song, S. Noda, High-Q photonic nanocavity in a two-dimensional photonic crystal, Nature. 425 (2003) 944–947. https://doi.org/10.1038/nature02063.

[44] M. Saldutti, M. Xiong, E. Dimopoulos, Y. Yu, M. Gioannini, J. Mørk, Modal Properties of Photonic Crystal Cavities and Applications to Lasers, Nanomaterials. 11 (2021) 3030. https://doi.org/10.3390/nano11113030.

[45] J. Hendrickson, A. Homyk, A. Scherer, T. Alasaarela, A. Säynätjoki, S. Honkanen, B.C. Richards, J.-Y. Kim, Y.-H. Lee, R. Gibson, M. Gehl, J.D. Olitzky, S. Zandbergen, H.M. Gibbs, G. Khitrova, 13 - One-dimensional photonic crystal nanobeam cavities, in: F. Jahnke (Ed.), Quantum Optics with Semiconductor Nanostructures, Woodhead Publishing, 2012: pp. 421–446. https://doi.org/10.1533/9780857096395.4.421.

[46] Y. Zhang, M.W. McCutcheon, I.B. Burgess, M. Loncar, Ultra-high-*Q* TE/TM dual-polarized photonic crystal nanocavities, Opt. Lett., OL. 34 (2009) 2694–2696. https://doi.org/10.1364/OL.34.002694.

[47] E. Kuramochi, H. Taniyama, T. Tanabe, K. Kawasaki, Y.-G. Roh, M. Notomi, Ultrahigh-Q one-dimensional photonic crystal nanocavities with modulated mode-gap barriers on SiO_2 claddings and on air claddings, Opt. Express, OE. 18 (2010) 15859–15869. https://doi.org/10.1364/OE.18.015859.

[48] Q. Quan, M. Loncar, Deterministic design of wavelength scale, ultra-high Q photonic crystal nanobeam cavities, Opt. Express, OE. 19 (2011) 18529–18542. https://doi.org/10.1364/OE.19.018529.

[49] Q. Quan, P.B. Deotare, M. Loncar, Photonic crystal nanobeam cavity strongly coupled to the feeding waveguide, Applied Physics Letters. 96 (2010) 203102. https://doi.org/10.1063/1.3429125.

[50] M.W. McCutcheon, M. Lončar, Design of a silicon nitride photonic crystal nanocavity with a Quality factor of one million for coupling to a diamond nanocrystal, Opt. Express, OE. 16 (2008) 19136–19145. https://doi.org/10.1364/OE.16.019136.

[51] C. Sauvan, G. Lecamp, P. Lalanne, J.P. Hugonin, Modal-reflectivity enhancement by geometry tuning in Photonic Crystal microcavities, Opt. Express, OE. 13 (2005) 245–255. https://doi.org/10.1364/OPEX.13.000245.

[52] S. Hu, S.M. Weiss, Design of Photonic Crystal Cavities for Extreme Light Concentration, ACS Photonics. 3 (2016) 1647–1653. https://doi.org/10.1021/acsphotonics.6b00219.

[53] G. Magno, A. Ecarnot, C. Pin, V. Yam, P. Gogol, R. Mégy, B. Cluzel, B. Dagens, Integrated plasmonic nanotweezers for nanoparticle manipulation, Opt. Lett., OL. 41 (2016) 3679–3682. https://doi.org/10.1364/OL.41.003679.

[54] Q. Quan, D.L. Floyd, I.B. Burgess, P.B. Deotare, I.W. Frank, S.K.Y. Tang, R. Ilic, M. Loncar, Single particle detection in CMOS compatible photonic crystal nanobeam cavities, Opt. Express, OE. 21 (2013) 32225–32233. https://doi.org/10.1364/OE.21.032225.

[55] S. Zhang, Z. Yong, Y. Shi, S. He, Numerical analysis of an optical nanoscale particles trapping device based on a slotted nanobeam cavity, Sci Rep. 6 (2016) 35977. https://doi.org/10.1038/srep35977.

[56] J. Wang, C. Wang, Z. Han, H. Tian, On-chip trapping and sorting of nanoparticles using a single slotted photonic crystal nanobeam cavity, Opt. Express, OE. 30 (2022) 11192–11202. https://doi.org/10.1364/OE.449193.

[57] D.-Q. Yang, B. Duan, X. Liu, A.-Q. Wang, X.-G. Li, Y.-F. Ji, Photonic Crystal Nanobeam Cavities for Nanoscale Optical Sensing: A Review, Micromachines. 11 (2020) 72. https://doi.org/10.3390/mi11010072.

[58] M.W. McCutcheon, M. Lončar, Design of a silicon nitride photonic crystal nanocavity with a Quality factor of one million for coupling to a diamond nanocrystal, Opt. Express, OE. 16 (2008) 19136–19145. https://doi.org/10.1364/OE.16.019136.

[59] M. Khan, T. Babinec, M.W. McCutcheon, P. Deotare, M. Lončar, Fabrication and characterization of high-quality-factor silicon nitride nanobeam cavities, Opt. Lett., OL. 36 (2011) 421–423. https://doi.org/10.1364/OL.36.000421.

[60] K.G. Fehler, A.P. Ovvyan, N. Gruhler, W.H.P. Pernice, A. Kubanek, Efficient Coupling of an Ensemble of Nitrogen Vacancy Center to the Mode of a High-Q, Si3N4 Photonic Crystal Cavity, ACS Nano. 13 (2019) 6891–6898. https://doi.org/10.1021/acsnano.9b01668.

[61] T. Xu, M.S. Wheeler, H.E. Ruda, M. Mojahedi, J.S. Aitchison, The influence of material absorption on the quality factor of photonic crystal cavities, Opt. Express, OE. 17 (2009) 8343–8348. https://doi.org/10.1364/OE.17.008343.

[62] C.-Y. Chao, L.J. Guo, Design and optimization of microring resonators in biochemical sensing applications, Journal of Lightwave Technology. 24 (2006) 1395–1402. https://doi.org/10.1109/JLT.2005.863333.

[63] X. Zhou, L. Zhang, A.M. Armani, D. Zhang, X. Duan, J. Liu, H. Zhang, W. Pang, On-Chip Biological and Chemical Sensing With Reversed Fano Lineshape Enabled by Embedded Microring Resonators, IEEE Journal of Selected Topics in Quantum Electronics. 20 (2014) 35–44. https://doi.org/10.1109/JSTQE.2013.2294465.

[64] W. Bogaerts, P. De Heyn, T. Van Vaerenbergh, K. De Vos, S. Kumar Selvaraja, T. Claes, P. Dumon, P. Bienstman, D. Van Thourhout, R. Baets, Silicon microring resonators, Laser & Photonics Reviews. 6 (2012) 47–73. https://doi.org/10.1002/lpor.201100017.

[65] P. Steglich, M. Hülsemann, B. Dietzel, A. Mai, Optical Biosensors Based on Silicon-On-Insulator Ring Resonators: A Review, Molecules. 24 (2019) 519. https://doi.org/10.3390/molecules24030519.

[66] L.S. Puumala, S.M. Grist, K. Wickremasinghe, M.A. Al-Qadasi, S.J. Chowdhury, Y. Liu, M. Mitchell, L. Chrostowski, S. Shekhar, K.C. Cheung, An Optimization Framework for Silicon Photonic Evanescent-Field Biosensors Using Sub-Wavelength Gratings, Biosensors. 12 (2022) 840. https://doi.org/10.3390/bios12100840.

[67] P. Steglich, C. Villringer, S. Pulwer, F. Heinrich, J. Bauer, B. Dietzel, C. Mai, A. Mai, M. Casalboni, S. Schrader, Hybrid-Waveguide Ring Resonator for Biochemical Sensing, IEEE Sensors Journal. 17 (2017) 4781–4790. https://doi.org/10.1109/JSEN.2017.2710318.

[68] S. Schmidt, J. Flueckiger, W. Wu, S. Grist, S. Talebi Fard, V. Donzella, P. Khumwan, E. Thompson, Q. Wang, P. Kulik, J. Kirk, X. Wang, A. Sherwali, C. Karen, L. Chrostowski, D. Ratner, Improving the performance of silicon photonic rings, disks, and Bragg gratings for use in label-free biosensing, in: 2014.

[69] R.S. El Shamy, M.A. Swillam, X. Li, On-chip complex refractive index detection at multiple wavelengths for selective sensing, Sci Rep. 12 (2022) 9343. https://doi.org/10.1038/s41598-022-13033-3.

[70] C.A. Barrios, B. Sánchez, K.B. Gylfason, A. Griol, H. Sohlström, M. Holgado, R. Casquel, Demonstration of slot-waveguide structures on silicon nitride / silicon oxide platform, Opt. Express, OE. 15 (2007) 6846–6856. https://doi.org/10.1364/OE.15.006846.

[71] C.A. Barrios, Optical Slot-Waveguide Based Biochemical Sensors, Sensors. 9 (2009) 4751–4765. https://doi.org/10.3390/s90604751.

[72] J. Niehusmann, A. Vörckel, P.H. Bolivar, T. Wahlbrink, W. Henschel, H. Kurz, Ultrahigh-quality-factor silicon-on-insulator microring resonator, Opt. Lett., OL. 29 (2004) 2861–2863. https://doi.org/10.1364/OL.29.002861.

[73] L. Castelló-Pedrero, M.I. Gómez-Gómez, J. García-Rupérez, A. Griol, A. Martínez, Performance improvement of a silicon nitride ring resonator biosensor operated in the TM mode at 1310 nm, Biomed. Opt. Express, BOE. 12 (2021) 7244–7260. https://doi.org/10.1364/BOE.437823.

[74] I.M. White, X. Fan, On the performance quantification of resonant refractive index sensors, Opt. Express, OE. 16 (2008) 1020–1028. https://doi.org/10.1364/OE.16.001020.

[75] L. Kassa-Baghdouche, High-sensitivity spectroscopic gas sensor using optimized H1 photonic crystal microcavities, J. Opt. Soc. Am. B, JOSAB. 37 (2020) A277–A284. https://doi.org/10.1364/JOSAB.398330.

[76] P.B. Deotare, M.W. McCutcheon, I.W. Frank, M. Khan, M. Lončar, High quality factor photonic crystal nanobeam cavities, Applied Physics Letters. 94 (2009) 121106. https://doi.org/10.1063/1.3107263.

[77] L. Ding, D. Eschimese, T.Y.L. Ang, D. Morits, H.S. Chu, S.T. Lim, C.E. Png, S. Gorelik, R. Paniagua-Dominguez, A.I. Kuznetsov, One-Dimensional High-Q Silicon Nanoparticle Chain

Resonators for Refractive Index Sensing, ACS Appl. Nano Mater. 5 (2022) 3170–3176. https://doi.org/10.1021/acsanm.1c03866.

[78] J. Zhan, Z. Jafari, S. Veilleux, M. Dagenais, I. De Leon, High-Q nanobeam cavities on a silicon nitride platform enabled by slow light, APL Photonics. 5 (2020) 066101. https://doi.org/10.1063/5.0007279.

[79] M. Notomi, E. Kuramochi, H. Taniyama, Ultrahigh-Q Nanocavity with 1D Photonic Gap, Opt. Express, OE. 16 (2008) 11095–11102. https://doi.org/10.1364/OE.16.011095.

[80] K. Yao, Y. Shi, High-Q width modulated photonic crystal stack mode-gap cavity and its application to refractive index sensing, Opt. Express, OE. 20 (2012) 27039–27044. https://doi.org/10.1364/OE.20.027039.

[81] S. Mauthe, P. Tiwari, M. Scherrer, D. Caimi, M. Sousa, H. Schmid, K.E. Moselund, N. Vico Triviño, Hybrid III–V Silicon Photonic Crystal Cavity Emitting at Telecom Wavelengths, Nano Lett. 20 (2020) 8768–8772. https://doi.org/10.1021/acs.nanolett.0c03634.

[82] A.F. Oskooi, D. Roundy, M. Ibanescu, P. Bermel, J.D. Joannopoulos, S.G. Johnson, Meep: A flexible free-software package for electromagnetic simulations by the FDTD method, Computer Physics Communications. 181 (2010) 687–702. https://doi.org/10.1016/j.cpc.2009.11.008.

[83] S.G. Johnson, J.D. Joannopoulos, Block-iterative frequency-domain methods for Maxwell's equations in a planewave basis, Opt. Express, OE. 8 (2001) 173–190. https://doi.org/10.1364/OE.8.000173.

[84] F.S.F. Brossard, S.G. Schirmer, A.R.A. Chalcraft, D.M. Whittaker, High Q photonic crystal cavities with tapered air holes, in: Physics and Simulation of Optoelectronic Devices XIX, SPIE, 2011: pp. 400–409. https://doi.org/10.1117/12.874212.

[85] Y. Tanaka, T. Asano, Y. Akahane, B.-S. Song, S. Noda, Theoretical investigation of a two-dimensional photonic crystal slab with truncated cone air holes, Applied Physics Letters. 82 (2003) 1661–1663. https://doi.org/10.1063/1.1559947.

[86] B.-S. Song, S.-W. Jeon, S. Noda, Symmetrically glass-clad photonic crystal nanocavities with ultrahigh quality factors, Opt. Lett., OL. 36 (2011) 91–93. https://doi.org/10.1364/OL.36.000091.

[87] F. Sun, Y. Yang, Z. Li, D. Yang, H. Tian, C. Lee, Controlling of spatial modes in multi-mode photonic crystal nanobeam cavity, Opt. Express, OE. 30 (2022) 21764–21773. https://doi.org/10.1364/OE.460199.

[88] D.T. Spencer, J.F. Bauters, M.J.R. Heck, J.E. Bowers, Integrated waveguide coupled Si_3N_4 resonators in the ultrahigh-Q regime, Optica, OPTICA. 1 (2014) 153–157. https://doi.org/10.1364/OPTICA.1.000153.

[89] S. Iadanza, A.P. Bakoz, P.K.J. Singaravelu, D. Panettieri, S.A. Schulz, G.C.R. Devarapu, S. Guerber, C. Baudot, F. Boeuf, S. Hegarty, L. O'Faolain, Thermally stable hybrid cavity laser based on silicon nitride gratings, Appl. Opt., AO. 57 (2018) E218–E223. https://doi.org/10.1364/AO.57.00E218.

[90] D. Panettieri, L. O'Faolain, M. Grande, Control of Q-factor in nanobeam cavities on substrate, in: 2016 18th International Conference on Transparent Optical Networks (ICTON), 2016: pp. 1–4. https://doi.org/10.1109/ICTON.2016.7550638.

[91] V.R. Almeida, Q. Xu, C.A. Barrios, M. Lipson, Guiding and confining light in void nanostructure, Opt. Lett., OL. 29 (2004) 1209–1211. https://doi.org/10.1364/OL.29.001209.

[92] M.G. Scullion, T.F. Krauss, A. Di Falco, Slotted Photonic Crystal Sensors, Sensors. 13 (2013) 3675–3710. https://doi.org/10.3390/s130303675.

[93] K. Yao, Y. Shi, High-Q width modulated photonic crystal stack mode-gap cavity and its application to refractive index sensing, Opt. Express. 20 (2012) 27039. https://doi.org/10.1364/OE.20.027039.

[94] D. Panettieri, L. O'Faolain, M. Grande, Control of Q-factor in nanobeam cavities on substrate, in: 2016 18th International Conference on Transparent Optical Networks (ICTON), IEEE, Trento, Italy, 2016: pp. 1–4. https://doi.org/10.1109/ICTON.2016.7550638.

[95] P. Xu, K. Yao, J. Zheng, X. Guan, Y. Shi, Slotted photonic crystal nanobeam cavity with parabolic modulated width stack for refractive index sensing, Opt. Express, OE. 21 (2013) 26908–26913. https://doi.org/10.1364/OE.21.026908.

[96] Y.-L. Fu, C.-S. Deng, S.-S. Ma, Design and analysis of refractive index sensors based on slotted photonic crystal nanobeam cavities with sidewall gratings, Appl. Opt., AO. 59 (2020) 896–903. https://doi.org/10.1364/AO.380459.

[97] J.E. Saunders, C. Sanders, H. Chen, H.-P. Loock, Refractive indices of common solvents and solutions at 1550 nm, Appl. Opt., AO. 55 (2016) 947–953. https://doi.org/10.1364/AO.55.000947.

[98] Z. Gou, C. Wang, Z. Han, T. Nie, H. Tian, Artificial neural networks assisting the design of a dual-mode photonic crystal nanobeam cavity for simultaneous sensing of the refractive index and temperature, Appl. Opt., AO. 61 (2022) 4802–4808. https://doi.org/10.1364/AO.453818.

[99] Z. Gou, C. Wang, Y. Yang, Z. Han, T. Nie, H. Tian, Artificial neural networks applied in fast-designing ultrabroad bandgap elliptical hole dielectric mode photonic crystal nanobeam cavity, Appl. Opt., AO. 60 (2021) 8977–8982. https://doi.org/10.1364/AO.431719.

[100] T. Nie, Z. Han, Z. Gou, C. Wang, H. Tian, High anti-interference dual-parameter sensor using EIT-like effect photonic crystal cavity coupled system, Appl. Opt., AO. 61 (2022) 1552–1558. https://doi.org/10.1364/AO.452140.

[101] Z. Han, C. Wang, Y. Liu, H. Tian, Simultaneous detection of complex refractive index and temperature using a compact side-coupled photonic crystal nanobeam cavity, J. Opt. Soc. Am. B, JOSAB. 38 (2021) 2765–2774. https://doi.org/10.1364/JOSAB.428815.

[102] Q. Liu, D. Zeng, C. Mei, H. Li, Q. Huang, X. Zhang, Integrated photonic devices enabled by silicon traveling wave-like Fabry–Perot resonators, Opt. Express, OE. 30 (2022) 9450–9462. https://doi.org/10.1364/OE.452450.

[103] H. Shu, L. Chang, Y. Tao, B. Shen, W. Xie, M. Jin, A. Netherton, Z. Tao, X. Zhang, R. Chen, B. Bai, J. Qin, S. Yu, X. Wang, J.E. Bowers, Microcomb-driven silicon photonic systems, Nature. 605 (2022) 457–463. https://doi.org/10.1038/s41586-022-04579-3.

[104] K.Y. Yang, J. Skarda, M. Cotrufo, A. Dutt, G.H. Ahn, M. Sawaby, D. Vercruysse, A. Arbabian, S. Fan, A. Alù, J. Vučković, Inverse-designed non-reciprocal pulse router for chip-

based LiDAR, Nat. Photonics. 14 (2020) 369–374. https://doi.org/10.1038/s41566-020-0606-0.

[105] J. Zheng, Z. Fang, C. Wu, S. Zhu, P. Xu, J.K. Doylend, S. Deshmukh, E. Pop, S. Dunham, M. Li, A. Majumdar, Nonvolatile Electrically Reconfigurable Integrated Photonic Switch Enabled by a Silicon PIN Diode Heater, Advanced Materials. 32 (2020) 2001218. https://doi.org/10.1002/adma.202001218.

[106] J.M.C. Boggio, D. Bodenmüller, S. Ahmed, S. Wabnitz, D. Modotto, T. Hansson, Efficient Kerr soliton comb generation in micro-resonator with interferometric back-coupling, Nat Commun. 13 (2022) 1292. https://doi.org/10.1038/s41467-022-28927-z.

[107] D. Grassani, S. Azzini, M. Liscidini, M. Galli, M.J. Strain, M. Sorel, J.E. Sipe, D. Bajoni, Micrometer-scale integrated silicon source of time-energy entangled photons, Optica, OPTICA. 2 (2015) 88–94. https://doi.org/10.1364/OPTICA.2.000088.

[108] U. Fano, Effects of Configuration Interaction on Intensities and Phase Shifts, Phys. Rev. 124 (1961) 1866–1878. https://doi.org/10.1103/PhysRev.124.1866.

[109] C. Zhang, G. Kang, Y. Xiong, T. Xu, L. Gu, X. Gan, Y. Pan, J. Qu, Photonic thermometer with a sub-millikelvin resolution and broad temperature range by waveguide-microring Fano resonance, Opt. Express, OE. 28 (2020) 12599–12608. https://doi.org/10.1364/OE.390966.

[110] Li-Dan L., Lian-Qing Z., Zhou-Mo Z., Yi-Ping C., Dong-Liang Z., Pei Y., Progress of silicon photonic devices-based Fano resonance, Acta Phys. Sin. 70 (2021) 034204–20. https://doi.org/10.7498/aps.70.20200550.

[111] J. Wang, J. Lin, P. Jin, S. Liu, K. Zhou, Single nanoparticle sensing based on Fano resonances enabled by microring resonator with a micro-reflective unit, Opt. Express. (2023). https://doi.org/10.1364/OE.500620.

[112] M.F. Limonov, M.V. Rybin, A.N. Poddubny, Y.S. Kivshar, Fano resonances in photonics, Nature Photon. 11 (2017) 543–554. https://doi.org/10.1038/nphoton.2017.142.

[113] K.K. Mehta, J.S. Orcutt, R.J. Ram, Fano line shapes in transmission spectra of silicon photonic crystal resonators, Appl. Phys. Lett. 102 (2013) 081109. https://doi.org/10.1063/1.4794064.

[114] D. Bekele, Y. Yu, K. Yvind, J. Mork, In-Plane Photonic Crystal Devices using Fano Resonances, Laser & Photonics Reviews. 13 (2019) 1900054. https://doi.org/10.1002/lpor.201900054.

[115] W. Zhou, D. Zhao, Y.-C. Shuai, H. Yang, S. Chuwongin, A. Chadha, J.-H. Seo, K.X. Wang, V. Liu, Z. Ma, S. Fan, Progress in 2D photonic crystal Fano resonance photonics, Progress in Quantum Electronics. 38 (2014) 1–74. https://doi.org/10.1016/j.pquantelec.2014.01.001.

[116] M. Galli, S.L. Portalupi, M. Belotti, L.C. Andreani, L. O'Faolain, T.F. Krauss, Light scattering and Fano resonances in high-Q photonic crystal nanocavities, Appl. Phys. Lett. 94 (2009) 071101. https://doi.org/10.1063/1.3080683.

[117] I.S. Maksymov, A.E. Miroshnichenko, Active control over nanofocusing with nanorod plasmonic antennas, Opt. Express, OE. 19 (2011) 5888–5894. https://doi.org/10.1364/OE.19.005888.

[118] Z.-M. Meng, A. Liang, Z.-Y. Li, Fano resonances in photonic crystal nanobeams side-coupled with nanobeam cavities, Journal of Applied Physics. 121 (2017) 193102. https://doi.org/10.1063/1.4983450.

[119] A.D. Osterkryger, J.R. de Lasson, M. Heuck, Y. Yu, J. Mørk, N. Gregersen, Spectral symmetry of Fano resonances in a waveguide coupled to a microcavity, Opt. Lett. 41 (2016) 2065. https://doi.org/10.1364/OL.41.002065.

[120] M.F. Limonov, Fano resonance for applications, Adv. Opt. Photon., AOP. 13 (2021) 703–771. https://doi.org/10.1364/AOP.420731.

[121] A.C. Ruege, R.M. Reano, Multimode waveguide-cavity sensor based on fringe visibility detection, Opt. Express, OE. 17 (2009) 4295–4305. https://doi.org/10.1364/OE.17.004295.

[122] Z. Tu, D. Gao, M. Zhang, D. Zhang, High-sensitivity complex refractive index sensing based on Fano resonance in the subwavelength grating waveguide micro-ring resonator, Opt. Express, OE. 25 (2017) 20911–20922. https://doi.org/10.1364/OE.25.020911.

[123] T. Christopoulos, O. Tsilipakos, G. Sinatkas, E.E. Kriezis, On the calculation of the quality factor in contemporary photonic resonant structures, Opt. Express, OE. 27 (2019) 14505–14522. https://doi.org/10.1364/OE.27.014505.

[124] A.E. Miroshnichenko, S.F. Mingaleev, S. Flach, Y.S. Kivshar, Nonlinear Fano resonance and bistable wave transmission, Phys. Rev. E. 71 (2005) 036626. https://doi.org/10.1103/PhysRevE.71.036626.

[125] A.E. Miroshnichenko, Y.S. Kivshar, Engineering Fano resonances in discrete arrays, Phys. Rev. E. 72 (2005) 056611. https://doi.org/10.1103/PhysRevE.72.056611.

[126] S.F. Mingaleev, A.E. Miroshnichenko, Y.S. Kivshar, K. Busch, All-optical switching, bistability, and slow-light transmission in photonic crystal waveguide-resonator structures, Phys. Rev. E. 74 (2006) 046603. https://doi.org/10.1103/PhysRevE.74.046603.

[127] S. Fan, W. Suh, J.D. Joannopoulos, Temporal coupled-mode theory for the Fano resonance in optical resonators, J. Opt. Soc. Am. A, JOSAA. 20 (2003) 569–572. https://doi.org/10.1364/JOSAA.20.000569.

[128] Y. Yu, M. Heuck, H. Hu, W. Xue, C. Peucheret, Y. Chen, L.K. Oxenløwe, K. Yvind, J. Mørk, Fano resonance control in a photonic crystal structure and its application to ultrafast switching, Appl. Phys. Lett. 105 (2014) 061117. https://doi.org/10.1063/1.4893451.

[129] F. Sun, Z. Li, B. Tang, B. Li, P. Zhang, R. Liu, G. Yang, K. Huang, Z. Han, J. Luo, W. Wang, Y. Yang, Scalable high Q-factor Fano resonance from air-mode photonic crystal nanobeam cavity, Nanophotonics. 12 (2023) 3135–3148. https://doi.org/10.1515/nanoph-2023-0170.

[130] S. Fan, Sharp asymmetric line shapes in side-coupled waveguide-cavity systems, Appl. Phys. Lett. 80 (2002) 908–910. https://doi.org/10.1063/1.1448174.

[131] M. Heuck, P.T. Kristensen, Y. Elesin, J. Mørk, Improved switching using Fano resonances in photonic crystal structures, Opt. Lett., OL. 38 (2013) 2466–2468. https://doi.org/10.1364/OL.38.002466.

[132] Y. Ding, R. Magnusson, Band gaps and leaky-wave effects in resonant photonic-crystal waveguides, Opt. Express, OE. 15 (2007) 680–694. https://doi.org/10.1364/OE.15.000680.

[133] D. Conteduca, G.S. Arruda, I. Barth, Y. Wang, T.F. Krauss, E.R. Martins, Beyond Q: The Importance of the Resonance Amplitude for Photonic Sensors, ACS Photonics. 9 (2022) 1757–1763. https://doi.org/10.1021/acsphotonics.2c00188.

[134] D. Pinto, J.P. Waclawek, S. Lindner, H. Moser, G. Ricchiuti, B. Lendl, Wavelength modulated diode probe laser for an interferometric cavity-assisted photothermal spectroscopy gas sensor, Sensors and Actuators B: Chemical. 377 (2023) 133061. https://doi.org/10.1016/j.snb.2022.133061.

[135] L. Ranno, P. Gupta, K. Gradkowski, R. Bernson, D. Weninger, S. Serna, A.M. Agarwal, L.C. Kimerling, J. Hu, P. OBrien, Integrated Photonics Packaging: Challenges and Opportunities, ACS Photonics. 9 (2022) 3467–3485. https://doi.org/10.1021/acsphotonics.2c00891.

[136] R.R.G. Soares, D.R. Santos, I.F. Pinto, A.M. Azevedo, M.R. Aires-Barros, V. Chu, J.P. Conde, Multiplexed microfluidic fluorescence immunoassay with photodiode array signal acquisition for sub-minute and point-of-need detection of mycotoxins, Lab Chip. 18 (2018) 1569–1580. https://doi.org/10.1039/C8LC00259B.

[137] B.C. Dhar, N.Y. Lee, Lab-on-a-Chip Technology for Environmental Monitoring of Microorganisms, BioChip J. 12 (2018) 173–183. https://doi.org/10.1007/s13206-018-2301-5.

[138] S. Cardoso, D.C. Leitao, T.M. Dias, J. Valadeiro, M.D. Silva, A. Chicharo, V. Silverio, J. Gaspar, P.P. Freitas, Challenges and trends in magnetic sensor integration with microfluidics for biomedical applications, J. Phys. D: Appl. Phys. 50 (2017) 213001. https://doi.org/10.1088/1361-6463/aa66ec.

[139] H. Nomada, K. Morita, H. Higuchi, H. Yoshioka, Y. Oki, Carbon–polydimethylsiloxane-based integratable optical technology for spectroscopic analysis, Talanta. 166 (2017) 428–432. https://doi.org/10.1016/j.talanta.2015.11.066.

[140] H. Shimizu, C. Chen, Y. Tsuyama, T. Tsukahara, T. Kitamori, Photothermal spectroscopy and micro/nanofluidics, Journal of Applied Physics. 132 (2022) 060902. https://doi.org/10.1063/5.0097665.

[141] S.C. Terry, J.H. Jerman, J.B. Angell, A gas chromatographic air analyzer fabricated on a silicon wafer, IEEE Transactions on Electron Devices. 26 (1979) 1880–1886. https://doi.org/10.1109/T-ED.1979.19791.

[142] R. Sivakumar, N. Yoon Lee, Microfluidic device fabrication mediated by surface chemical bonding, Analyst. 145 (2020) 4096–4110. https://doi.org/10.1039/D0AN00614A.

[143] C. Iliescu, H. Taylor, M. Avram, J. Miao, S. Franssila, A practical guide for the fabrication of microfluidic devices using glass and silicon, Biomicrofluidics. 6 (2012) 016505. https://doi.org/10.1063/1.3689939.

[144] A. Borók, K. Laboda, A. Bonyár, PDMS Bonding Technologies for Microfluidic Applications: A Review, Biosensors. 11 (2021) 292. https://doi.org/10.3390/bios11080292.

[145] J. Wang, M.M. Sanchez, Y. Yin, R. Herzer, L. Ma, O.G. Schmidt, Silicon-Based Integrated Label-Free Optofluidic Biosensors: Latest Advances and Roadmap, Advanced Materials Technologies. 5 (2020) 1901138. https://doi.org/10.1002/admt.201901138.

[146] B. Subramanian, N. Kim, W. Lee, D.A. Spivak, D.E. Nikitopoulos, R.L. McCarley, S.A. Soper, Surface Modification of Droplet Polymeric Microfluidic Devices for the Stable and Continuous Generation of Aqueous Droplets, Langmuir. 27 (2011) 7949–7957. https://doi.org/10.1021/la200298n.

[147] Examination of Polystyrene by Inverse GC: Part 2. Above Glass Transition Temperature | SpringerLink, (n.d.). https://link.springer.com/article/10.1007/s10337-010-1830-4 (accessed November 1, 2023).

[148] C.-H. Chan, J.-K. Chen, F.-C. Chang, Specific DNA extraction through fluid channels with immobilization of layered double hydroxides on polycarbonate surface, Sensors and Actuators B: Chemical. 133 (2008) 327–332. https://doi.org/10.1016/j.snb.2008.02.041.

[149] S. Hassanpour-Tamrin, A. Sanati-Nezhad, A. Sen, A simple and low-cost approach for irreversible bonding of polymethylmethacrylate and polydimethylsiloxane at room temperature for high-pressure hybrid microfluidics, Sci Rep. 11 (2021) 4821. https://doi.org/10.1038/s41598-021-83011-8.

[150] S.R.A. Kratz, C. Eilenberger, P. Schuller, B. Bachmann, S. Spitz, P. Ertl, M. Rothbauer, Characterization of four functional biocompatible pressure-sensitive adhesives for rapid prototyping of cell-based lab-on-a-chip and organ-on-a-chip systems, Sci Rep. 9 (2019) 9287. https://doi.org/10.1038/s41598-019-45633-x.

[151] C. Carver, M. Boaks, J. Kim, K. Larson, G.P. Nordin, R.M. Camacho, Automated photonic tuning of silicon microring resonators using a 3D-printed microfluidic mixer, OSA Continuum. 4 (2021) 2075. https://doi.org/10.1364/OSAC.425058.

[152] K. Larson, A. Hammond, C. Carver, D. Anderson, M. Viglione, M. Boaks, G. Nordin, R.M. Camacho, Post-fabrication tuning of microring resonators using 3D-printed microfluidics, Opt. Lett. 46 (2021) 4650. https://doi.org/10.1364/OL.433987.

[153] D. Erickson, T. Rockwood, T. Emery, A. Scherer, D. Psaltis, Nanofluidic tuning of photonic crystal circuits, Opt. Lett., OL. 31 (2006) 59–61. https://doi.org/10.1364/OL.31.000059.

[154] M. Li, P. Bai, C. Yan, S. Peng, Mid-infrared silicon metasurfaces for near-field enhancement of molecular fingerprints, Opt. Lett., OL. 48 (2023) 1502–1505. https://doi.org/10.1364/OL.479854.

[155] C. Liu, Y. Bai, J. Zhou, J. Chen, L. Qiao, Refractive index sensing by asymmetric dielectric gratings with both bound states in the continuum and guided mode resonances, Opt. Express, OE. 29 (2021) 42978–42988. https://doi.org/10.1364/OE.446937.

[156] DiffractMOD RCWA Software - RSoft Photonic Device Tools | Synopsys Photonic Solutions, (n.d.). https://www.synopsys.com/photonic-solutions/rsoft-photonic-device-tools/passive-device-diffractmod.html (accessed November 3, 2023).

[157] K. Yee, Numerical solution of initial boundary value problems involving maxwell's equations in isotropic media, IEEE Transactions on Antennas and Propagation. 14 (1966) 302–307. https://doi.org/10.1109/TAP.1966.1138693.

[158] A. Taflove, A. Oskooi, S.G. Johnson, Advances in FDTD Computational Electrodynamics: Photonics and Nanotechnology, Artech House, 2013.

[159] The Scheme Programming Language, 4th Edition, (n.d.).

[160] V.A. Mandelshtam, H.S. Taylor, Harmonic inversion of time signals and its applications, The Journal of Chemical Physics. 107 (1997) 6756–6769. https://doi.org/10.1063/1.475324.

[161] S. Iadanza, MOS Compatible Deposited Materials for Optical Interconnects, Theses. (2022). https://sword.cit.ie/allthe/770.

"Nothing in life is to be feared, it is only to be understood. Now is the time to understand more, so that we may fear less."

– Marie Skłodowska-Curie

OPTAPHI has received funding from the European Union's Horizon 2020 research and innovation programme under the Marie Skłodowska-Curie grant agreement No. 860808